The development and characterization of a nickel/metal hydride microbattery for microfluidic applications

by

Hamid Falahati

A thesis submitted to the
Department of Chemical Engineering
in conformity with the requirements for
the degree of Doctor of Philosophy

Queen's University
Kingston, Ontario, Canada
July 2015

To someone very special in my life

Elmira

who always inspires me

and

In memory of

my beloved grandma

Abstract

Micro Electro Mechanical Systems as well as Microfluidics are versatile technologies which have been evolved due to the advantage of miniaturization over the last decades. However, the majority of microfluidic devices are still powered by macroscale power supplies. Here, interconnection problems, unwanted electronic interactions (noise), and difficulties in controlling the power delivered are some of the problems which can arise. One possible approach to ease such difficulties is through the use of integrated (embedded) power sources. This thesis is focused on the development and characterization of a nickel/metal hydride microbattery on a glass substrate which can be easily integrated during the regular microfabrication process of the microfluidic device.

Glass or glass-like materials, such as silicon dioxide, are often used as substrates for microfluidic chips. Hence, we pursue a two-dimensional approach in that we fabricate thin films of electroactive materials on glass wafers using microfabrication techniques which are common in semiconductor (electronics) industries. A tailored polymeric layer is placed between the two electrodes to serve as an electrolyte reservoir and electrode separator in a sandwich-like structure which mimics a typical microfluidic chip design.

The microfabricated electrodes are investigated in terms of material characterization and electrochemical performance. In detail, we use x-ray diffraction, x-ray photoelectron spectroscopy, field emission scanning electron microscope/energy dispersive spectroscopy, and profilometry to study the materials properties as well as the surface morphologies. Furthermore, cyclic voltammetry, charge-discharge characterization, and electrochemical impedance spectroscopy are performed to gain insights into the electrochemical performance of the single nickel electrode and of the single metal hydride electrode. This is also accompanied by a mathematical derivation and evaluation of electrolytic and gas sorption models of the metal hydride electrode.

Finally, the performance of the microbattery is investigated using charge-discharge, voltage-current, and electrochemical impedance spectroscopy measurements.

Co-Authorship Statement

All papers in this thesis, presented in chapters 2 to 5, are co-authored with my supervisor Dr. Dominik P.J. Barz at Queen's University. The paper presented in chapter 3 of this thesis is also co-authored with Edward Kim who was a visiting undergraduate research student in the summer of 2013 at Queen's University. In detail, papers are as follows:

Paper 1: Hamid Falahati and Dominik P.J. Barz (2013), "Evaluation of hydrogen sorption models for AB_5-type metal alloys by employing a gravimetric technique", *International Journal of Hydrogen Energy*, Vol. 38, Issue 21, Pages 8838-8851.

Paper 2: Hamid Falahati, Edward Kim and Dominik P.J. Barz (2015), "Fabrication and Characterization of Thin-Film Nickel Hydroxide Electrodes for Micro-Power Applications", *ACS Applied Materials & Interfaces*, Vol. 7, Issue 23, Pages 12797-12808.

Paper 3: Hamid Falahati and Dominik P.J. Barz, "Fabrication and Characterization of Thin-Film Metal Hydride Electrodes for Microbattery Applications", *To be submitted.*

Paper 4: Hamid Falahati and Dominik P.J. Barz, "A Nickel/Metal Hydride Microbattery for Microfluidic Applications", *To be submitted.*

Acknowledgments

First and foremost I wish to express my sincere appreciation and deepest gratitude to my supervisor, Dr. Dominik Barz, for his valuable guidance and his patience in the completion of this thesis. He provided me with excellent guidance throughout this process with endless support and editorial comments on all of my written work; this achievement would not have been possible otherwise. Dr. Barz's invaluable guidance improved the quality of my work tremendously. By going above and beyond what is expected from an academic supervisor, Dr. Barz has taught me the importance of hard work and passion; it certainly was a privilege to have him as my PhD supervisor. I enjoyed a great deal of freedom and the inherent discipline while working under his supervision during my time at Queen's University. I also learned a lot through our lively discussions.

I would like to thank my PhD committee members, Dr. Brant Peppley, Dr. Robert Knobel and Dr. Carlos Escobedo (Head's delegate), for providing me with useful comments during my comprehensive examination session. I would also like to thank Dr. Mike B. Evans, Professor Emeritus at the Royal Military College of Canada for his advice and support, Dr. Wojtek Halliop and Dr. Dzmitry Malevich for their useful suggestions and discussions during my studies at Queen's-RMC Fuel Cell Research Centre. I am further indebted to many colleagues and friends including

the support and management staff within the department of chemical engineering.

I was also surrounded by several amazing undergraduate and graduate students at Queen's University and Queen's-RMC Fuel Cell Research Centre. I wish to thank the past and the present students and researchers with whom I have had the pleasure of working, especially those who were partially involved in the completion of this research work including Edward Kim, Rio Vincento Festarini, Alisha Giglio, Johanna Bort, and Karl Murray. I also thank the personnel of Microelectronics Fabrication Laboratory (MFL), Rob Vandusen and Richard Adams at Carleton University in Ottawa, for their assistance with the DC magnetron sputter instrument.

Last but not least, I want to thank my beautiful Elmira who has given me encouragement and emotional support throughout this study. My special thank you goes to Mr. Hossein Moghadam who provided me with inspirational support. Finally, I wish to thank my parents, Mehdi and Nooshfar, for their endless support, encouragement and understanding throughout these years.

I also gratefully acknowledge the financial support from Queen's University, the Natural Sciences and Engineering Research Council of Canada (NSERC), and CMC microsystems. It was an honor to receive the Queen Elizabeth II Graduate Scholarship in Science and Technology and I am very thankful for that.

Table of Contents

List of Tables

List of Figures

Chapter 1

Introduction and Background

1.1 Motivation

Portable and wearable micro-electro-mechanical-systems (MEMS) [1] devices have been increasingly emerging into our lives while their utilization ranges from communications to medical diagnostics. The advantage of microscale systems lies in the reduction of sample volumes, portability, cost-effectiveness in various testing procedures along with higher efficiencies. Additionally, miniaturization results in large surface area to volume ratios which promotes surface phenomena, and significantly higher heat and mass transfer rates in comparison with their macroscale counterparts are observed [2]. Given all these advantages, microfluidic systems have attracted much attention in that they offer size reduction and the possibility of integration of several functions or tasks in a single unit [3]. Microfluidic technologies comprise different concepts such as micro-total-analysis-systems (μTAS) [4], Lab-on-a-Chip (LOC) [5] and Point-of-Care-Testing (POCT). Typical applications aim at chemical analytics and medical diagnostics such as blood sample testing of the sugar level of a diabetic person. POCT also gained particular attention for the use in developing countries since a centralized hospital (laboratory) may not be easily accessible in various regions. Hence, the utilization of POCT devices can facilitate proper medical treatment to patients living in remote areas [6] as well as enable the epidemiological surveillance of fast-spreading diseases [7]. Chin et al. have reviewed the most important diseases in developing countries with their corresponding potential LOC devices which can be used to improve the health of people in ref.[8]. Also, they report a list of about 40 diseases which can potentially find a treatment through testing using POCT devices in near future. However, the market trends show that the current penetration of such POCT devices is rather slow. One explanation can be the fact that these devices are designed and manufactured without taking into account the local factors including culture, society, life standards, and expectations as emphasized by the United Nations development program [9] (as cited in [8]). Hence, it seems that designing and fabricating simple POCT kits, which can be used by any person despite their level of education and cultural background, plays a key role in their acceptance. Cost-effective POCT devices are also attractive in developed countries where health care expenses are high [10]. Such POCT devices can be single-use but also reusable for multiple times to offset the fabrication costs.

The requirements to power microsystems heavily depends on the used technology as well as on the application. In terms of remote sensing microsystems, Humble et al. have suggested power requirements for standby and data collection/processing activities in the range of 3 to $30\,\mu W$ and 100 to $1000\,\mu W$, respectively [11]. In contrast, Puers and Wouters designed a flexible temperature and motion sensing device based on electronic interface circuits with a low power consumption of $35\,\mu W$

[12]. Chandrakasan et al. have reviewed ultra-low-power electronics for existing and emerging biomedical applications [13]. They have reported power requirements of $< 10\,\mu W$ for a pacemaker and a cardioverter-defibrillator while powers in the range of 100 to $2000\,\mu W$ are required for hearing aids [13]. Further, they have reported that a low power of $140\,\mu W$ is required for body-area monitoring microsystems [13]. There have been more works on MEMS sensors and processors which operate with ultra-low power consumption which is still sufficient for monitoring systems for body temperature and activity of animal or human [14]. For instance, Okada et al. have developed an electronic circuit which can work as a wireless sensor node for health monitoring systems which requires a lower power of $0.5\,\mu W$ [14]. Other works include an ultra-low-power wireless sensor node to monitor animal health ($460\,nW$) [15] and a temperature compensated timer for ultra low power wireless sensor nodes ($660\,pW$) [16]. To conclude, the required power for microscale devices depends on the application and the complexity; i.e., the number of sensors, actuators and processors which forms the microsystem. The required power spans over several orders of magnitude and the range is estimated to be roughly from $0.1\,\mu W$ to $1000 \mu W$.

Almost all microscale devices are currently powered by large and non-integrated (external) power supplies such as button cells. This can have several drawbacks such as connection problems and it may compromise the advantages which are offered through miniaturization. It has also been emphasized by Cook-Chennault et al. that the applications of MEMS technology has been significantly limited due to the poor performances, masses (or volumes), and lifetimes of current power sources [17]. Roundy et al. have put together a brief survey on a variety of potential power supplies for MEMS applications particularly for wireless sensor nodes [18]. They have reported that rechargeable and non-rechargeable lithium batteries with power densities of 7 and 45 $\mu W\,cm^{-3}$, respectively, as well as methanol fuel cell and hydrocarbon fuel micro heat engine with power densities of 280 and 333 $\mu W\,cm^{-3}$, respectively, (all values are normalized by a device size of $1\,cm^3$ as mentioned in ref.[18]) are potential power sources for wireless sensor nodes. Furthermore, since silicon dioxide-based materials have been extensively used as substrates for microfluidic devices, this study is focused on the microfabrication of a rechargeable microbattery on a glass substrate which, to our knowledge, has not been explored yet.

In terms of capacity requirements, if we assume an operation time of around $4\,hr\,day^{-1}$ for the wireless sensor node reported for health monitoring system by Okada et al.[14, 15] as mentioned above, a capacity of $\approx 1.7\,\mu Ah$ per day ($\approx 50\,\mu Ah$ per month) at a nominal voltage of $1.2\,V$ is required. This capacity is adequate for the sensor to perform the measurement every minute for a duration of 10 seconds.

1.1.1 Non-regenerative vs. regenerative power sources

Generally, we can categorize power supply systems into regenerative and non-regenerative ones [19]. Non-regenerative systems, such as micro-fuel cells [20], micro-turbines [21], micro-combustors [22], and micro-heat engines [23] require either fuel or materials to be continuously supplied to the system. Contrary, regenerative power sources are energy harvesting (power scavenging) systems based on piezoelectric, vibration, or thermoelectric effects, for instance. A comprehensive review of both regenerative and non-regenerative micro-power supplies reported in the literature until 2008 is available in ref.[19]. Later work includes that of Liu et al. who reported a power generator array based on thick-film piezoelectric cantilevers and delivering an effective electrical power of $3.98\,\mu W$ with 3.93 DC output voltage which has a potential use for wireless sensors [24]. Lam et al. have reported a MEMS-based photosynthetic cell with an open circuit voltage (OCV) of $470\,mV$ and a current density of $1.1\,\mu A\,cm^{-2}$ at $5.2\,\mu V$, which corresponds to a power density of around $0.1\,nW\,cm^{-3}$ [25]. Yang et al. and Chun et al. suggested a micro-power supply based on the relatively-old electrokinetic phenomenon, streaming potential [26, 27]. Here, a diluted electrolyte flows between the small gap between two electrodes which induces an electrical potential difference and generates a power up to $0.9\,\mu W\,cm^{-3}$. However, considerable mechanical energy is required to generate the $1.7\,bar$ pressure difference. Another (semi-)regenerative micro-power supply based on reverse electrodialysis has been reported by Broer et al. [28]. This concept offers a promising feature for an integration with bioMEMS and MEMS devices in that body fluids may be utilized as electrolytes. The authors have reported a voltage and a current of $0.5\,V$ and $20\,\mu A$ (max), respectively, when using $1M$ NaCl solution as an electrolyte. A five layer stack has been realized which delivers around $222\,nW\,cm^{-2}$ based on the effective membrane surface area.

Generally, batteries are non-regenerative systems with the capability of energy storage, particularly in the secondary type batteries which can provide continuous (steady) energy supply to microscale devices [17]. Further, there has been several attempts to couple solar cells (energy harvesting devices) with rechargeable microbatteries (hybrid power supplies) [29, 11]. In order to manufacture small power sources, several microbattery chemistries and manufacturing concepts have been reported as follows.

1.1.2 Microbattery chemistries and designs

Among microbatteries reported in the literature, lithium-(refs.[30, 31]), nickel-(refs.[11, 32]), and zinc- (refs.[33, 34]) based microbatteries have gained generally more attention as evident by the large number of publications. Albano et al. have published a short survey on microbatteries in ref.[33]. The survey covers the works published from 1995 to 2007. Here, a number of highlights from their survey are provided; the original references are also given. The $Li/LIPON/V_2O_5$ microbattery is proposed by Lemmerhirt and Wise (ref.[35] as cited in ref.[33]). They employ deep reactive-ion etching (DRIE) and low-pressure chemical vapor deposition (LPCVD) techniques to fabricate the cell which delivers capacities ranging between 13.5 and 18.5 μAh (for a discharge current of 2.42 to 48.4 μA) with an estimated power density range of 7.5 to 150 $\mu W\, cm^{-2}$ (for a nominal voltage of 3.75 V). Further, smaller capacities have been reported in other works with a chemistry of Mn_2O_4/solid lithium glass/Li for $\approx 15\, \mu Ah$ in refs.[33, 36]. Alahmad and Hess have reported a lithium microbattery which is rated at 4.25 V, with a capacity of 50 nAh to be used in miniaturized spacecraft applications [37]. Interestingly, Pikul et al. have reported on a high power density lithium microbattery which provides power densities for up to 74 $W\, cm^{-3}$ in 2013 [38]. They have emphasized that the high energy density is attributed to the high conductivity of the micro-electrodes, the very thin electro-active materials, the close electrode packing, and the high aspect ratio of the electrodes [38]. Lhermet et al. reported on an embedded solid state microbattery fabricated using PVD techniques for a charge density of roughly 100 $\mu Ah\, cm^{-2}$ which can deliver currents up to 3 $mA\, cm^{-2}$ [39]. Nevertheless, the complexity associated with the lithium-based batteries is to protect them from being exposed to moist (or ambient air) due to the high reactivity of lithium which makes packaging and encapsulation difficult [5, 40]. Further, there is still a need for a better understanding of ion dissociation and transport within a lithium cell as well as finding salts with higher conductivities, and wide electrochemical window ref.[41]. Also, there have been several attempts to reduce the formation of dendrites at the surface of lithium. A review on the issues and challenges in the development of lithium-based batteries is available in ref.[41].

Due to the difficulties associated with lithium batteries, it seems that aqueous electrolyte batteries are promising alternatives as they offer relatively low costs, high ionic conductivity (lower ohmic overpotentials), better safety, and less environmental issues [42, 43]. Albano et al. reported on the development of an integrated zinc-silver oxide primary microbattery for implantable MEMS devices [33]. They used physical vapor deposition (PVD) technique to deposit thin film layers (less than a micron) of titanium (as a sticky layer), gold (as a current collector), and silver (active electrode material) onto a glass substrate. The anode electrode material is zinc, directly sprayed on a copper foil (as a current collector) from a nanopowder zinc solution and capacities of up to $138\,\mu Ah\,cm^{-2}$ are obtained [33]. They have also emphasized that the specific capacities reported in the literature for thin film batteries ranges between 20 and $300\,\mu Ah\,cm^{-2}$ [33]. Other alternatives to lithium based batteries are nickel-based battery chemistries such as nickel zinc (Ni-Zn) and nickel metal hydride (NiMH). While Humble et al. have reported an energy density of $555\,\mu Wh\,cm^{-2}$ for a microfabricated Ni-Zn battery, the possibility of morphology change on the zinc electrode after several charge-discharge cycles still needs to be addressed [11].

The cathode electrode of a NiMH battery features $Ni(OH)_2/NiOOH$ conversion while the anode electrode consists of a metal hydride material (e.g., $LaNi_5H_6$) [44]. The overall electrochemical reaction involved in a NiMH battery cell is $NiOOH + MH \rightleftharpoons Ni(OH)_2 + M$ with a standard reversible cell potential of $1.35\,V$ [44]. Even though there have been several works on the fabrication of thin films of metal hydride materials which could be used in micro-fuel cells or micro-NiMH batteries [45, 46, 47] back in early 1980s, there are hardly works on miniaturized NiMH batteries. In 2003, Do et al. reported on a NiMH microbattery which can be fabricated using a film electrode concept. They fabricated the electrodes onto the sides of a porous substrate which is used as a separator (and support) for the battery electrodes. In their microbattery concept, the current collectors are fabricated by employing a sputtering technique while the electrode materials are screen-printed by using poly vinyl alcohol as a binder [48]. They have reported discharge capacities of around 1.17–$3.15\,mAh\,cm^{-2}$ [48, 49]. It should be emphasized that the use of a membrane as a separator increases the complexity and costs associated with the fabrication, and provides a barrier to the electrolyte ionic transport; i.e., there will be considerable additional ohmic overpotentials. This section proceeds with a brief overview on two and three dimensional microstructures used for microbattery electrodes.

1.1.3 Two dimensional (planar) and three dimensional microstructures

Generally, two different approaches have been employed to design and fabricate microbatteries including films (two-dimensional) (thin and thick films such as refs.[50, 51]), and three dimensional (3D) electrodes [52]. In the planar (two-dimensional) approach, the electrodes (and electrolytes) are fabricated as film layers and are combined to form an electrochemical cell. This approach has been extensively utilized over the last two decades to design and manufacture small batteries. Various microfabrication' techniques have been used such as sol-gel deposition (such as ref.[53]), physical vapor deposition (PVD) (such as ref.[54]), chemical vapor deposition (CVD) (such as ref.[55]), atomic layer deposition (ALD) (such as ref.[56]), electrodeposition (such as ref.[57]), and printing [58]. The latter has gained more attention as a cost-effective fabrication method which offers fast replication and prototyping such as works in refs.[59, 60, 61].

In terms of 2D electrode type microbatteries, the fabrication of lithium microbatteries with V_2O_5 thin films for both electrodes using radio-frequency (RF) magnetron sputtering method can be found in ref.[62]. Additionally, Kuwata et al. have employed a pulsed laser deposition (PLD) technique to fabricate a thin-film lithium-ion battery with an amorphous solid electrolyte for capacities up to around $8 \mu Ah\, cm^{-2}$ for a current density range of 13 to 222 $\mu A\, cm^{-2}$ [63]. Note there are a large number of works on electrode and electrolyte material improvements for lithium-ion microbatteries such as the work by Song et al. which showed that SnO_x thin films can deliver a capacity of $670\, \mu Ah\, (cm^2 \mu m)^{-1}$ at $50\, \mu A\, cm^{-2}$ in the voltage range between 0.1 and $1.2\, V$ for up to 50 cycles [64].

The three dimensional (3D) electrode approach has gained attention more recently as it offers higher energy density for the same footprint area of the battery compared to that of thin or thick film-based batteries as also emphasized by Albano et al. [33]. In a nutshell, the 3D structure is microfabricated by employing micro-lithography techniques which yield electrodes of cylindrical shapes (in an array configuration) with lengths ranging between 10 and $200\, \mu m$ and diameters of 5 to 100 μm [65].

The fabrication of a 3D microelectrode for a lithium battery by using electrophoretic deposition has been reported by Kanamura et al. [66]. They have obtained a discharge capacity of 105.4 $\mu Ah\, cm^{-2}$ for a microarray cell of $Li_4Ti_5O_{12}$/PMMA gel/lithium [66]. More recently, 3D microbattery architectures have been reported for lithium-based batteries by using printing techniques such as the work in ref.[67]. Note that the 3D architectures provide higher areal energy and power densities which can be used more effectively in microdevices [67, 68]. For instance, Ho et al. have reported on a novel ink jet printing technique to fabricate 3D zinc-silver microbatteries directly onto a substrate [69]. They have fabricated 3D arrays of pillars on a glass substrate as an electrode for an energy density of 3.95 $mWh\, cm^{-2}$. Further, Nam et al. have mentioned a novel fabrication method for electrode arrays using a self-assembled layer of virus-templated cobalt oxide nanowires which can deliver capacities ranging from 380 to $460\, nA\, h$ at a low discharge current ($26\, nA$), and from 100 to $150\, nA\, h$ at a high discharge current ($255\, nA$) [70]. Gerasopoulos et al. have also reported on the fabrication of a nano-structured nickel-zinc microbattery by using Tobacco mosaic virus (TMV), a high aspect ratio cylindrical plant virus, which delivers a capacity of $4.45\, \mu Ah\, cm^{-2}$ [32, 71].

1.2 Concluding Remarks

Micro Electro Mechanical Systems (MEMS) and microfluidics are versatile technologies. To ease the problems associated with using macroscale power sources for MEMS devices, the use of integrated power supplies, which can be fabricated by commonly-used fabrication methods of the semi-conductor industry, is promising. A review of the literature reveals that the required power depends on the type of unit and the application. Generally, the power ranges from roughly $0.1\,\mu W$ to $1000\mu W$. In terms of capacity, as an example, if we assume an operation time of around $4\,hr\,day^{-1}$ (measurement at every minute for a duration of 10 seconds) for the wireless sensor node reported by Okada et al.[14, 15] as mentioned above, a capacity of $\approx 1.7\,\mu Ah$ per day ($\approx 50\,\mu Ah$ per month) at a nominal voltage of $1.2\,V$ is required.

Even though lithium based microbatteries provide higher energy densities, there are still complications with respect to the battery packaging and encapsulation due to high reactivity of lithium when it is exposed to moist. Hence, a nickel based microbattery can be an alternative which features characteristics sufficient to fulfill the requirements in terms of power and capacity. The latter has somewhat less significance if the microbattery is coupled with an energy harvesting device (hybrid system) such as a solar cell, for instance. Generally, glass-like substrates have been commonly used to manufacture various micro(fluidic) devices and the fabrication of the entire battery cell on a glass wafer appears reasonable approach to mimic the integration of the battery onto a microfluidic device.

Therefore, this research project is aimed at the fabrication and the characterization of a rechargeable nickel metal hydride microbattery on a glass substrate. The objectives of this research work can be divided into five sections: i) characterization of materials used as electrodes of the microbattery; ii) fabrication of both positive and negative electrodes using microfabrication techniques; iii) electrochemical characterization of both positive and negative electrodes; iv) fabrication of a fluidic layer to be used as an electrolyte reservoir and electrode separator; v) assembling the entire microbattery followed by an electrochemical characterization.

1.3 Organization of Thesis

A total number of four papers have been prepared for publication. These papers are presented in chapters II to V. The objective of the first paper is to investigate and characterize the intermetallic compounds of $LaNi_5$ and $LaNi_{4.5}Co_{0.5}$ using hydrogen sorption measurements. In this paper, several models are evaluated to describe the transition between phases during (de-)hydrogenation. Also, a model based on a cumulative distribution function is introduced which can describe hydrogen sorption of the AB_5 metal alloys with four regression parameters. A comprehensive review of the models reported over the past decades is also given in this paper. Further, a model proposed by Feng and co-workers which is based on the kinetics of desorption is evaluated for $LaNi_5$ and $LaNi_{4.5}Co_{0.5}$. This approach is used to correct for overpotentials and further improve the model to describe the electrolytic hydrogenation of the intermetallic compound of AB_5 for the third paper as presented in chapter IV. The work presented in chapter II of this thesis has been published in the International Journal of Hydrogen Energy, Vol. 38, Issue 21, Pages 8838-8851 (2013) (Authors: Hamid Falahati and Dominik P.J. Barz).

The second paper is concerned with the fabrication and characterization of the positive electrode (cathode) of the microbattery. In this article, a thorough discussion is given with respect to the fabrication methods and electrochemical characterization of the nickel hydroxide film electrode. The electrode is fabricated on a glass substrate by commonly used electron beam evaporative and electrodeposition techniques. The durability of the nickel electrode is improved by using a patterning technique. The electrochemical performance of the patterned nickel hydroxide film electrode is compared with the conventionally fabricated electrode on nickel foil, and also without the pattern on a glass substrate. The work presented in chapter III of this thesis has been published in ACS Applied Materials & Interfaces, Vol. 7, Issue 23, Pages 12797-12808 (2015). (Authors: Hamid Falahati, Edward Kim and Dominik P.J. Barz).

The objectives of the work presented in the third paper (chapter IV) are to fabricate and characterize the metal hydride film electrode to be used as a negative electrode (anode) of the microbattery cell. Electron beam evaporative and sputtering techniques are used to microfabricate such films of intermetallic alloy with AB_5-type of La-Ni-Al. A model for the electrolytic (de)hydrogenation is derived which can explain the two $\alpha-$ and $\beta-$ regions along with the transition between the phases using the same kinetics approach as described in the first paper. Additionally, the results of the hydrogen sorption of aluminium-substituted $LaNi_5$ obtained in this work are compared to those of pure $LaNi_5$ previously described in the first paper with respect to the plateau pressure and activation process.

The fourth paper in this thesis is concerned with the combination of the electrodes which are fabricated in the works given in the second and third papers, in order to obtain a workable microbattery. In this work, a polymeric fluidic layer is fabricated and used as an electrolyte reservoir and electrode separator in a sandwich-like assembly. The thesis is concluded with some remarks and recommended further works.

1.4 References

[1] Jack W Judy. Microelectromechanical systems (MEMS): fabrication, design and applications. *Smart Mater. Struct.*, 10(6):1115, 2001.

[2] Nam-Trung Nguyen and Steven T Wereley. *Fundamentals and applications of microfluidics*. Artech House, 2002.

[3] Klavs F. Jensen. Microreaction engineering – is small better? *Chem. Eng. Sci.*, 56(2):293 – 303, 2001.

[4] Darwin R. Reyes, Dimitri Iossifidis, Pierre-Alain Auroux, and Andreas Manz. Micro total analysis systems. 1. introduction, theory, and technology. *Anal. Chem.*, 74(12):2623–2636, 2002.

[5] P Abgrall and A-M Gué. Lab-on-chip technologies: making a microfluidic network and coupling it into a complete microsystem–a review. *J. Micromech. Microeng.*, 17(5):R15, 2007.

[6] Paul Yager, Gonzalo J. Domingo, and John Gerdes. Point-of-care diagnostics for global health. *Annu. Rev. Biomed. Eng.*, 10(1):107–144, 2008.

[7] Betty H. Robertson and Janet K.A. Nicholson. New microbiology tools for public health and their implications1. *Annu. Rev. Public Health*, 26(1):281–302, 2005.

[8] Curtis D. Chin, Vincent Linder, and Samuel K. Sia. Lab-on-a-chip devices for global health: Past studies and future opportunities. *Lab. Chip*, 7:41–57, 2007.

[9] United nations development programme, human development report 2001: Making new technologies work for human development. Technical report, Oxford University Press, 2001.

[10] G. De Micheli. An outlook on design technologies for future integrated systems. *IEEE Transactions on Computer-Aided Design of Integrated Circuits and Systems*, 28(6):777–790, 2009.

[11] Paul H. Humble, John N. Harb, and Rodney LaFollette. Microscopic nickel-zinc batteries for use in autonomous microsystems. *J. Electrochem. Soc.*, 148(12):A1357–A1361, 2001.

[12] Robert Puers and Patrick Wouters. Adaptable interface circuits for flexible monitoring of temperature and movement. *Analog Integr. Circuits Signal Process.*, 14(3):193–206, 1997.

[13] Anantha P. Chandrakasan, Naveen Verma, and Denis C. Daly. Ultralow-power electronics for biomedical applications. *Annu. Rev. Biomedical Engineering*, 10(1):247–274, 2008. PMID: 18647116.

[14] H. Okada, T. Itoh, and T. Masuda. Development of custom CMOS LSI for ultra-low power wireless sensor node in health monitoring systems. In *Sensors, 2011 IEEE*, pages 1197–1200, Oct 2011.

[15] H. Okada, H. Nogami, T. Kobayashi, T. Masuda, and T. Itoh. Development of ultra low power wireless sensor node with piezoelectric accelerometer for health monitoring. In *Solid-State Sensors, Actuators and Microsystems (TRANSDUCERS EUROSENSORS XXVII), 2013 Transducers Eurosensors XXVII: The 17th International Conference on*, pages 26–29, June 2013.

[16] Yoonmyung Lee, B. Giridhar, Zhiyoong Foo, D. Sylvester, and D.B. Blaauw. A sub-nW multi-stage temperature compensated timer for ultra-low-power sensor nodes. *IEEE J. Solid-State Circuits*, 48(10):2511–2521, Oct 2013.

[17] K A Cook-Chennault, N Thambi, and A M Sastry. Powering MEMS portable devices–a review of non-regenerative and regenerative power supply systems with special emphasis on piezoelectric energy harvesting systems. *Smart Mater. Struct.*, 17(4):043001, 2008.

[18] Shad Roundy, Paul K. Wright, and Jan Rabaey. A study of low level vibrations as a power source for wireless sensor nodes. *Comput. Commun.*, 26(11):1131 – 1144, 2003.

[19] Kimberly Ann Cook-Chennault, Nithya Thambi, Mary Anne Bitetto, and E.B. Hameyie. Piezoelectric energy harvesting: A green and clean alternative for sustained power production. *Bulletin of Science, Technology & Society*, 28(6):496–509, 2008.

[20] Yanghua Tang, Kevin Stanley, Jonathan Wu, Dave Ghosh, and Jiujun Zhang. Design consideration of micro thin film solid-oxide fuel cells. *J. Micromech. Microeng.*, 15(9):S185, 2005.

[21] Jan Peirs, Dominiek Reynaerts, and Filip Verplaetsen. A microturbine for electric power generation. *Sens. Actuators, A*, 113(1):86 – 93, 2004.

[22] Shuji Tanaka, Takashi Yamada, Shinya Sugimoto, Jing-Feng Li, and Masayoshi Esashi. Silicon nitride ceramic-based two-dimensional microcombustor. *J. Micromech. Microeng.*, 13(3):502, 2003.

[23] S Whalen, M Thompson, D Bahr, C Richards, and R Richards. Design, fabrication and testing of the P3 micro heat engine. *Sens. Actuators, A*, 104(3):290 – 298, 2003.

[24] Jing-Quan Liu, Hua-Bin Fang, Zheng-Yi Xu, Xin-Hui Mao, Xiu-Cheng Shen, Di Chen, Hang Liao, and Bing-Chu Cai. A MEMS-based piezoelectric power generator array for vibration energy harvesting. *Microelectron. J.*, 39(5):802–806, 2008.

[25] Kien Bang Lam, Eric A Johnson, Mu Chiao, and Liwei Lin. A MEMS photosynthetic electrochemical cell powered by subcellular plant photosystems. *J. Microelectromech. Syst.*, 15(5):1243–1250, 2006.

[26] Choi D. K. Chun M.S., Shim M.S. Electrokinetic micro power cell using pile-up disk type microfluidic-chip with multi-channel, patent: US 7,709,126, 2010.

[27] Jun Yang, Fuzhi Lu, Larry W Kostiuk, and Daniel Y Kwok. Electrokinetic microchannel battery by means of electrokinetic and microfluidic phenomena. *J. Micromech. Microeng.*, 13(6):963, 2003.

[28] DJ Broer, R Penterman, E Peeters, R Kurt, D Halter, and HD Koning. Supplying power for a micro system, patent: USAPP 20110070469, PCT No.: PCT/IB09/52088, 2011.

[29] John N. Harb, Rodney M. LaFollette, Richard H. Selfridge, and Larry L. Howell. Microbatteries for self-sustained hybrid micropower supplies. *J. Power Sources*, 104(1):46 – 51, 2002.

[30] Jinkui Feng, Binggong Yan, Man O. Lai, and Lu Li. Design and fabrication of an all-solid-state thin-film Li-ion microbattery with amorphous TiO2 as the anode. *Energy Technology*, 2(4):397–400, 2014.

[31] Nana Amponsah Kyeremateng, Chrystelle Lebouin, Philippe Knauth, and Thierry Djenizian. The electrochemical behaviour of TiO2 nanotubes with Co3O4 or NiO submicron particles: Composite anode materials for Li-ion micro batteries. *Electrochim. Acta*, 88(0):814 – 820, 2013.

[32] Konstantinos Gerasopoulos, Matthew McCarthy, Elizabeth Royston, James N Culver, and Reza Ghodssi. Nanostructured nickel electrodes using the tobacco mosaic virus for microbattery applications. *J. Micromech. Microeng.*, 18(10):104003, 2008.

[33] F. Albano, Y.S. Lin, D. Blaauw, D.M. Sylvester, K.D. Wise, and A.M. Sastry. A fully integrated microbattery for an implantable microelectromechanical system. *J. Power Sources*, 185(2):1524 – 1532, 2008.

[34] Kyle T. Braam, Steven K. Volkman, and Vivek Subramanian. Characterization and optimization of a printed, primary silver-zinc battery. *J. Power Sources*, 199(0):367 – 372, 2012.

[35] D.F. Lemmerhirt and K.D. Wise. Chip-scale integration of data-gathering microsystems. *Proc. IEEE*, 94(6):1138–1159, 2006.

[36] P. Mohseni, K. Najafi, S.J. Eliades, and X. Wang. Wireless multichannel biopotential recording using an integrated FM telemetry circuit. *IEEE Trans. Neural Syst. Rehabil. Eng.*, 13(3):263–271, 2005.

[37] M.A. Alahmad and H.L. Hess. Evaluation and analysis of a new solid-state rechargeable microscale lithium battery. *IEEE Trans. Ind. Electron.*, 55(9):3391–3401, 2008.

[38] J. Pikul, H. Zhang, J. Cho, P. Braun, and W. King. High power lithium ion microbatteries with lithographically defined 3-d porous electrodes. In *IEEE 26th Intl Conf. on Micro Electro Mechanical Systems (MEMS)*, pages 857–860, 2013.

[39] H. Lhermet, C. Condemine, M. Plissonnier, R. Salot, P. Audebert, and M. Rosset. Efficient power management circuit: From thermal energy harvesting to above-IC microbattery energy storage. *IEEE J. Solid-State Circuits*, 43(1):246–255, 2008.

[40] R. Salot, S. Martin, S. Oukassi, M. Bedjaoui, and J. Ubrig. Microbattery technology overview and associated multilayer encapsulation process. *Appl. Surf. Sci.*, 256(3, Supplement):S54 – S57, 2009.

[41] J.-M. Tarascon and M. Armand. Issues and challenges facing rechargeable lithium batteries. *Nature*, 414(6861):359–367, 2001.

[42] Xue-Ping Gao and Han-Xi Yang. Multi-electron reaction materials for high energy density batteries. *Energy Environ. Sci.*, 3:174–189, 2010.

[43] Jilei Liu, Minghua Chen, Lili Zhang, Jian Jiang, Jiaxu Yan, Yizhong Huang, Jianyi Lin, Hong Jin Fan, and Ze Xiang Shen. A flexible alkaline rechargeable Ni/Fe battery based on graphene foam/carbon nanotubes hybrid film. *Nano Lett.*, 14(12):7180–7187, 2014.

[44] David Linden and Thomas B Reddy. Handbook of batteries. *New York*, 2002.

[45] H. Sakaguchi, N. Taniguchi, H. Seri, J. Shiokawa, and G. Adachi. Mechanical properties of LaNi5 thin films prepared by sputtering and vapor deposition methods and determination of the hydrogen content in these films. *J. Appl. Phys.*, 64(2):888–892, 1988.

[46] G. Adachi, H. Sakaguchi, K. Niki, N. Nagai, and J. Shimokawa. Preparation of LaNi5 films and their electrical properties under a hydrogen atmosphere. *J. Less-Common Met.*, 108(1):107 – 114, 1985.

[47] L. Huang, H. Gong, and W. Gao. Phase change of sputtered LaNi5 thin films due to hydrogenation. *Thin Solid Films*, 339(12):78 – 81, 1999.

[48] Jing-Shan Do, Sen-Hao Yu, and Suh-Fen Cheng. Thick-film nickel-metal-hydride battery based on porous ceramic substrates. *J. Power Sources*, 117(12):203 – 211, 2003.

[49] Jing-Shan Do, Sen-Hao Yu, and Suh-Fen Cheng. Preparation and characterization of thick-film Ni/MH battery. *Biosens. Bioelectron.*, 20(1):61 – 67, 2004.

[50] C Branci, N Benjelloun, J Sarradin, and M Ribes. Vitreous tin oxide-based thin film electrodes for Li-ion micro-batteries. *Solid State Ionics*, 135(14):169 – 174, 2000.

[51] N.J. Dudney and B.J. Neudecker. Solid state thin-film lithium battery systems. *Curr. Opin. Solid State Mater. Sci.*, 4(5):479 – 482, 1999.

[52] Menachem Nathan, D. Golodnitsky, V. Yufit, E. Strauss, T. Ripenbein, I. Shechtman, S. Menkin, and E. Peled. Three-dimensional thin-film li-ion microbatteries for autonomous mems. *J. Microelectromech. Syst.*, 14(5):879–885, 2005.

[53] Gabriel Oltean, Mario Valvo, Leif Nyholm, and Kristina Edström. On the electrophoretic and sol–gel deposition of active materials on aluminium rod current collectors for three-dimensional li-ion micro-batteries. *Thin Solid Films*, 562:63–69, 2014.

[54] Jeremy Freixas, Etienne Eustache, Pascal Roussel, Charlene Brillard, Dominique Deresmes, Nicolas Nuns, Nathalie Rolland, Thierry Brousse, and Christophe Lethien. Sputtered titanium nitride: A bifunctional material for Li-ion microbatteries. *J. Electrochem. Soc.*, 162(4):A493–A500, 2015.

[55] E. Biserni, M. Xie, R. Brescia, A. Scarpellini, M. Hashempour, P. Movahed, S.M. George, M. Bestetti, A. Li Bassi, and P. Bruno. Silicon algae with carbon topping as thin-film anodes for lithium-ion microbatteries by a two-step facile method. *J. Power Sources*, 274(0):252 – 259, 2015.

[56] Biqiong Wang, Jian Liu, Qian Sun, Ruying Li, Tsun-Kong Sham, and Xueliang Sun. Atomic layer deposition of lithium phosphates as solid-state electrolytes for all-solid-state microbatteries. *Nanotechnology*, 25(50):504007, 2014.

[57] Hao Liu, Hyung-Man Cho, Ying Shirley Meng, and Quan Li. Engineering three-dimensionally electrodeposited Si-on-Ni inverse opal structure for high volumetric capacity Li-ion microbattery anode. *ACS Appl. Mater. Interfaces*, 6(12):9842–9849, 2014.

[58] P-E Delannoy, B Riou, B Lestriez, D Guyomard, T Brousse, and J Le Bideau. Toward fast and cost-effective ink-jet printing of solid electrolyte for lithium microbatteries. *J. Power Sources*, 274:1085–1090, 2015.

[59] C C Ho, J W Evans, and P K Wright. Direct write dispenser printing of a zinc microbattery with an ionic liquid gel electrolyte. *J. Micromech. Microeng.*, 20(10):104009, 2010.

[60] Moon-Soo Park, Sang-Hoon Hyun, Sang-Cheol Nam, and Sung Back Cho. Performance evaluation of printed LiCoO2 cathodes with PVDF-HFP gel electrolyte for lithium ion microbatteries. *Electrochim. Acta*, 53(17):5523 – 5527, 2008.

[61] D. Steingart, C.C. Ho, J. Salminen, J.W. Evans, and P.K. Wright. Dispenser printing of solid polymer-ionic liquid electrolytes for lithium ion cells. In *6th International Conference on Polymers and Adhesives in Microelectronics and Photonics*, pages 261–264, 2007.

[62] M. Baba, N. Kumagai, H. Kobayashi, O. Nakano, and K. Nishidate. Fabrication and electrochemical characteristics of all-solid-state Lithium-Ion batteries using V2O5 thin films for both electrodes. *Electrochem. Solid-State Lett.*, 2(7):320–322, 1999.

[63] Naoaki Kuwata, Junichi Kawamura, Keisuke Toribami, Takeshi Hattori, and Noriko Sata. Thin-film lithium-ion battery with amorphous solid electrolyte fabricated by pulsed laser deposition. *Electrochem. Commun.*, 6(4):417 – 421, 2004.

[64] Jie Song, Min-Zhen Cai, Quan-Feng Dong, Ming-Sen Zheng, Qi-Hui Wu, and Sun-Tao Wu. Structural and electrochemical characterization of SnOx thin films for Li-ion microbattery. *Electrochim. Acta*, 54(10):2748 – 2753, 2009.

[65] Jeffrey W Long, Bruce Dunn, Debra R Rolison, and Henry S White. Three-dimensional battery architectures. *Chem. Rev.*, 104(10):4463–4492, 2004.

[66] Kiyoshi Kanamura, Hirokazu Munakata, and Takashi Sugiura. Fabrication of 3D microelectrodes for lithium ion batteries by electrophoretic deposition. *Functional Materials Letters*, 02(01):9–12, 2009.

[67] Ke Sun, Teng-Sing Wei, Bok Yeop Ahn, Jung Yoon Seo, Shen J Dillon, and Jennifer A Lewis. 3D printing of interdigitated Li-ion microbattery architectures. *Adv. Mater.*, 25(33):4539–4543, 2013.

[68] Jianhui Zhu, Jian Jiang, Yamin Feng, Gaoxiang Meng, Hao Ding, and Xintang Huang. Three-dimensional Ni/SnO x/C hybrid nanostructured arrays for lithium-ion microbattery anodes with enhanced areal capacity. *ACS Appl. Mater. Interfaces*, 5(7):2634–2640, 2013.

[69] C C Ho, K Murata, D A Steingart, J W Evans, and P K Wright. A super ink jet printed zinc-silver 3D microbattery. *J. Micromech. Microeng.*, 19(9):094013, 2009.

[70] Ki Tae Nam, Ryan Wartena, Pil J. Yoo, Forrest W. Liau, Yun Jung Lee, Yet-Ming Chiang, Paula T. Hammond, and Angela M. Belcher. Stamped microbattery electrodes based on self-assembled M13 viruses. *Proc. Natl. Acad. Sci. U.S.A.*, 105(45):17227–17231, 2008.

[71] Konstantinos Gerasopoulos, Ekaterina Pomerantseva, Matthew McCarthy, Adam Brown, Chunsheng Wang, James Culver, and Reza Ghodssi. Hierarchical three-dimensional microbattery electrodes combining bottom-up self-assembly and top-down micromachining. *ACS Nano*, 6(7):6422–6432, 2012.

Chapter 2

Evaluation of hydrogen sorption models for AB_5-type metal alloys by employing a gravimetric technique[1]

2.1 Abstract

This paper is concerned with hydrogen absorption and desorption in AB_5-type hydrogen storage metal alloys. We give a brief overview on models which have been proposed for hydrogen sorption in metals over the past decades. We choose three models based on different perspectives, i.e. thermodynamics, reaction kinetics, and

---

[1] This paper has been published in the International Journal of Hydrogen Energy by Elsevier (H. Falahati and D.P.J. Barz (2013), Int. J. Hydrogen Energy 38, 21, 8838-8851), Featured as Key Scientific Article in Renewable Energy Global Innovations ISSN 2291-2460 http://reginnovations.org/ 08/03/2014, 2013

mere observation (empiricism), and evaluate their applicability in order to describe the sorption behaviour. Additionally, we propose a model which is based on a cumulative distribution function. In order to evaluate the models, the hydrogen absorption and desorption isotherms of $LaNi_5$ and $LaNi_{4.5}Co_{0.5}$ are measured by means of a gravimetric technique. Nonlinear regression is performed to fit the models to experimental data. The computed model parameters are compared to values reported in the literature. Emphasis is given to the applicability of the models with respect to describing non-ideality of the plateau region and continuity/smoothness of phase transition regions.

2.2 Introduction

Hydrogen absorbing metal alloys can be used for various applications including hydrogen storage, nickel metal hydride (NiMH) battery electrodes, hydrogen purification, hydrogen sensors and catalysts [1, 2], heat pumps [3], and cooling systems [4]. This wide range of applications can be attributed to the reversibility of hydrogen gas absorption as it occurs in many materials such as crystalline AB_5-type metal alloys [5]. The class of AB_5 hydrogen absorbing metal alloys is particularly suitable not only due to its highly reversible hydrogen sorption but also low equilibrium pressure and relatively fast kinetics [6]. Hydrogen storage in metal alloys is relatively safe in comparison with pressurization [7] and requires lower input energy compared to liquefaction [8]. Additionally, the volumetric capacity of a hydrogen store can be higher, for a given hydrogen weight, when filled with a hydrogen absorbing metal alloy such as AB_5-type metal alloys [5].

For the purpose of this study, $LaNi_5$ and $LaNi_{4.5}Co_{0.5}$ are chosen due to the presence of nickel in the metal structure. Nickel has several benefits including acting as a catalyst for hydrogen dissociation which increases the reversibility of hydrogen sorption [9]. From an equilibrium perspective, the electrochemical reaction taking place at the gas-solid interface is similar to an electrolytic (electrochemical) hydrogenation at a solid-liquid interface [10]; Hence, hydrogen ab/desorption at the gas-solid interface can be utilized as a physicochemical model for the negative electrode of a NiMH battery.

The hydrogen content in a metal hydride system depends on operating temperature T and pressure P. The absorption and desorption of hydrogen in metal alloys tends to be exothermic and endothermic, respectively. Hence, a relationship which correlates the hydrogen content with T and P is very useful for the design of hydrogen storage systems; i.e. the so-called pressure-composition-temperature (P-C-T) relationship. Furthermore, the dependency also affects the reaction kinetics of the ab/desorption which can be seen in metal hydride cooling systems [4].

The mechanism of hydrogen sorption in an exemplary metal alloy is shown in Figure 2.1. In detail, Figure 2.1(a) depicts hydrogen molecules being adsorbed onto the surface of the metal alloy. The hydrogen molecules dissociate into atoms on the surface of the metal. The α-phase is the solution of hydrogen atoms and the solid metal as shown in Figure 2.1(b), while β-phase is the hydride phase in which the metal interstices are occupied by hydrogen atoms as illustrated in Figure 2.1(c). During the desorption process, the hydrogen atoms desorb from the metal bulk to reach the metal surface where they combine to hydrogen molecules. The transition from β- to α-phase occurs when the concentration of hydrogen in the bulk becomes

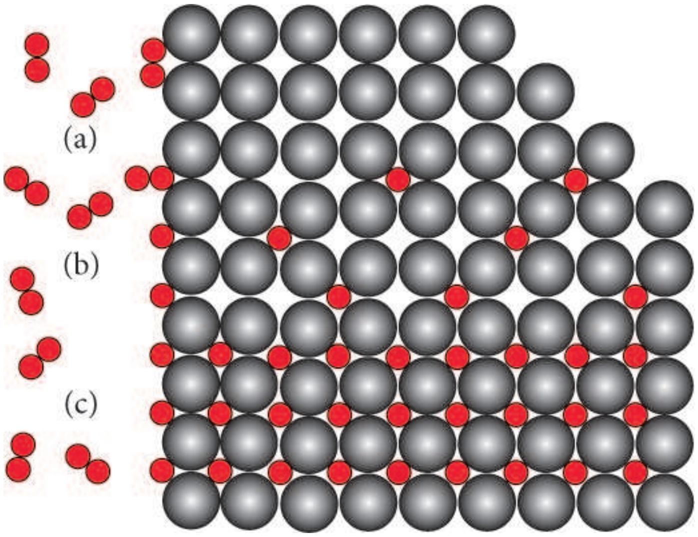

Figure 2.1: Hydrogen ab/desorption mechanism in a metal alloy: (a) adsorbed hydrogen molecules at the metal surface; (b) solid solution (α-phase); (c) hydride phase (β-phase).

too low to sustain the β-phase. It is noteworthy that the recombination of hydrogen atoms to form molecules can occur from pure β- and α-phases and also from the transition region where both phases coexist. The transition region is indicated by the plateau in the isotherm, as shown in Figure 2.2, which can be described by the van't Hoff thermodynamic model $ln(P_{eq}/P_{ref}) = \Delta S/R - \Delta H/RT$ at a given hydrogen concentration absorbed in the metal. Hence, the enthalpy ΔH and entropy ΔS of de/hydrogenation can be estimated by measuring the equilibrium hydrogen pressure P_{eq} at different temperatures and plotting its logarithmic value vs. the reciprocal temperature $1/T$.

Figure 2.2 gives an illustrative sketch of equilibrium pressure vs. hydride concentration C_H for various temperatures and indicates the transition region in each case. Generally, a higher equilibrium plateau pressure is observed at a higher temperature.

There is no mixed phase region at the so-called critical temperature, T_c. Additionally, the knowledge of the equilibrium pressure in the transition region allows for the construction of the van't Hoff plot as illustrated on the right-hand side of Figure 2.2.

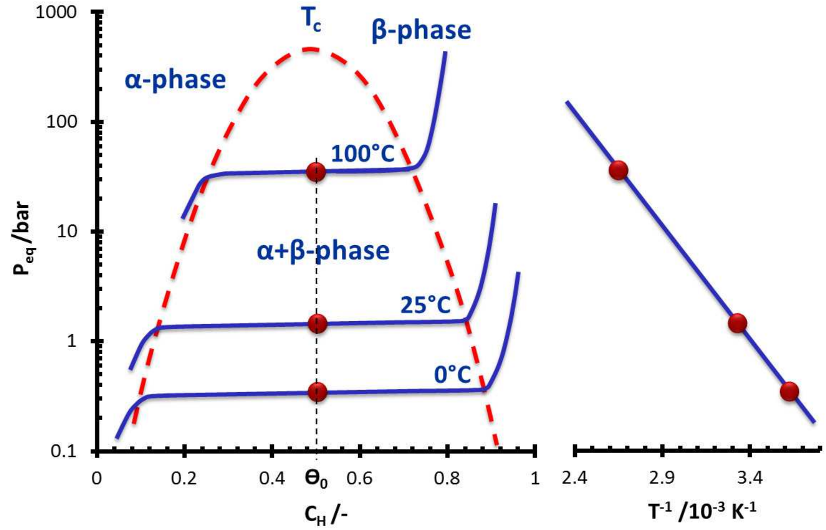

Figure 2.2: Sketch of an ideal equilibrium pressure/hydride concentration diagram for a hydrogen absorbing metal alloy indicating phases involved with hydrogen ab/desorption.

In the present study, we compare a set of three models selected from the literature along with a novel model which is based on a cumulative distribution function (CDF). In detail, we employ a gravimetric method to measure the hydrogen ab/desorption isotherms of $LaNi_5$ and $LaNi_{4.5}Co_{0.5}$ metal alloys and evaluate the applicability of the models. We proceed the article with an overview of various models known from literature. Then, the experimental setup and methodology are described. We use these data to perform nonlinear regressions to the selected models and discuss the findings. Finally, this article is summarized with some concluding remarks.

2.3 P-C-T models: An overview

Generally, the P-C-T models can be categorized into three groups: i) models which are derived from thermodynamics including statistical mechanics; ii) empirical models solely based on observation; and iii) models derived from reaction kinetics. In the following review, we give a brief overview of various models which have been proposed over the last decades. The emphasis will be on assumptions and limitations of each model.

A very first model which describes the P-C-T correlation for hydrogen absorbing materials was proposed by Lacher [11] in 1937. The Lacher model was initially proposed for palladium systems. Evans and Everett (1976) applied the model to deuterium absorption in palladium [12]. The Lacher model is primarily based on the work of Sieverts *et al.* (as cited in [11]) who discovered that the concentration of hydrogen is proportional to the square root of the hydrogen pressure. The model was derived from statistical mechanics and utilizes the Planck function which assumes a definite number of interstitial sites in the lattice. Sieverts and co-workers also assumed that the absorption energy weakly depends on the arrangement of protons in the metal interstitial sites while the total average absorption energy of a number of hydrogen atoms are at their lowest states. In the Lacher model, the hydrogen gas is described using the ideal gas law while there is no expansion, defects, dislocations and sub-lattice in the metal structure. Additionally, the plateaus are assumed to be symmetric when using Lacher model. The model is reasonably adequate for metals in which the metal lattice structure does not change due to hydrogen absorption; hence, the model cannot be applied to Ti, Zr and Ta according to Hägg (as cited in [11]).

The model also assumes that there is equilibrium between gaseous hydrogen atoms at the gas/metal interface and the hydrogen molecules in the bulk of the hydrogen gas. Furthermore, the model has the disadvantage that the heat of absorption is weakly correlated to the temperature. The Lacher model was later extended by Lototsky *et al.* [13] to obtain more realistic isotherms of metal hydride systems. In other words, the Lacher model mainly describes an idealized behaviour of hydrogen ab/desorption in metal lattices.

As the hydrogen-hydrogen (H-H) interaction contributes to the real isotherm plateaus, a correction term is required. Non-ideal behaviour had also been described by Brodowsky *et al.* (as cited in [14]), as well as the mathematical study by Griessen [15]. Real (measured) isotherm plateaus are usually not symmetric, i.e. the filling fraction θ_0 in the plateau midpoint deviates from 0.5, and may feature a slope due to the non-ideal behaviour. Moreover, the slope of the plateau region often appears to be temperature-dependent as first proposed by Shilov *et al.* (as cited in [13]). Lototsky *et al.* assumed that there should be interaction between metal-hydrogen and hydrogen-hydrogen [13]. They also noted that the most simple approach to account for the repulsive interaction is the van-der-Waals gas consideration which includes interaction between adsorbate molecules in the condensed phase. This was also considered by Hill-de Boer who studied monomolecular surface adsorption based on the model for interaction of molecules of adsorbate as mentioned by Lototsky *et al.*; a very similar approach that Langmuir used for adsorption. Lexcellent and Gondor in 2007 pointed out that the Lototsky model cannot describe the phase transformation very well [16]. The model presented by Lexcellent and Gondor is based on open two-phase systems with coherent interfaces. This requires that the reservoir is large enough that the chemical potential μ of the interstices in the reservoir does not change: i.e. $\mu_\alpha(C_\alpha) = \mu_\beta(C_\beta) = \mu_g(P_g, T)$. For further details on the thermodynamics of two-phase systems, the reader is referred to the work of Schwarz and Khachaturyan [17]. There are further models such as Beeri *et al.* [18] and Samsun *et al.* [19] which can also be considered as modifications or extensions of the Lacher model.

In the early 1950s, Rees [20] proposed a model, based on statistical mechanics, assuming that B atoms occupy interstitial sites only in the parent structure (A_mB_n). In addition, neither Schottky lattice defects nor Frenkel lattice defects were included [20]. Other work reported that the composition of any crystalline compound (of atomic lattice type) must depend, even to small degree, on the partial pressure of the components which are in equilibrium with the crystalline phase. This implies a small deviation from an ideal composition [21]. Another valid assumption is that the energy of B atoms in the interstitial sites relative to the gas phase is independent of changes in symmetry and cell dimensions of the parent lattice and the temperature as postulated by Rees [20]. On one hand, this is similar to the Lacher model in that all the solute atoms are considered to occupy interstitial sites for any part of the composition range. On the other hand, this is contrary to Anderson's model [21], in which the solute atoms are distributed among interstitial and normal lattice sites. Eventually, Rees [20] also proposed Schottky lattice defects in the parent lattice. Although the defects may reduce the number of interstitial sites accessible to atoms, the deviation from a non-defective lattice is insignificant for pure metals. However, if the hydrogen concentration is high, then there is a remarkable change in the saturation solubility for θ values approaching unity [20]. It should be emphasized that the presence of Schottky lattice defects requires a more comprehensive investigation in terms of hydrogen sorption of metal alloys.

In the early 1980s, Kierstead [22, 23] proposed a model similar to the Lacher model, though based on another derivation approach. One of the advantages of this model is that it can be easily applied to multi plateau isotherms. A general assumption is that the absorption sites can be divided into groups which are independently occupied by hydrogen. Moreover, they are maintained even though there is lattice expansion and phase changes. In addition, the heat of absorption is treated as independent of the temperature. There is confusion in literature since other works, including (hydrogen) absorption kinetics proposed by Larsen and Livesay [24], consider the heat of absorption as a temperature-dependent parameter. Symmetric plateaus are obtained when using this model. In general, the Kierstead model is very similar to the Lacher model which had been derived from statistical mechanics. The Kierstead model also considers the phase transition which is induced by attractive interactions among hydrogen atoms at the same type of site. Additionally, the interactions among hydrogen atoms at different types of sites were taken into account in the later study by Kierstead in 1984.

In the 1980s, Larsen and Livesay [24] suggested an (a semi-)empirical model based on probabilistic arguments. The model is based on nucleation and growth reactions taking place during phase transformations. This phenomenon can be described by the generalized Johnson-Mehl equation [25] which has been widely used in metallurgical applications.

In 1987, another empirical based model for P-C isotherms of hydrogen sorption in metals was proposed by Bjurström *et al.* [26]; it is called Bjurström model in this article. This model utilizes a free energy function and a Langmuir-like expression.

Bjurström *et al.* note that a Langmuir type model had previously been used for silica gel-water vapour absorption by Jury and Edwards [27]. The Bjurström model is suitable for engineering applications as it describes the isotherms with an error of a few percent only. The model has been applied to experimental data obtained for $LaNi_{4.79}Al_{0.21}$ and other metal alloys [26, 28]. Bjurström and co-workers note that experimental data in the vicinity of the critical point are not represented by their modelling approach. Furthermore, the regression of experimental data in the α-phase leads to unsatisfactory results. However, this model offers the advantage of describing the P-C-T behaviour in a single curve for all temperatures unlike Sieverts' law.

Stark *et al.* [29] and Guo *et al.* [30] studied hydrogen sorption of a metal hydride system by employing artificial neural networks; this approach can be considered as an empirical model as well [29, 30]. A polynomial regression model of ninth order has been utilized in conjunction with the van't Hoff equation by several researchers. This includes works by Jemni *et al.* in 1999 [31], Askri *et al.* [32, 33, 34, 35], and Gambini *et al.* in 2008 [36]. Even though a 9th-order polynomial regression describes the experimental data very well, the physical interpretation of the regression parameters is rather difficult. Hence, the significance of such high order polynomials is limited.

In 1993, Fujitani *et al.* introduced a concept which assigns plateau slope to a statistical distribution of the chemical potential of hydrogen in an alloy at a given temperature [37]. This can be related to heterogenous properties of the lattice including grain boundaries and lattice defects and/or composition fluctuations such as segregation [38].

Zhou *et al.* [39] proposed a model in 1994 which contains two different correlations; it will be named the Zhou model in this article. One correlation describes the segments in the P-C isotherm where the solubility of hydrogen atoms controls the ab/desorption. The other correlation describes the plateau region where the transition between α- and β-phases occurs. The Zhou model is also able to describe a slope of the plateau region implying non-ideality of the isotherms. Furthermore, the model parameters have physical meaning. In 2009, Payá *et al.* proposed an extension to Zhou model which reflects the transition points [40]. However, this modified correlation has not yet been tested with other materials to prove the general applicability of the extension.

Feng *et al.* introduced a model using a chemical reaction approach; we call it the Feng model in this article. The model is derived for the desorption process but describes the absorption process as well [14]. In detail, the model utilizes two first-order reaction kinetics of the transition of hydrogen from the absorbed to the adsorbed phase and the desorption from the metal alloy surface. Feng and co-workers considered these reactions as rate-limiting steps which is contrary to the work of others. The works of Boser [41] and Miyamoto [42] indicate that the rate-limiting step is the reaction between hydrogen atoms and α-phase solution at the interface of these two phases. In contrast, Tanaka [43] reports that the rate-limiting step is hydrogen diffusion through the β-phase while the work of Wallace [44] identifies the adsorption of hydrogen onto the metal surface. Other work determines the dissociative chemisorption of the hydrogen molecules on the AB_5 metal alloy surface as the rate-limiting step [45]. The assumption made in the Feng model is close to the one reported by Park and Lee [46], who suggested that the rate-limiting step may change with the extent of the absorption process. Furthermore, the 2012 study by Payá *et al.* indicates that the change in the rate-limiting step occurs at the transition from the plateau region to the $\beta-$phase [47].

One of the advantages of the Feng model is that hydrogen-hydrogen interaction is considered by a Temkin isotherm which was proposed for heterogenous surfaces [14]. Additionally, Feng and co-workers note that there are significant similarities between their model developed for electrochemical systems [48] and their model developed by considering phenomena at the interface of hydrogen gas and solid [14].

In the present study, one model is chosen from each category for the sake of comparison. Additionally, we propose a novel model which is based on a cumulative distribution function (CDF). Our work intends to give more insights into the applicability of the models for AB_5-type of hydrogen absorbing metal alloys. Therefore, a series of ab/desorption experiments are conducted as described in the next section.

2.4 Experimental methods and materials

In this section, we first give a brief introduction to the experimental setup which is utilized for measuring the hydrogen ab/desorption of the metal alloys. We then introduce the materials that are used and eventually describe the metal hydride activation method.

2.4.1 Gravimetric analysis

The hydrogen absorption and desorption isotherms are obtained by employing a gravimetric technique. A schematic diagram of the experimental setup, which is built in-house, is shown in Figure 2.3. The experimental setup consists of a gravimetric instrument, equipment to adjust and control gas temperature and pressure, and vacuum pumps equipped with vacuum pressure gauges. The gravimetric instrument is capable of measuring weight increase and decrease due to ab/desorption within the pressure and temperature range of 0 and 50 bar and ambient temperature to 100 $^\circ C$, respectively. The sensitivity of the gravimetric balance is 0.1 μg.

Contrary to a volumetric analysis, based on Sievert's law, a gravimetric method is more reliable even if there is a gas leakage in the instrument particularly at high pressures. The gravimetric method measures the hydrogen content by monitoring the weight increase via a microbalance. A high precision pressure transducer/transmitter (35.5 bar-ASHCROFT USA, 0.5% accuracy), which is coupled with a multimeter (Fluke 8840A, USA), measures the hydrogen pressure in the sample cells. Sample cells are equipped with two separate electrical heating tapes. The temperature of the sample cells is continuously controlled by utilizing two T-type exposed thermocouples (OMEGA, Engineering Inc., USA) which are connected to proportional-integral-derivative (PID) controllers (Barnant Company, USA and Digi-Sense, Singapore). The microbalance is calibrated prior to any measurement.

To measure the hydrogen absorption, a sample of about 4 g of metal alloy is loaded into a sample cell. The other sample cell contains a counterweight (glass beads) which does not absorb hydrogen. Then, the system is evacuated by employing two vacuum pumps. One of the vacuum pumps is a mechanical pump (Edwards, UK) and the other one is a vapour pump (Edwards, UK E0 40/55). A vacuum pressure of lower than 10^{-5} bar is obtained at the beginning of the experiment. The instrument is filled with ultra high purity hydrogen gas at a desired pressure. The weight increase is monitored through a DISBAL data acquisition system (CI Electronics ltd., UK) which is connected to the microbalance. All weight difference values are obtained after the pressure and temperature of the sample reach steady state. That is, the metal hydride is in equilibrium with its hydrogen environment.

In the desorption process, the hydrogen pressure is controlled by venting the hydrogen out via a vent needle valve. The weight decrease is read using the DISBAL data acquisition system. The hydrogen pressure reduction is repeated until an entire desorption isotherm is obtained. Weight differences are recorded if the metal hydride is in equilibrium with the hydrogen environment. We calculate the effect of buoyancy on the weight differences by using Archimedes' principle as we employ a different material for the counterweight. Additionally, we explore the buoyancy effect on the weight readings experimentally by changing the counterweight materials. These experiments are performed using nitrogen gas which gives higher buoyancy effect compared to hydrogen gas. As a result, we measure that the relative effect of buoyancy is negligible – that is, on the order of 10^{-3} relative error – over the temperature and pressure range studied. The hydrogen sorption isotherms are obtained at four different temperatures starting at room temperature with an interval of 20 $^{\circ}C$.

The $LaNi_5$ and $LaNi_{4.5}Co_{0.5}$ hydrogen storage grade metal alloys are purchased from Sigma Aldrich, Canada. Initially, the metal alloys are in the form of large particles featuring a wide particle size distribution. Ultra high purity hydrogen gas is used in all experiments (Grade 5-MEGS, Canada).

2.4.2 Metal alloy activation

An oxide layer is formed on the metal alloy surface when it is exposed to air which acts as a barrier to hydrogen ab/desorption. Hence, the removal of the oxide layer is

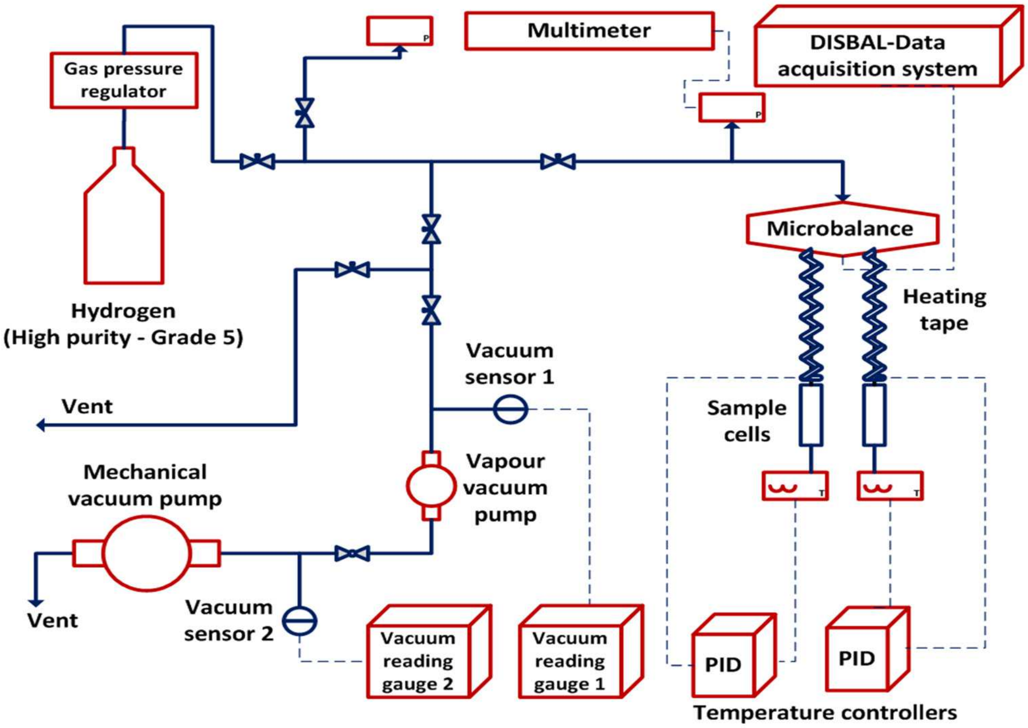

Figure 2.3: Schematic diagram of the experimental setup.

necessary to obtain bare surfaces which then can adsorb hydrogen. The removal of this oxide layer is called activation in the context of this work. The activation plays a very important role in obtaining reliable values for both absorption and desorption isotherms. The procedure used to activate the metal alloys is as follows.

The sample is loaded into the sample cell of the gravimetric instrument and maintained for three days at a temperature and pressure of 180 $^{\circ}C$ and 30 bar, respectively. Then, the sample is cooled down to ambient temperature while the hydrogen pressure is maintained at 30 bar for another three days. A few absorption and desorption cycles, as mentioned above, are performed during heating and cooling the samples. Since the metal alloys used in this study have crystalline structure, large particles are broken into very small particles (fine powder); and the alloy starts to readily absorb hydrogen. This behaviour can be seen for most crystalline materials but not for amorphous structures [49]. We observe that the activation of $LaNi_{4.5}Co_{0.5}$ metal alloy is easier to achieve than that of $LaNi_5$ which is probably due to its lower equilibrium pressure. This might also be related to the presence of cobalt in the structure of the metal alloy. In order to make sure that the alloys are fully activated, a set of five absorption and desorption cycles are performed without unloading the sample cell and the results are compared. We consider the metal alloys as entirely activated if there is no significant difference between the measured cycles.

In the next section, we evaluate the Zhou, Bjurström and Feng models along with a novel model based on CDF for $LaNi_5$ and $LaNi_{4.5}Co_{0.5}$ hydrogen storage grade metal alloys.

2.5 Results and Discussion

To evaluate and compare the mathematical models selected for this study, the models are fitted to the experimental results by using the minimization of the sum of the squared residuals. The model parameters are computed by using the Generalized-Reduced-Gradient (GRG) method for optimizing nonlinear problems.

2.5.1 Zhou Model

The model which is proposed by Zhou *et al.* [39] is comprised of two equations to describe the ab/desorption isotherms. The α- and β-phases are modelled with the correlation:

$$C_H = A\left(\frac{P_{eq}}{P_{ref}}\right)^{\gamma/2} \exp\left(-\frac{\gamma V_H P_{eq}}{RT}\right) \exp\left(-\frac{\gamma \Delta H_s}{RT}\right) \tag{2.1}$$

while

$$\ln\left(\frac{P_{eq}}{P_{ref}}\right) = \frac{\Delta S}{R} - \frac{\Delta H}{RT} + \left(f_{s,298} + k(T - 298K)\right)\left(C_H - C_{mid}\right) \tag{2.2}$$

describes the transition between $\alpha-$ and β-phase. Here, C_H and C_{mid} are the hydrogen concentration at any point and at the mid-point of the segment of the plateau with the smallest slope, respectively; P_{eq} is the equilibrium hydrogen pressure; P_{ref} is the reference pressure defined as unit pressure ($\equiv$ 1 bar); γ is the activity coefficient of hydrogen; V_H is the hydrogen partial molar volume; ΔH is the enthalpy of de/hydrogenation; ΔH_s is the heat of solution of hydrogen; ΔS is the entropy change; f_s is the slope factor of the non-ideal transition region at 298 K; k is the rate variation of the slope factor as a function of temperature; T is the absolute temperature; R is the universal gas constant in $J\,mol^{-1}K^{-1}$; and A is a regression coefficient. Eventually, the model requires the regression of twelve parameters to describe all phases.

In the current investigation, the Zhou model is fitted to experimental data obtained for $LaNi_5$ and $LaNi_{4.5}Co_{0.5}$ as shown in Figures. 2.4 and 2.5. We plot the logarithm of the concentration and the equilibrium pressure since we obtain an improved illustration of the α-phase. The indicated segments 1, 2 and 3 correspond to $\alpha-$, $\alpha+\beta-$, and $\beta-$phases, respectively. The computed values of the model parameters are given in Table 2.1. An inspection of the results show that enthalpy and

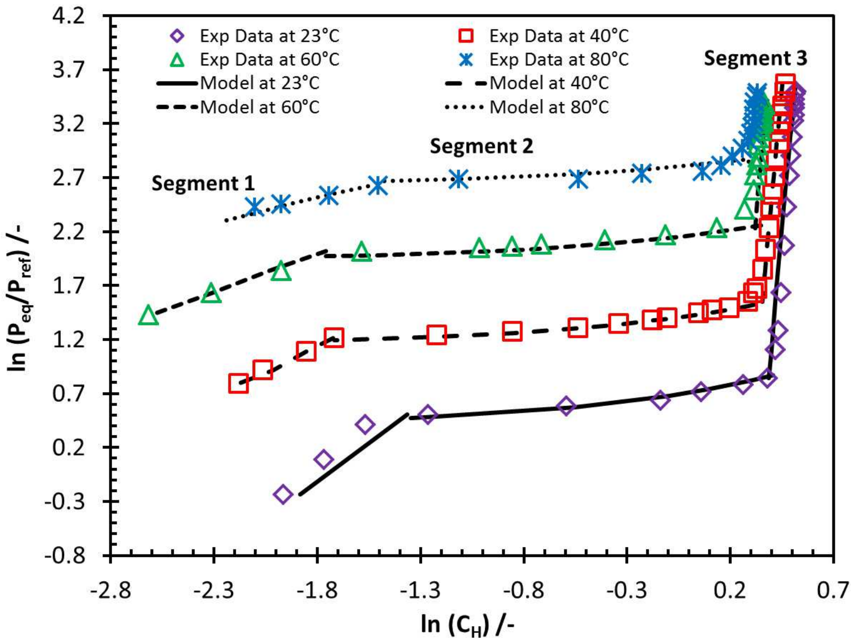

Figure 2.4: Zhou model: Desorption P-C isotherms of $LaNi_5$ metal alloy.

entropy change of hydrogen sorption of $LaNi_{4.5}Co_{0.5}$ are higher than those of $LaNi_5$. In general, somewhat higher enthalpy and entropy values for desorption process are obtained. This also emphasises that relatively small hysteresis in both metal alloys exist.

Zhou *et al.* [50, 39] and Payá *et al.* [40] also test the quality of the Zhou model for AB-, AB_2-, and AB_5-type metal alloys. The latter group, however, fits the experimental data obtained from AB_2- and AB_5-type alloys to the "modified" Zhou model which is mentioned in the overview section 2.3. Payá *et al.* have obtained a good regression quality of the fitted data for their AB_5-type alloys [40]. Contrary to the "modified" Zhou model, the original one used in [39] shows smooth continuity for the phase transition regions despite the fact that this model consists of two different correlations. Additionally, the inadequacy of the "modified" Zhou model in describing

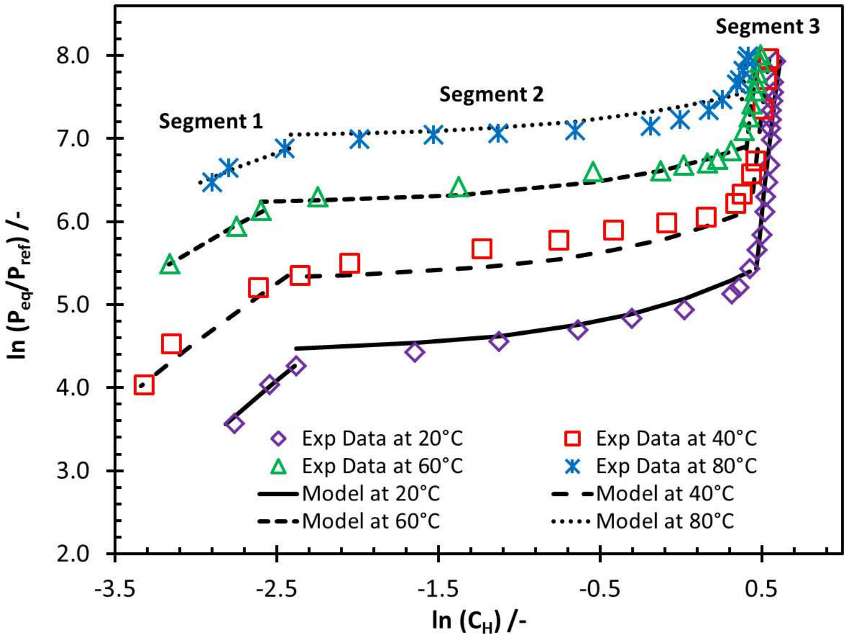

Figure 2.5: Zhou model: Desorption P-C isotherms of $LaNi_{4.5}Co_{0.5}$ metal alloy.

the α-phase, as can be seen in the work of Payá *et al.* [40], cannot clearly be seen in the current work for the original Zhou model.

As shown in Figures 2.4 and 2.5, the quality of the regression is good for both investigated metal alloys. The results clarify that the Zhou model is capable of describing the plateau region well for the temperature range studied in this work. Moreover, the model allows for the description of the non-ideality of the plateau region, i.e. for plateaus which feature a slope. It is found that the activity coefficient of hydrogen γ calculated for both metal alloys are at the same order of magnitude. However, all V_H are negative which does not have physical meaning. The absolute values of V_H for $LaNi_5$ are much larger than those of $LaNi_{4.5}Co_{0.5}$ for both α- and β- phases.

Overall, the Zhou model represents all phase regions with an accuracy sufficient for engineering applications. However, the major disadvantage of the model is that it consists of two equations and a seamless transition between the phases is not possible.

	$LaNi_5$	$LaNi_5$	$LaNi_{4.5}Co_{0.5}$	$LaNi_{4.5}Co_{0.5}$
Parameters	Absorption	Desorption	Absorption	Desorption
A_α [-]	5.26E-05	2.32E-09	2.13E-07	3.30E-09
γ_α [-]	0.72	1.03	1.58	1.11
$V_{H\alpha}$ $[L\,mol^{-1}]$	-209.85	-392.78	0.04	-2.61
$\Delta H_{S\alpha}$ $[kJ\,mol^{-1}]$	-25.25	-43.04	-14.03	-32.50
$(f_s)_{298}$ [-]	0.46	0.31	0.45	0.64
k $[K^{-1}]$	-0.004	-0.002	-0.003	-0.005
A_β [-]	0.46	0.44	0.26	0.36
γ_β [-]	0.07	0.09	0.10	0.10
$V_{H\beta}$ $[L\,mol^{-1}]$	-6.03	-10.00	-0.46	-0.28
$\Delta H_{S\beta}$ $[kJ\,mol^{-1}]$	-37.90	-32.91	-36.22	-32.50
$\|\Delta H\|$ $[kJ\,mol^{-1}]$	28.81	31.82	29.99	35.07
$\|\Delta S\|$ $[J\,mol^{-1}\,K^{-1}]$	107.41	113.09	146.02	159.89

Table 2.1: Zhou model parameters for $LaNi_5$ and $LaNi_{4.5}Co_{0.5}$ metal alloys.

2.5.2 Empirical models

In this section, we investigate two empirical models. The first model has been proposed by Bjurström *et al.* in 1987. The other model is developed within the context of this work and is based on a cumulative distribution function (CDF). In general, a noteworthy observation is that all P-C isotherms can collapse to a single characteristic curve if the equilibrium pressures are scaled with an appropriate reference pressure P_{ref}. This idea of scaled equilibrium pressures has been proposed by Bjurström *et al.* [26]; they choose a pressure scale which corresponds to the midpoint of the isotherm plateau. Initially, this method has been adapted in this paper. The results which have been achieved were not satisfactory. This might be due to the fact that the isotherm plateaus in the work of Bjurström *et al.* are symmetric contrary to ours. Hence, we expand this concept and introduce a temperature-dependent pressure scale in order to obtain a single curve of (collapsed) experimental data. In order to obtain the best possible collapse, we optimize the pressure scale by employing a regression method.

Figure 2.6 shows the results of the optimizations (and a corresponding linear fit) as a function of temperature for both metal alloys. We observe a good linearity for the temperature dependency of the pressure scale. Additionally, Figure 2.6 clarifies that the pressure scale significantly changes over the temperature. The temperature dependency of the pressure scale is more pronounced for non-symmetric isotherm plateaus. We observe that the values of absorption P-C isotherms are higher than those of desorption ones; which is an indicator for the presence of hysteresis during the ab/desorption cycle. Finally, we propose the utilization of the pressures scales as the temperature-dependent reference pressure. This reference pressure is used to scale the equilibrium pressures of each isotherm individually. In the following sections, we use the reference pressure values to test both the Bjurström and the novel CDF model.

Bjurström model

The model proposed by Bjurström *et al.* [26] is an empirical model which comprises six regression coefficients as given in Eq.(4.3):

$$C_H = a_1 \frac{a_2 X^{1/a_3}}{1 + a_2 X^{1/a_3}} + a_4 \frac{a_5 X^{1/a_6}}{1 + a_5 X^{1/a_6}} \tag{2.3}$$

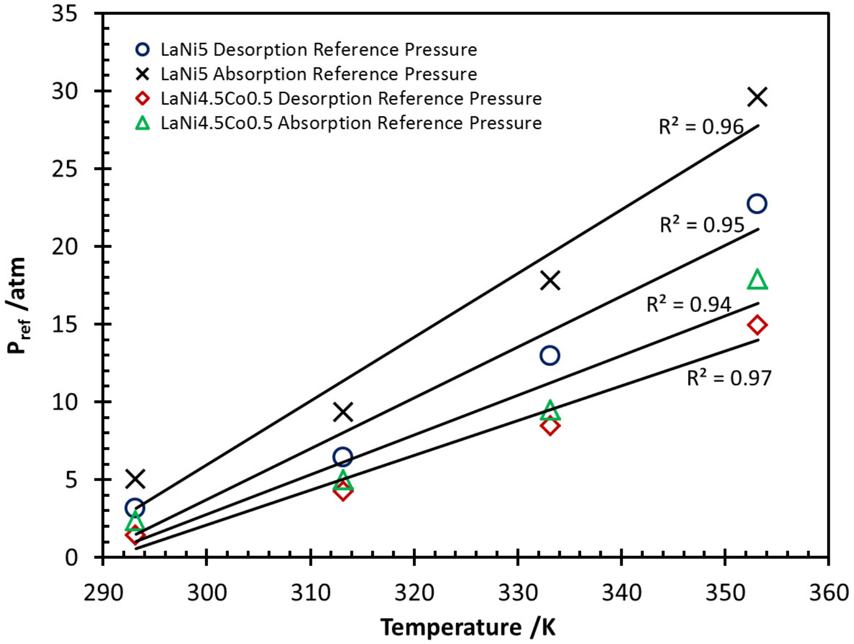

Figure 2.6: Reference pressure representing ”best-collapsed” experimental data vs. temperature.

Here, X is the equilibrium pressure P_{eq} scaled with a reference pressure P_{ref} according to $X = (P_{eq}/P_{ref})^{RT}$, C_H is the metal hydride concentration, a_i for $i = 1..6$ are the regression coefficients, T is the absolute temperature, and R is the universal gas constant in $L\,atm\,(mol\,K)^{-1}$.

The experimental data is scaled with the maximum metal hydride concentration at its corresponding temperature. The model is used to describe the experimental values obtained for $LaNi_5$ and $LaNi_{4.5}Co_{0.5}$ as shown in Figure 2.7 and Figure 2.8, respectively. The used reference pressure values correspond to those given in Figure 2.6. However, the range of experimental data is different for each isotherm which has to be considered for the regression. Hence, in terms of empirical models, regression is only performed where all isotherm experimental data are present in the collapsed curve. In the range of fewer temperature data, the regression function is given by a dashed line to indicate that the model is used for extrapolation. The computed regression coefficients are given in Table 2.

	$LaNi_5$	$LaNi_5$	$LaNi_{4.5}Co_{0.5}$	$LaNi_{4.5}Co_{0.5}$
Parameter	Absorption	Desorption	Absorption	Desorption
a_1 [-]	0.90	0.88	0.73	0.78
a_2 [-]	76.61	486.08	10.81	5.36
a_3 $[L\,atm\,mol^{-1}]$	2.36	1.95	1.90	2.58
a_4 [-]	0.09	0.10	0.27	0.23
a_5 [-]	5.00	4.00	0.81	0.58
a_6 $[L\,atm\,mol^{-1}]$	43.12	41.84	13.67	14.29

Table 2.2: Bjurström model parameters for $LaNi_5$ and $LaNi_{4.5}Co_{0.5}$ metal alloys.

Generally, the parameters of the empirical model do not provide physicochemical data such as enthalpy or entropy of (de-)hydrogenation. When we compare the regression coefficients of ab- and desorption isotherms, we find mainly similar values for $LaNi_{4.5}Co_{0.5}$ which indicates the good reversibility of this alloy. When we compare between the two different alloys, we realize that the respective a_1, a_3 and a_4 values are relatively similar. One order of magnitude difference among the a_2 values and among the a_5 values of the alloys is found, though. However, the model parameters strongly depend on the choice of the reference pressure values.

As can be seen in Figure 2.7, the model reflects the hydrogen sorption processes on $LaNi_5$ in the α-phase and in the transition region with a very good agreement while there are some inaccuracies in the β-phase. When we inspect Figure 2.8, which gives the $LaNi_{4.5}Co_{0.5}$ experimental and modelled data, we find that α- and transition region show very good agreement as well. Additionally, the model shows fairly good agreement with the experimental data of the β-phase.

Bjurström and co-workers have shown that the model represents the experimental data very well for cases where two hydrogen atoms bound to AB_5-type metal alloy [26]; however, this may not always be the case. Again, the choice of the reference pressure is crucial to obtain a high accuracy. In the present study, the accuracy is considerably higher when the regression-based temperature-dependent reference pressures are used. Furthermore, better regression can be obtained if the regression coefficients are calculated for each P-C isotherm [26], i.e. non-collapsed curves. This would result in a large number of model parameters, though. Eventually, this empirical model can be employed where a high degree of accuracy is not required, e.g. for most engineering applications.

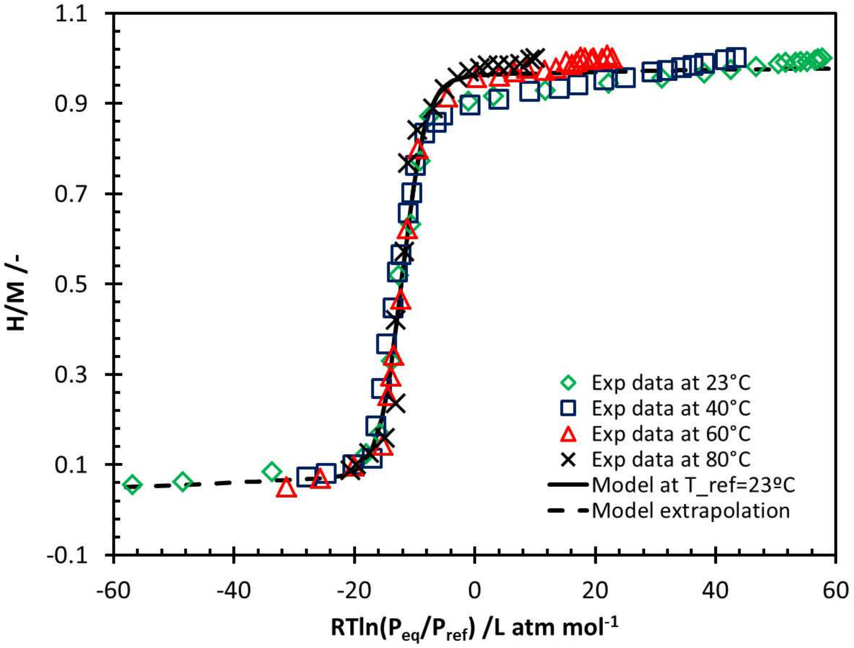

Figure 2.7: Bjurström model: Desorption P-C isotherms of $LaNi_5$ metal alloy.

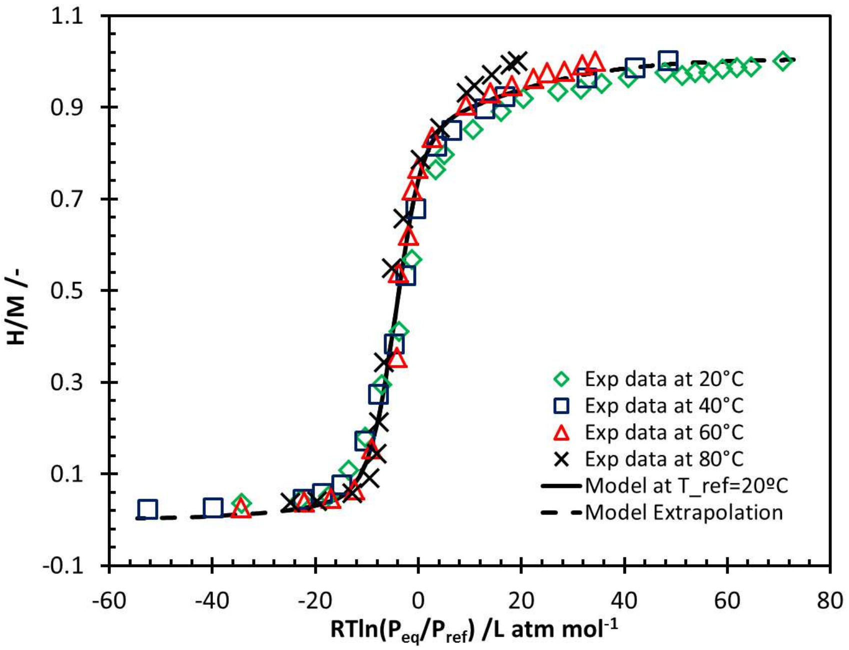

Figure 2.8: Bjurström model: Desorption P-C isotherms of $LaNi_{4.5}Co_{0.5}$ metal alloy.

A model based on a cumulative distribution function

In this section, we introduce an empirical model to represent experimental sorption data which is based on a cumulative distribution function (CDF). In detail, the model is used to describe a single curve of collapsed experimental data as it results from scaling of the equilibrium pressure (cf. section 2.5.2). We refer to this model as ERF model as it consists of an error function. The inspiration for this approach comes from modelling of breakthrough curves in ad/desorption systems as it can be found for instance in [51, 52]. The ERF model consists of four regression parameters according to

$$\frac{C_H}{C_m} = \Omega_1 \left[\Omega_2 + ERF \left(\frac{RT_{ref} \ln \left(\frac{P_{eq}}{P_{ref}} \right) + \Omega_3}{\Omega_4} \right) \right]. \tag{2.4}$$

Here, C_H and C_m are the metal hydride concentration and the maximum metal hydride concentration, respectively; P_{eq} and P_{ref} are equilibrium and reference pressure, respectively; T_{ref} is an absolute reference temperature; R is universal gas constant in $L\,atm\,K^{-1}mol^{-1}$; and Ω_i for $i = 1..4$ are the regression coefficients. In this model, Ω_3 and Ω_4 correspond to the mean μ and variance $\sqrt{\sigma^2}$ in the original CDF.

The reference conditions (T_{ref}, P_{ref}) are chosen to be room temperature (293 K) and temperature dependent reference pressure as shown in Figure 2.6. The model and experimental data points are compared in Figures 2.9 and 2.10 for the desorption of $LaNi_5$ and $LaNi_{4.5}Co_{0.5}$ metal alloys, respectively. Generally, this model requires a relatively high resolution of experimental points in the transition range to obtain a good regression quality. Since we use collapsed data, we have to perform the regression in a range where all temperatures are represented. This range is indicated by solid lines in the following figures. Hence, the ranges where we do not have all temperatures are extrapolated and indicated by dashed lines.

Figures 2.9 and 2.10 demonstrate that the model is able to represent α-phase and non-ideal plateau regions with a good agreement. Moreover, the model describes the smooth transition between the phases well. In terms of β-phase, we find lower accuracy, though it should be still adequate for technical applications. Eventually, the model parameters can also be computed for each P-C isotherm in order to obtain higher accuracies.

Table 2.3 shows the model parameters which are computed from the regression. We see that there are only small differences between the regression coefficients of the ab- and desorption process (for a metal alloy) for all parameters except Ω_4. The Ω_4

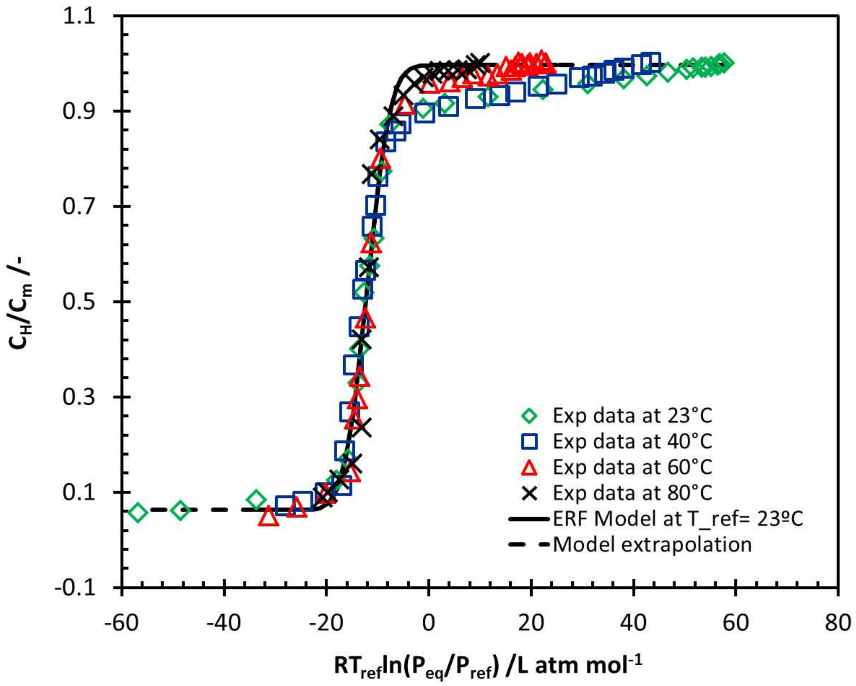

Figure 2.9: ERF model: Desorption P-C isotherms of $LaNi_5$ metal alloys.

parameter corresponds to the variance in the CDF and contributes to the slope of the transition phase. As can be seen in Figure 2.10, the plateau region of $LaNi_5$ features a larger slope in comparison with that of $LaNi_{4.5}Co_{0.5}$. This is also reflected in the regression parameters, as the value of Ω_4 for $LaNi_5$ is larger than that of $LaNi_{4.5}Co_{0.5}$. Furthermore, the presence of small hysteresis can be referred to the difference between Ω_3 values in sorption P-C isotherms of both metal alloys since Ω_3 corresponds to the mean μ in the original CDF. In fact, the mean μ contributes to the positioning of the CDF curve along the abscissa. Eventually, we find that difference in Ω_3 is larger for $LaNi_5$ which agrees with the observation of larger hysteresis for this alloy.

One considerable advantage of the empirical ERF model is that it is not restricted

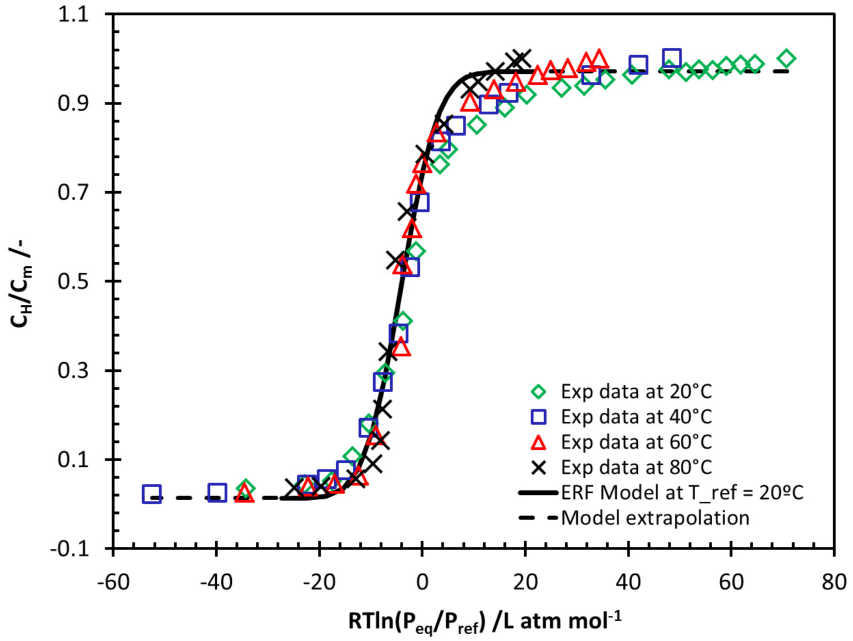

Figure 2.10: ERF model: Desorption P-C isotherms of $LaNi_{4.5}Co_{0.5}$ metal alloys.

to a single P-C isotherm. Since it utilizes collapsed experimental data resulting from scaling with a temperature-dependent reference pressure, it is able to represent P-C data for various temperatures in a single characteristic curve. In comparison to the Bjurström model, our approach offers the advantage of four regression coefficients only.

	$LaNi_5$	$LaNi_5$	$LaNi_{4.5}Co_{0.5}$	$LaNi_{4.5}Co_{0.5}$
Parameter	Absorption	Desorption	Absorption	Desorption
Ω_1 [-]	0.47	0.47	0.47	0.48
Ω_2 [-]	1.14	1.13	1.06	1.03
Ω_3 $[L\,atm\,mol^{-1}]$	10.24	12.06	4.24	4.02
Ω_4 $[L\,atm\,mol^{-1}]$	5.70	24.77	6.66	7.98

Table 2.3: ERF model parameters for $LaNi_5$ and $LaNi_{4.5}Co_{0.5}$ metal alloys.

2.5.3 Feng model

The Feng model is based on the kinetics of desorption of hydrogen in the metal alloy [14]. It is:

$$RT\ln\left(\frac{P_{eq}}{P_{ref}}\right) = \frac{2}{y_0 - x_0}\left(A + RT\ln\left(\frac{C_H}{C_m - C_H}\right) + \frac{\gamma^H C_H}{C_m}\right), \tag{2.5}$$

where A can be expressed according to

$$A = \Delta H + RT\ln\left(\frac{k_1^0 k_2^0}{k_{-1}^0 k_{-2}^0}\right). \tag{2.6}$$

Here, P_{eq} and P_{ref} ($\equiv\ 1\,atm$) are equilibrium and reference pressure, respectively; T is the absolute temperature; C_H and C_m are hydrogen concentration in mol/mol and maximum metal hydride concentration, respectively; $RT\ln\left(P_{eq}/P_{ref}\right)$ and $RT\ln(C_H/(C_m - C_H))$ can be regarded as Gibbs energy and configurational entropy, respectively [14]; $\gamma^H C_H/Cm$ is the attractive interaction coefficient of H-H absorbed; $\frac{k_1^0 k_2^0}{k_{-1}^0 k_{-2}^0}$ is the ratio of the products of the reaction rate constants of the 2-step forward reaction to the product of the corresponding reverse reaction; and R is the universal gas constant in $J\ K^{-1}mol^{-1}$.

Feng and co-workers investigated both the electrolytic hydrogenation (liquid-solid interface) and the hydrogen absorption (gas-solid interface). They found that both phenomena can be described with similar models [2]. This has several implications. For instance, the physicochemical gas-solid model can be used to investigate electrolytic de/hydrogenation of metal hydride electrodes in a NiMH battery.

We follow the original approach, and scale all metal hydride concentrations with the maximum hydrogen concentration which can be stored at room temperature. In the original Feng model, the value of y_0 and x_0 are maximum and minimum solubility of hydrogen in α- and β-phase, respectively, which are determined using the experimental P-C-T data. However, we cannot achieve a satisfactory regression quality when we use $y_0 - x_0$ resulting from our experiments. Hence, we treat the term $y_0 - x_0$ as a model regression parameter.

The regression coefficients are computed and given in Tables 2.4 and 2.5. Feng *et al.* plotted the model parameter A vs. the absolute temperature and calculated the enthalpy for hydrogen ab/desorption ΔH from the ordinate intercept divided by the average of $\frac{y_0 - x_0}{2}$ at all investigated temperatures. It turns out that we cannot achieve meaningful values by using this approach. Therefore, we revise equation (4.6) and replace coefficient A with A_0RT where the value and units of both terms are identical. The difference is that regression coefficient A_0 is now dimensionless. We obtain meaningful values when we divide the ordinate intercept of the plot A_0 vs. the temperature with the average of $\frac{1}{y_0 - x_0}$ and then multiply with RT_{mean}; where T_{mean} corresponds to the average of the investigated temperatures; i.e. 324 K. We give the enthalpy values in Table 2.6 together with enthalpy values found in literature for the sake of comparison.

T $[^\circ C]$	C_m $[-]$	$y_0 - x_0$ $[-]$	A $[kJ\,(mol H_2)^{-1}]$	γ^H / C_m $[kJ\,(mol\, H_2)^{-1}]$
23±1.5	1.03	0.90	6.39	-10.80
40±1	0.95	2.93	10.12	-9.47
60±1	0.89	4.70	18.55	-10.36
80±2	0.83	10.66	46.14	-8.84

Table 2.4: Feng model parameters for $LaNi_5$ metal alloy, for hydrogen desorption process.

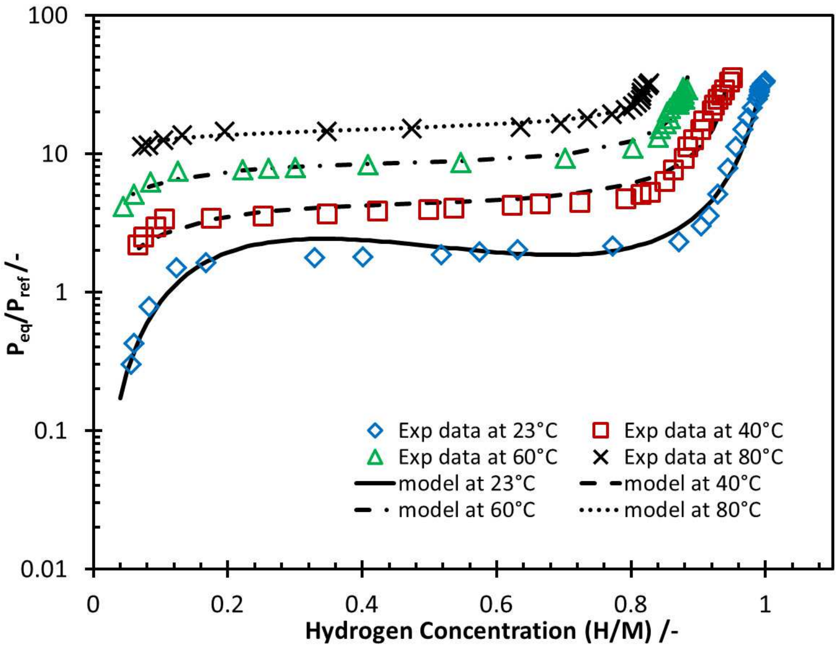

Figure 2.11: Feng model: Desorption P-C isotherms of $LaNi_5$ metal alloy.

T $[^\circ C]$	C_m $[-]$	$y_0 - x_0$ $[-]$	A $[kJ\,(mol\,H_2)^{-1}]$	γ^H/Cm $[kJ\,(mol\,H_2)^{-1}]$
20±1	1.00	1.88	5.85	-9.48
40±1	0.96	2.95	10.17	-9.73
60±1	0.91	4.57	17.46	-9.74
80±2	0.84	9.54	39.59	-9.00

Table 2.5: Feng model parameters for $LaNi_{4.5}Co_{0.5}$ metal alloy, for hydrogen desorption process.

As can be seen in Figures 2.11 and 2.12, the Feng model is able to describe the experimental data very well in all regions. The model accounts for the non-ideality of the plateau regions which feature slopes and are slightly curved. Additionally, the model is able to reflect the transition between the phases very smoothly. The model could also represent collapsed experimental data (results not shown) leading

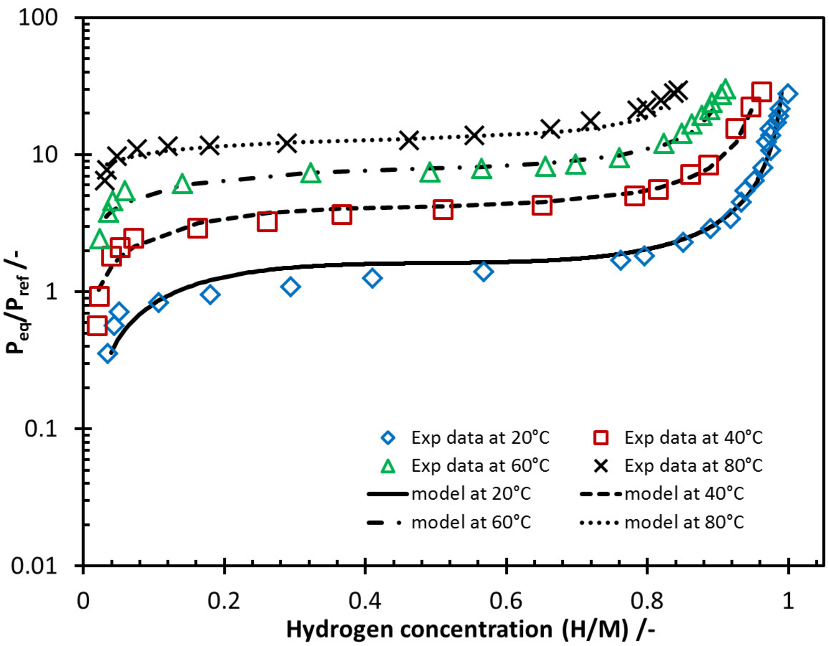

Figure 2.12: Feng model: Desorption P-C isotherms of $LaNi_{4.5}Co_{0.5}$ metal alloy.

to a reduced number of regression parameters. However, we have to treat the $y_0 - x_0$ as a regression coefficient in order to achieve an acceptable regression quality. The definition of $y_0 - x_0$ constitutes that these values should be always approximately one. The computed values can be considerably higher, especially for higher temperatures. Additionally, meaningful enthalpies are only derived when we considerably deviate from the procedure suggested in [14]. The reason behind this discrepancy is unknown. Payá *et al.* mentioned that the Feng model should not be used for isotherms at higher temperatures [40].

2.5.4 Enthalpy and entropy of hydrogen ab/desorption

Eventually, we compare the enthalpy and entropy values, which are calculated using the models studied in this work, to values that we found in literature. The values are given in Tables 2.6 and 2.7.

Enthalpy $[kJ\,(mol\,H_2)^{-1}]$	$LaNi_5$ Absorption	$LaNi_5$ Desorption	$LaNi_{4.5}Co_{0.5}$ Absorption	$LaNi_{4.5}Co_{0.5}$ Desorption	Ref.
$\|\Delta H\|_{Zhou}$	28.87	31.60	30.11	35.28	-
$\|\Delta H\|_{van't-Hoff}$	28.35	31.69	28.23	31.28	-
$\|\Delta H\|_{Feng}$	30.81	34.01	28.69	28.97	-
$\|\Delta H\|$	32.30	31.83	-	-	[53, 54]
$\|\Delta H\|$	-	$\approx$ 31.80	-	-	[55]
$\|\Delta H\|$	31.79	-	-	-	[41]
$\|\Delta H\|$	$\approx$ 33	-	-	-	[56]
$\|\Delta H\|$	30.9	-	27.7	-	[57]

Table 2.6: Absolute enthalpy of hydrogen ab/desorption for $LaNi_5Co_5$ and $LaNi_{4.5}Co_{0.5}$ metal alloy calculated from models evaluated in this work and from literature.

Entropy $[J\,(K\,mol\,H_2)^{-1}]$	$LaNi_5$ Absorption	$LaNi_5$ Desorption	$LaNi_{4.5}Co_{0.5}$ Absorption	$LaNi_{4.5}Co_{0.5}$ Desorption	Ref.
$\|\Delta S\|_{Zhou}$	107.49	112.38	146.28	160.29	-
$\|\Delta S\|_{van't-Hoff}$	144.56	151.12	141.15	148.70	-
$\|\Delta S\|$	-	108.78	-	-	[55]
$\|\Delta S\|$	-	$\approx$ 100	-	-	[28, 58]

Table 2.7: Absolute entropy of hydrogen ab/desorption for $LaNi_5Co_5$ and $LaNi_{4.5}Co_{0.5}$ metal alloy calculated from models evaluated in this work and from literature.

In general, we can see that the absolute enthalpies of all processes, i.e. ab- and desorption, are similar for both metal alloys; it fluctuates around $30\,kJ(mol\,H_2)^{-1}$. In detail, the absolute absorption enthalpies calculated in our work are around $28..30\,kJ(mol\,H_2)^{-1}$. This is in good agreement to the values of $31..33\,kJ\,(mol\,H_2)^{-1}$ which can be found in literature. The absolute desorption enthalpies determined in this work are higher than the absorption enthalpies. This difference between absorption and desorption enthalpy can be attributed to the hysteresis which is experimentally observed for both metal alloys. In addition, Koh *et al.* [59] studied the kinetics of $LaNi_5$ for de/hydrogenation. They found the activation energy of absorption and desorption to be 27 and 37 $kJ\ mol^{-1}$, respectively. This implies that the absorption enthalpy of $LaNi_5$ should be smaller than that of desorption; as mentioned in the works given in [60, 61]. This is in agreement with the findings obtained in this study as well.

When we inspect the absolute absorption enthalpies for $LaNi_{4.5}Co_{0.5}$, we find a larger fluctuation of the values, i.e. $28..35\,kJ\,(mol\,H_2)^{-1}$, compared to the other alloy. The values determined using the Zhou, van't Hoff, and Feng models are in good agrement with the values that we found in the literature. A wider range of the desorption enthalpies in $LaNi_{4.5}Co_{0.5}$ is found as well. These enthalpies are also principally higher than the absorption enthalpies. We are not able find respective literature values for the desorption enthalpy.

In terms of entropy, we observe for both alloys that the absolute entropy change $|\Delta S|$ of desorption is always higher than the corresponding absorption one; whereas the differences are relatively small. Essentially, all values are in a range of $140..160\,J\,(K\,mol\,H_2)^{-1}$ but the values resulting from Zhou model for the $LaNi_5$ alloy; these are around $110\,J\,(K\,mol\,H_2)^{-1}$. The latter values have a good agreement with the values reported by Mal *et al.* for $LaNi_5$, i.e. $108.78\,J\,(K\,mol\,H_2)^{-1}$ [55]. In addition, an entropy change value of about $100\,J\,(K\,mol\,H_2)^{-1}$ is reported by Uchida *et al.* [28].

2.6 Concluding Remarks

The characterization of hydrogen storage grade $LaNi_5$ and $LaNi_{4.5}Co_{0.5}$ metal alloys in terms of hydrogen absorption and desorption is performed by employing a gravimetric analysis technique. The applicability of selected literature models, along with a novel model based on a cumulative distribution function, with respect to a reproduction of experimental data is investigated. The concluding remarks are, as follows:

1) It is observed that the thermodynamic-based Zhou model does not reflect a smooth transition of the isotherms between different phases. The model describes the α- , β-, and $\alpha + \beta$-phase regions adequately for engineering applications. In addition, the model is capable of displaying experimental data in case of non-idealities of the plateau region. This includes plateaus with slopes and slightly curved transition regions. The advantage of the Zhou model is that it is derived from thermodynamics; hence, the regression coefficients mainly have a physicochemical meaning.

2) Displaying various P-C isotherms in a single characteristic curve of collapsed (scaled) experimental data can be used to find simple models which feature less parameters. The empirical model proposed by Bjurström and co-workers utilizes an arbitrary mid-plateau reference pressure to describe the experimental data in a single characteristic curve. In our study, we expand this approach and introduce a temperature-dependent reference pressure. The Bjurström model gives very good accuracy especially in the α- and transition phases. The ERF model shows good accuracy for α- and transition phases as well. Due to the nature of the error function, i.e. the sole description of the transition between two constant values, less accuracy

is obtained for β-phases. Nevertheless, this should be still acceptable for engineering applications. Contrary to the Zhou model, the Bjurström and the ERF model can reproduce a smooth transition between phases. An advantage of the ERF model is that it requires fewer regression parameters compared to the Bjurström model. However, the regression coefficients of both empirical models have no physicochemical relevance.

3) The Feng model describes the phase transition points and non-ideal characteristics of the $\alpha + \beta$-phase, i.e. a non-ideal plateau region, reasonably well. Contrary to the Zhou model, the Feng model can cover a smooth transition between phases. Beside these rather mathematical characteristics, we have to deviate from the original procedure to obtain model parameters of physicochemical relevance. This might be related to the different type of metal alloy used in our work compared to the original work.

4) Finally, the enthalpy and entropy values of hydrogenation and dehydrogenation of the $LaNi_5$ metal alloy which are computed through the Zhou and Feng models are in good agreement with the literature data. However, the entropy values of hydrogen sorption of $LaNi_5$ and $LaNi_{4.5}Co_{0.5}$ metal alloys that are obtained by using the van't Hoff model are somewhat higher than the value of approximately 130 $J\,(K\,mol\,H_2)^{-1}$ as reported for the entropy change for all metal-hydrogen systems [62]. Additionally, the entropy values of $LaNi_{4.5}Co_{0.5}$, obtained by using the Zhou model, are about 18% (by average) higher than the approximate value mentioned above.

2.7 Acknowledgments

The authors gratefully acknowledge the financial support from the Natural Sciences and Engineering Research Council of Canada (NSERC). The authors would like to thank Dr. Mike B. Evans, Professor Emeritus at the Royal Military College of Canada for his useful advice and support throughout this project.

2.8 Nomenclature

A	Coefficient/regression parameter [-]
a_i	Regression parameters in [-] except for $i = 3, 6$ $[L\, atm\, mol^{-1}]$
C	Metal hydride concentration [-]
f_s	Slope factor [-]
H_s (ΔH_s)	Heat of solution of hydrogen $[J\, mol^{-1}]$
H (ΔH)	Enthalpy $[kJ\, (mol\, H_2)^{-1}]$
k	Variation rate of slope factor $[K^{-1}]$
k^0	Reaction rate constant $[sec^{-1}]$
mid	Mid-point
P	Pressure [bar]
R	Universal gas constant $[L\ atm\ K^{-1}\ mol^{-1}\ ]$
S	Entropy $[J\, (K\, mol\, H_2)^{-1}]$
T	Absolute temperature $[K]$
V	Partial molar volume $[L\ \ mol^{-1}]$
$y_0 - x_0$	Regression parameter
α	Single phase (dehydrided)/anhydrated phase
$\alpha + \beta$	Transition phase when α and β phases coexist
β	Single phase (hydrided)/hydrated phase
γ	Hydrogen activity [-]/unstable phase of nickel with higher oxidation state
γ^H	Absorbed hydrogen-hydrogen attractive interaction $[kJ\, (mol\, H_2)^{-1}]$
Δ	Difference
θ	Filling fraction
μ	Chemical potential $[J\, mol^{-1}]$
Ω_i	Regression parameter [-] except for $i = 3, 4$ $[L\, atm\, mol^{-1}]$

2.9 References

[1] Wang XL and Suda S. Reaction kinetics of hydrogen-metal hydride systems. *Int. J. Hydrogen Energy*, 15(8):569 – 577, 1990.

[2] Feng F, Geng M, and Northwood DO. Electrochemical behaviour of intermetallic-based metal hydrides used in Ni/metal hydride (MH) batteries: A review. *Int. J. Hydrogen Energy*, 26(7):725 – 734, 2001.

[3] Bjurström H, Komazaki Y, and Suda S. The dynamics of hydrogen transfer in a metal hydride heat pump. *J. Less-Common Met.*, 131(1-2):225 – 234, 1987.

[4] Payá J, Linder M, Mertz R, and Corberan JM. Analysis and optimization of a metal hydride cooling system. *Int. J. Hydrogen Energy*, 36(1):920 – 930, 2011.

[5] Schlapbach L and Züttel A. Hydrogen-storage materials for mobile applications. *Nature*, 414(6861):353–358, 2001.

[6] Nahm KS, Kim WY, Hong SP, and Lee WY. The reaction kinetics of hydrogen storage in $LaNi_5$. *Int. J. Hydrogen Energy*, 17(5):333 – 338, 1992.

[7] Sakintuna B, Darkrim FL, and Hirscher M. Metal hydride materials for solid hydrogen storage: A review. *Int. J. Hydrogen Energy*, 32(9):1121 – 1140, 2007.

[8] Rowsell JLC and Yaghi OM. Strategies for hydrogen storage in metal-organic frameworks. *Angew. Chem. Int. Ed.*, 44(30):4670–4679, 2005.

[9] Ovshinsky SR, Fetcenko MA, and Ross J. A nickel metal hydride battery for electric vehicles. *Science*, 260(5105):176–181, 1993.

[10] Furukawa N. Development and commercialization of nickel-metal hydride secondary batteries. *J. Power Sources*, 51(12):45 – 59, 1994.

[11] Lacher JR. A theoretical formula for the solubility of hydrogen in palladium. *Proc. R. Soc. London Ser. A*, 161(907):525–545, 1937.

[12] Evans MJB and Everett DH. Thermodynamics of the solution of hydrogen and deuterium in palladium. *J. Less-Common Met.*, 49(1):123 – 145, 1976.

[13] Lototsky MV, Yartys VA, Marinin VS, and Lototsky NM. Modelling of phase equilibria in metal-hydrogen systems. *J. Alloys Compd.*, 356-357(1):27 – 31, 2003.

[14] Feng F, Geng M, and Northwood DO. Mathematical model for the plateau region of PC-isotherms of hydrogen-absorbing alloys using hydrogen reaction kinetics. *Comput. Mater. Sci.*, 23(14):291 – 299, 2002.

[15] Griessen R. Phase separation in amorphous metal hydrides: A stoner-type criterion. *Phys. Rev. B*, 27:7575–7582, 1983.

[16] Lexcellent CH and Gondor G. Analysis of hydride formation for hydrogen storage: Pressure-composition isotherm curves modeling. *Intermetallics*, 15(7):934 – 944, 2007.

[17] Schwarz RB and Khachaturyan AG. Thermodynamics of open two-phase systems with coherent interfaces: Application to metal-hydrogen systems. *Acta Mater.*, 54(2):313 – 323, 2006.

[18] Beeri O, Cohen D, Gavra Z, Johnson JR, and Mintz MH. High-pressure studies of the $TiCr_{1.8}H_2$ system statistical thermodynamics above the critical temperature. *J. Alloys Compd.*, 267(1-2):113 – 120, 1998.

[19] Samsun BM, Fukada S, and Fujiwara H. Hydrogen isotope absorption amount and rate of $PdAl_2O_3$ pellets. *Int. J. Hydrogen Energy*, 26(3):225–229, 2001.

[20] Rees ALG. Statistical mechanics of two-component interstitial solid solutions. *Trans. Faraday Soc.*, 50:335–342, 1954.

[21] Anderson JS. The conditions of equilibrium of ”non-stoichiometric” chemical compounds. *Proc. R. Soc. London Ser. A*, 185(1000):69–89, 1946.

[22] Kierstead HA. A theory of multiplateau hydrogen absorption isotherms. *J. Less-Common Met.*, 71(2):303 – 309, 1980.

[23] Kierstead HA. A theory of hydrogen absorption with interactions. *J. Less-Common Met.*, 96(1):141 – 152, 1984.

[24] Larsen JW and Livesay BR. Hydriding kinetics of $SmCo_5$. *J. Less-Common Met.*, 73(1):79 – 88, 1980.

[25] Hömberg D. A numerical simulation of the jominy end-quench test. *Acta Mater.*, 44(11):4375 – 4385, 1996.

[26] Bjurström H, Suda S, and Lewis D. A numerical expression for the P-C-T properties of metal hydrides. *J. Less-Common Met.*, 130(0):365 – 370, 1987.

[27] Jury SH and Edwards HR. The silica gel-water vapor sorption therm. *Can. J. Chem. Eng.*, 49(5):663 – 666, 1971.

[28] Uchida M, Bjurström H, Suda S, and Matsubara Y. On the equilibrium properties of some $ZrMn_2$-related hydride-forming alloys. *J. Less-Common Met.*, 119(1):63 – 74, 1986.

[29] Stark M, Krost G, Lemken D, and Oberschachtsiek B. Neural network based modeling of metal-hydride bed storages for small self-sustaining energy supply systems. In *PowerTech, 2011 IEEE Trondheim*, pages 1 – 7, 2011.

[30] Guo J, Li C, Liu H, and Chen N. Effect of rare earth compositions on the hydrogen storage properties of AB_5-type alloys and pattern recognition analysis. *J. Electrochem. Soc.*, 144(7):2276–2278, 1997.

[31] Jemni A, Nasrallah SB, and Lamloumi J. Experimental and theoretical study of a metal-hydrogen reactor. *Int. J. Hydrogen Energy*, 24(7):631 – 644, 1999.

[32] Askri F, Jemni A, and Nasrallah SB. Prediction of transient heat and mass transfer in a closed metal-hydrogen reactor. *Int. J. Hydrogen Energy*, 29(2):195 – 208, 2004.

[33] Askri F, Jemni A, and Nasrallah SB. Dynamic behavior of metal-hydrogen reactor during hydriding process. *Int. J. Hydrogen Energy*, 29(6):635 – 647, 2004.

[34] Askri F, Jemni A, and Nasrallah SB. Study of two-dimensional and dynamic heat and mass transfer in a metal-hydrogen reactor. *Int. J. Hydrogen Energy*, 28(5):537 – 557, 2003.

[35] Askri F, Salah MB, Jemni A, and Nasrallah SB. Optimization of hydrogen storage in metal-hydride tanks. *Int. J. Hydrogen Energy*, 34(2):897 – 905, 2009.

[36] Gambini M, Manno M, and Vellini M. Numerical analysis and performance assessment of metal hydride-based hydrogen storage systems. *Int. J. Hydrogen Energy*, 33(21):6178 – 6187, 2008.

[37] Fujitani S, Nakamura H, Furukawa A, Nasako K, Satoh K, Imoto T, Saito T, and Yonezu I. A method for numerical expressions of P-C isotherms of hydrogen-absorbing alloys. *Z. Phys. Chem.*, 179(1-2):27 – 33, 1993.

[38] Nakamura Y, Nakamura H, Fujitani S, and Yonezu I. Homogenizing behaviour in a hydrogen-absorbing $LaNi_{4.55}Al_{0.45}$ alloy through annealing and rapid quenching. *J. Alloys Compd.*, 210(1-2):299 – 303, 1994.

[39] Zhou Z, Zhang J, Ge J, Feng F, and Dai Z. Mathematical modeling of the PCT curve of hydrogen storage alloys. *Int. J. Hydrogen Energy*, 19(3):269 – 273, 1994.

[40] Payá J, Linder M, Laurien E, and Corberan JM. Mathematical models for the P-C-T characterization of hydrogen absorbing alloys. *J. Alloys Compd.*, 484(12):190 – 195, 2009.

[41] Boser O. Hydrogen sorption in $LaNi_5$. *J. Less-Common Met.*, 46(1):91 – 99, 1976.

[42] Miyamoto M, Yamaji K, and Nakata Y. Reaction kinetics of $LaNi_5$. *J. Less-Common Met.*, 89(1):111 – 116, 1983.

[43] Tanaka S, Clewley JD, and Flanagan TB. Kinetics of hydrogen absorption by $LaNi_5$. *J. Phys. Chem.*, 81(17):1684–1688, 1977.

[44] Wallace WE, Karlicek RF, and Imamura H. Mechanism of hydrogen absorption by $LaNi_5$. *J. Phys. Chem.*, 83(13):1708–1712, 1979.

[45] Oh JW, Kim CY, Nahm KS, and Sim KS. The hydriding kinetics of $LaNi_{4.5}Al_{0.5}$ with hydrogen. *J. Alloys Compd.*, 278(12):270 – 276, 1998.

[46] Park CN and Lee JY. A study on the kinetics of hydriding of the LaNi5 system. *J. Less-Common Met.*, 83(1):39 – 48, 1982.

[47] Payá J, Freni A, Corberán JM, and Compahan V. Hydriding kinetics of $LaNi_5$ using nucleation-growth and diffusion models. *J. New Mater. Electrochem. Syst.*, 15:293 – 300, 2012.

[48] Feng F, Ping X, Zhou Z, Geng M, Han J, and Northwood DO. The relationship between equilibrium potential during discharge and hydrogen concentration in a metal hydride electrode. *Int. J. Hydrogen Energy*, 23(7):599 – 602, 1998.

[49] Adachi G, Sakaguchi H, Niki K, Nagai N, and Shimokawa J. Preparation of $LaNi_5$ films and their electrical properties under a hydrogen atmosphere. *J. Less-Common Met.*, 108(1):107 – 114, 1985.

[50] Fang S, Zhou Z, Zhang J, Yao M, Feng F, and Northwood DO. Two mathematical models for the hydrogen storage properties of AB_2 type alloys. *J. Alloys Compd.*, 293-295(1):10 – 13, 1999.

[51] Murillo R, Garciá T, Aylón E, Callén MS, Navarro MV, López JM, and Mastral AM. Adsorption of phenanthrene on activated carbons: Breakthrough curve modeling. *Carbon*, 42(10):2009 – 2017, 2004.

[52] Wiedemann K, Roethe A, and Radeke K-Gelbin D. The modelling of adsorption-desorption breakthrough curves using statistical moments. *Chem. Eng. J.*, 16(1):19 – 26, 1978.

[53] Han JI and Lee JY. An investigation of the intrinsic degradation mechanism of $LaNi_5$ by thermal desorption technique. *Int. J. Hydrogen Energy*, 13(9):577 – 581, 1988.

[54] Murray JJ, Post ML, and Taylor JB. The thermodynamics of the $LaNi_5 - H_2$ system by differential heat flow calorimetry I: Techniques; the $\alpha + \beta$ two-phase region. *J. Less-Common Met.*, 80(2):201 – 209, 1981.

[55] Van Mal HH, Buschow KHJ, and Miedema AR. Hydrogen absorption in LaNi5 and related compounds: Experimental observations and their explanation. *J. Less-Common Met.*, 35(1):65 – 76, 1974.

[56] Andreasen A. Predicting formation enthalpies of metal hydrides. Technical report, Risø National Laboratory, Roskilde, Denmark, 2004. ISBN 87-550-3382-2.

[57] Miyashita T and Masuda Y. Study on the interaction between hydrogen and metals of $LaNi_5$ type hydrogen absorbing alloys by means of DV-Xα method. *J. Alloys Compd.*, 475(1-2):422 – 428, 2009.

[58] Pedziwiatr AT, Craig RS, Wallace WE, and Pourarian F. Calorimetric enthalpies of formation and decomposition of hydrides of $ZrMn_2$, $ZrCr_2$, and related systems. *J. Solid State Chem.*, 46(3):336 – 341, 1983.

[59] Koh JT, Goudy AJ, Huang P, and Zhou G. A comparison of the hydriding and dehydriding kinetics of $LaNi_5$ hydride. *J. Less-Common Met.*, 153(1):89 – 100, 1989.

[60] Flanagan TB and Clewley JD. Hysteresis in metal hydrides. *J. Less-Common Met.*, 83(1):127 – 141, 1982.

[61] Sinha VK and Wallace WE. The hyperstoichiometric $ZrMn_1 + xFe_1 + yH_2$ system II: Hysteresis effect. *J. Less-Common Met.*, 91(2):239 – 249, 1983.

[62] Züttel A. Materials for hydrogen storage. *Mater. Today*, 6(9):24 – 33, 2003.

Chapter 3

Fabrication and Characterization of Thin Film Nickel Hydroxide Electrodes for Micro-Power Applications[1]

3.1 Abstract

The utilization of micro-power sources is attractive in portable microfluidic devices where only low power densities and energy contents are required. In this work, we report on the micro-fabrication of patterned α-$Ni(OH)_2$ films on glass substrates which can be used for rechargeable micro batteries as well as for micro-capacitors.

---

[1] H. Falahati, E. Kim and D.P.J. Barz (2015); This paper has been published in ACS Applied Materials & Interfaces, Vol. 7, Issue 23, Pages 12797-12808.

A multi-layer deposition technique is developed based on e–beam evaporation, ultraviolet photolithography and electroplating/electrodeposition which creates thin-film electrodes that are patterned with arrays of micro-pillars. The morphology and the structure of the patterned electrode films are characterized by employing field emission scanning electron microscopy. The chemical composition is investigated by using X-ray diffraction and X-ray photoelectron spectroscopy. Finally, cyclic voltammetry, electrochemical impedance spectroscopy and galvanostatic charge/discharge measurements are used to evaluate the electrochemical performance of the patterned thin film electrodes compared to patternless electrodes. We observe that patterning of the electrodes results in significantly improved stability and, thus, longer endurance while good electrochemical performance is maintained.

3.2 Introduction

In the last two decades, micro-electro-mechanical-systems (MEMS) and especially microfluidic systems have attracted considerable attention since they offer size reduction along with the possibility of integration of several functions in a single unit. The system capabilities usually far exceed those of conventional systems while maintaining the potential of being mass produced at a low cost [1]. Technological microfluidic concepts comprise, for example, Lab-on-a-Chip [2] and Point-of-Care-Testing [3] systems where the typical utilization aims at chemical analytics and medical diagnostics, respectively. However, in almost all microfluidics as well as in other MEMS technologies, the supply of electric power is a barrier to further development since battery miniaturization has not kept the same pace as the advances in micro-fabrication methods. That is, the size of a micro-device is often determined by the size of its power supply, and integrating a (macroscopic) power supply within the device structure is often not possible [4]. Typical sub-millimeter sized sources should produce power in the range of 10^2 to $10^3 \mu W\, cm^{-2}$ and should have capacities of up to $10^3 \mu Ah\, cm^{-2}$, at an operating voltage range of 2 to $3V$ [5]. Sub-millimeter power sources with such power and energy densities have not yet been developed due to constraints on packaging, fuel storage, fuel delivery, and power generation [6].

Presently, there are several strategies for the miniaturization of electrical power sources. These include regenerative power technologies that generate power from micro-photovoltaic arrays or thermoelectric, electrostatic and piezoelectric devices [7, 8]. In contrast, non-regenerative power supplies have a finite amount, or require a continuous supply, of active materials/fuel for power generation, such as micro-fuel cells [9] and microfluidic fuel cells [10]. Other relevant electrochemical devices are micro-batteries where the chemistries are in most cases indistinguishable from conventional batteries. Though configurations, material deposition, post-processing and packaging methods applicable to macro batteries are oftentimes not feasible below the centimeter scale. Hence, the resulting micro-battery performance does not proportionally scale at such miniature dimensions [11]. Micro-batteries typically utilize thin or thick films of electroactive materials which can be either printed or deposited by various techniques such as sol-gel, electrodeposition, physical and chemical vapor deposition or atomic layer deposition [12].

Here, micro-power sources which utilize nickel hydroxide ($Ni(OH)_2$) films appear promising since they offer well-defined reduction-oxidation (redox) activity, high power/energy density as well as good cyclability at low cost. However, the discharge rate and the temperature sensitivity still need to be improved [13, 14]. Nevertheless, considerable scientific and technological knowledge of $Ni(OH)_2$ substrates is available since they have been widely investigated for their utilization in macroscopic batteries, such as nickel/cadmium (Ni/Cd) ($E^{0\Theta} = 1.3\,V$), nickel/metal hydride (Ni/MH) ($E^{0\Theta} = 1.3\,V$) or nickel/zinc (Ni/Zn) ($E^{0\Theta} \approx 1.7\,V$) [15] as well as in electrochromic devices [16, 17]. The standard half cell potential of $Ni(OH)_2/NiOOH$ is around $0.5\,V$ (vs. SHE).

The current research on $Ni(OH)_2$ films often aims at (pseudo) electrochemical capacitors including, but not limited to, the work of [18, 19, 20, 21]. For this application, research is also dedicated to the preparation of nano-sized particulate $Ni(OH)_2$ which is deposited on carbon-nano-tubes [22, 23], on nickel foams [24] or clustered to microspheres [25]. Other applications of $Ni(OH)_2$ films aim to increase the electrocatalytic activity and stability of sensors [26].

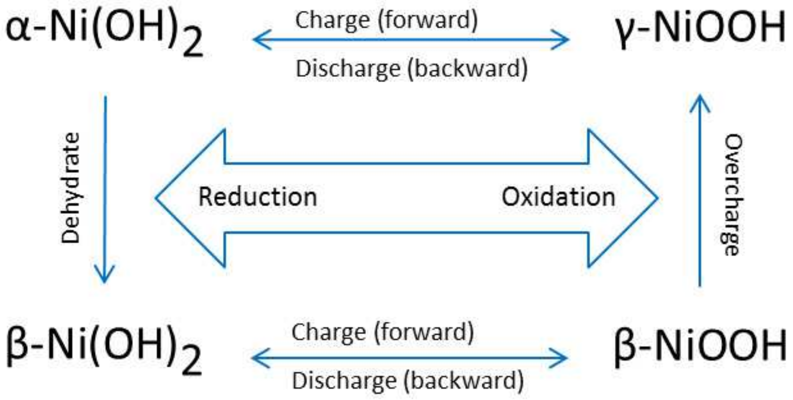

Figure 3.1: Four phase Bode scheme of oxidation and reduction of $Ni(OH)_2/NiOOH$ according to [27] as cited in [28].

The suitability of $Ni(OH)_2$ substrates for electrochemical applications is due to the fact that they can be reversibly converted to nickel oxyhydroxide ($NiOOH$) as sketched in Figure 3.1. Generally, $Ni(OH)_2$ has two polymorphic states. The hydrated form with intercalated water molecules is called α-$Ni(OH)_2$. In a highly-concentrated alkaline solution, this structure is unstable and converts to the relatively anhydrous and thermodynamically stable polymorph β-$Ni(OH)_2$. The β-$Ni(OH)_2$ can then be charged to increase the oxidation state of Ni to about 3 which is called β-$NiOOH$. If it is further charged (overcharged), the β-$NiOOH$ is converted to another polymorph, the so-called γ-$NiOOH$. There are several difficulties involved with the redox reaction between the β-phases, including volume expansion which results in mechanical instability problems and a generally lower charge capacity [29]. Here, an alternative redox route is favourable where α-$Ni(OH)_2$ is directly oxidized to γ-$NiOOH$ which can also occur at a lower potential than that required for the redox reaction between the two β-phases [27]. Another advantage of this route is that α-$Ni(OH)_2$ features a considerably lower mass density so that higher mass specific charge contents can be achieved. Hence, there is significant research dedicated to the stability enhancement of α-phase in alkaline milieus such as refs. [29, 30].

So far, very few attempts have been made to utilize $Ni(OH)_2$ film electrodes for micro-battery applications. Humble et al. fabricated a Ni/Zn micro-battery on a epoxy-coated silicone chip where the cathode consisted of a roughly $100\mu m$ thick film deposited on a nickel current collector of around $600nm$ in thickness. An estimation of the film electrodes characteristics resulted in an energy and power density of around $0.5mWh\,cm^{-2}$ and $50mW\,cm^{-2}$, respectively [31, 32]. Further research by Do et al. was concerned with the screen printing of $Ni(OH)_2$ thick-film electrodes for Ni/MH batteries on porous ceramic substrates and on polypropylene films [33, 34]. It is questionable whether or not this fabrication method can be easily adapted to micro-systems. Additionally, such printed films have a limited tolerance for stress arising from volume change of the active materials [35] and from shear if in contact with flowing liquids as we may have in microfluidics.

In the present work, we report on a novel fabrication method for thin film electrodes of α-$Ni(OH)_2$ directly on glass, which is one of the most common microfluidic substrates. These electrodes can be employed for micro-power applications such as rechargeable micro-batteries or electrochemical capacitors. In contrast to the work of others, which is concerned with the electrodeposition of $Ni(OH)_2$ thin films on bulk nickel foils, such as [21, 36], we use lithography techniques to create patterned films on the glass substrate. These micro-fabricated electrodes are characterized in terms of their material compositions and surface morphologies. We investigate the electrochemical performance of the patterned electrodes and compare them to similar but patternless film electrodes. This article continues with a section on the experimental methodologies and materials followed by a discussion of our experimental results. Finally, the article is summarized with some concluding remarks.

3.3 Experimental Methods and Materials

In this section, we specify the materials, fabrication and characterization techniques which are used for this work.

3.3.1 Microfabrication

Materials: Glass microscope slides (Fisher Scientific, Canada) of area 1 by 3 inches are used as the microfluidic substrate for the micro-fabrication of the $Ni(OH)_2$ films. Nickel and chromium pellets (Kurt J. Lesker Canada, Inc., Canada) with purities

99.995% and 99.998%, respectively, are used for the physical vapour deposition of the thin films. Electrodeposition is performed using nickel(II) chloride hexahydrate (puriss. p.a., $> 98\%$, Sigma-Aldrich Canada Co., Canada) and nickel(II) nitrate hexahydrate (99.999% trace metals basis, Sigma-Aldrich Canada Co., Canada). Note that the use of a very high purity nickel nitrate solution is required since traces of co-precipitated metals such as iron can promote unwanted side reactions such as the oxygen evolution reaction (OER) [37]. For the sake of comparison, nickel films are also prepared on nickel foil (99.99%, Sigma-Aldrich Canada Co., Canada) with a thickness of $0.125\,mm$. The materials required for the ultraviolet (UV) lithography include a chemically amplified negative photoresist KMPR® 1000, a SU-8 photoresist developer solution (Methoxy-2-propanol acetate) and a photoresist remover PG solution (1-Methylpyrrolidone (NMP)) (all from MicroChem Corp., USA).

Instruments: Metal thin films are prepared using an electron beam evaporator (Thermionics laboratory Inc., USA) coupled with an IG4500 ion gauge controller. The deposition rate is controlled by a deposition crystal monitor (INFICON Inc., USA). In terms of the UV lithography process, we use a glass photo-mask, with a grid style geometric pattern consisting of squares of size $400 \times 400\,\mu m^2$, obtained from nanoFAB at the University of Alberta (Canada). The other photo-masks which are required for the patterning of the nickel current collector are made by printing on a regular office transparency sheet by using a XEROX office printer (XEROX WorkCentre 7428). A mask aligner (Oriel Instruments, USA) coupled with a light intensity controller, timer, and ultraviolet (UV) lamp is used to transfer the mask pattern to the photoresist. In terms of electrodeposition, a power supply (U8002A, Agilent Technologies, USA) along with a potentiostat/galvanostat (PGSTAT302N, Metrohm Autolab B.V., The Netherlands) are utilized.

3.3.2 Materials and Physical Characterization

The elemental composition of the deposited films is examined with an X-ray diffraction (XRD) instrument (X'Pert Pro, Philips Analytical B.V., The Netherlands) via Cu K-alpha radiation. The diffractometer is operated at 40 kV and 45 mA. The data analysis is performed by using X'Pert Highscore Pro software. Additionally, we employ an X-ray photoelectron spectrometer (XPS) (Thermo Instruments 310-F Microlab) using the Mg Kα method. A stylus profiler (Dektak XT, Bruker Nano Surfaces Division, USA) is used to characterize the size features of the electrode surfaces. Furthermore, an infrared analysis is performed by using a Nicolet Avatar 320 Fourier transform infrared (FTIR) spectrometer (Thermo Electron Corporation, USA) with a Specac Golden Gate single pass diamond attenuated total reflectance (ATR) accessory. A total number of 32 scans is collected at a resolution of $4\,cm^{-1}$.

3.3.3 Electrochemical Characterization

Electrode films are electrochemically characterized with cyclic voltammetry (CV), Electrochemical Impedance Spectroscopy and galvanostatic charge/discharge measurements using a potentiostat/galvanostat (PGSTAT302N, Metrohm Autolab B.V., The Netherlands). A three electrode setup is utilized consisting of the working electrode ($Ni(OH)_2$), reference electrode (Ag/AgCl/3M KCl, double junction, Metrohm Autolab B.V., The Netherlands) and a counter electrode (Pt-wire-mesh, Metrohm Autolab B.V., The Netherlands). All electrochemical measurements are performed in aqueous $1\,M$ potassium hydroxide (KOH) solutions at a room temperature of $23°C$.

The electrolyte solutions are prepared with deionized water having a conductivity of approximately $2\,\mu S\,cm^{-1}$. Conductivities and pH values are tested using a modular pH and conductivity meter (Mettler-Toledo, SevenMulti, Switzerland). Additionally, a source measure unit instrument (2400-LV SourceMeter, Keithley Instruments Inc., USA) coupled with a 4-probe station with Tungsten W probe-tips (Wentworth Laboratories Inc., USA) is used to measure the surface resistance of the thin films.

3.4 Results and Discussion

In this section, we first describe the micro-fabrication of the patterned film electrodes on glass substrates. These micro-fabricated electrodes are compared to similar patternless films which are deposited on commercially available nickel sheets.

3.4.1 Microfabrication

The $Ni(OH)_2$ thin film electrodes are made through micro-fabrication techniques which are commonly used in the semiconductor industry along with electroplating and electrodeposition. The process starts with the fabrication of a current collector on the microfluidic substrate using electron beam physical vapor deposition (e-beam evaporation). We first perform some qualitative experiments with a sticky tape to test the adherence of the deposited thin films on glass. It turns out that pure nickel hardly adheres to glass. An improved adherence is achieved, when we first evaporate chromium to deposit an adhesion (seed) layer of a thickness of $40\,nm$ on the glass surface. Then, a nickel film of the same thickness is grown onto the adhesion layer. In terms of patternless electrodes, $Ni(OH)_2$ films are electrodeposited onto the current collector from the nickel nitrate solution in a potentiostatic mode. We observe that the durability of these $Ni(OH)_2$ films is very poor. Fu et al. used nickel sheet foils as the substrate for the electrodeposition of $Ni(OH)_2$ films [21]. They mentioned that the nickel foils were polished with emery paper to a rough finish. We use the same method for our electrode preparation on nickel foils since this enhances the adhesion with the film material, as we discuss in the next section. In our case, the very small thickness of the e–beam evaporative deposited current collectors prevents this kind of mechanical surface roughening. Therefore, we employ a novel approach which appears more suitable for micro-fabricated thin films. That is, we pattern the nickel current collector with a 3D array of micro-pillars. These 3D features not only "simulated roughness" of the surface, but also increase the size of the adhesion area.

The patterned electrode is fabricated through a multi-layered film process which, along with e–beam evaporation and electroplating/electrodeposition, also employs multiple UV photolithography steps. The process steps are illustrated in Figure 3.2. In detail, the microscope glass slide is first subjected to a cleaning process involving acetone, isopropanol and DI water. A layer of KMPR® photoresist is spin-coated on the glass slide in two steps ($500\,rpm$ with an acceleration of $100\,rpm\,s^{-1}$, followed by $3000\,rpm$ with an acceleration of $300\,rpms^{-1}$). The slide with the photoresist is transferred to a hot plate and backed for $25\,mins$ at a temperature of $100°C$. To define the footprint of the electrode on the slide, the photoresist is exposed to UV light through the transparency sheet mask which initiates the cross-linking process. The exposure time is $6\,sec$ and the intensity controller reads 18.8 at a power of $1000\,W$. The glass slide is then transferred to the hot plate for a post exposure bake of $5\,mins$ at a temperature of $100°C$. The photoresist is developed in a SU-8 developer solution for about $5\,mins$ to remove the unexposed areas. That is, the unexposed bare glass surface area defines the location for the deposition of the electrode pad. The glass slide is transferred to the e-beam evaporation chamber where the chromium adhesion layer and subsequently the nickel current collector layer are grown; each film thickness is $40\,nm$. After deposition, the slide with the deposited metal layers is soaked in remover PG solution at a temperature of $60°C$ to strip off the leftover photoresist. Note that soaking times of more than 20 minutes attack the nickel current collector severely, especially at elevated temperatures.

In order to create a patterned nickel surface, we process another layer of photoresist with the same fabrication parameters as described above. However, we use the photo–mask which patterns the photoresist with a grid of squares of size $400 \times 400 \mu m^2$. That is, we obtain a grid–like structure of alternating bare nickel and photoresist-coated squares after the lithography process. The micro-fabrication proceeds with the electroplating of nickel from a $1M\ \ NiCl_2$ solution for around $30\,mins$ at a potential of $0.9\,V$; the resulting current is $\approx I = 0.01\,A$. Since nickel is only deposited at the bare nickel surfaces of the current collector, a three-dimensional pattern of nickel micro-pillars is grown.

Once the three-dimensional features are fabricated, the remaining photoresist is stripped off the electrode pad using the same conditions as previously described. Finally, we grow a thin layer of $Ni(OH)_2$ from an aqueous $Ni(NO_3)_2 \cdot 6H_2O$ solution onto the entire electrode pad. According to ref. [38], this electrodeposition process is based on the reduction of nitrate to ammonium via

$$NO_3^- + 7H_2O + 8e^- \to NH_4^+ + 10OH^-. \tag{3.1}$$

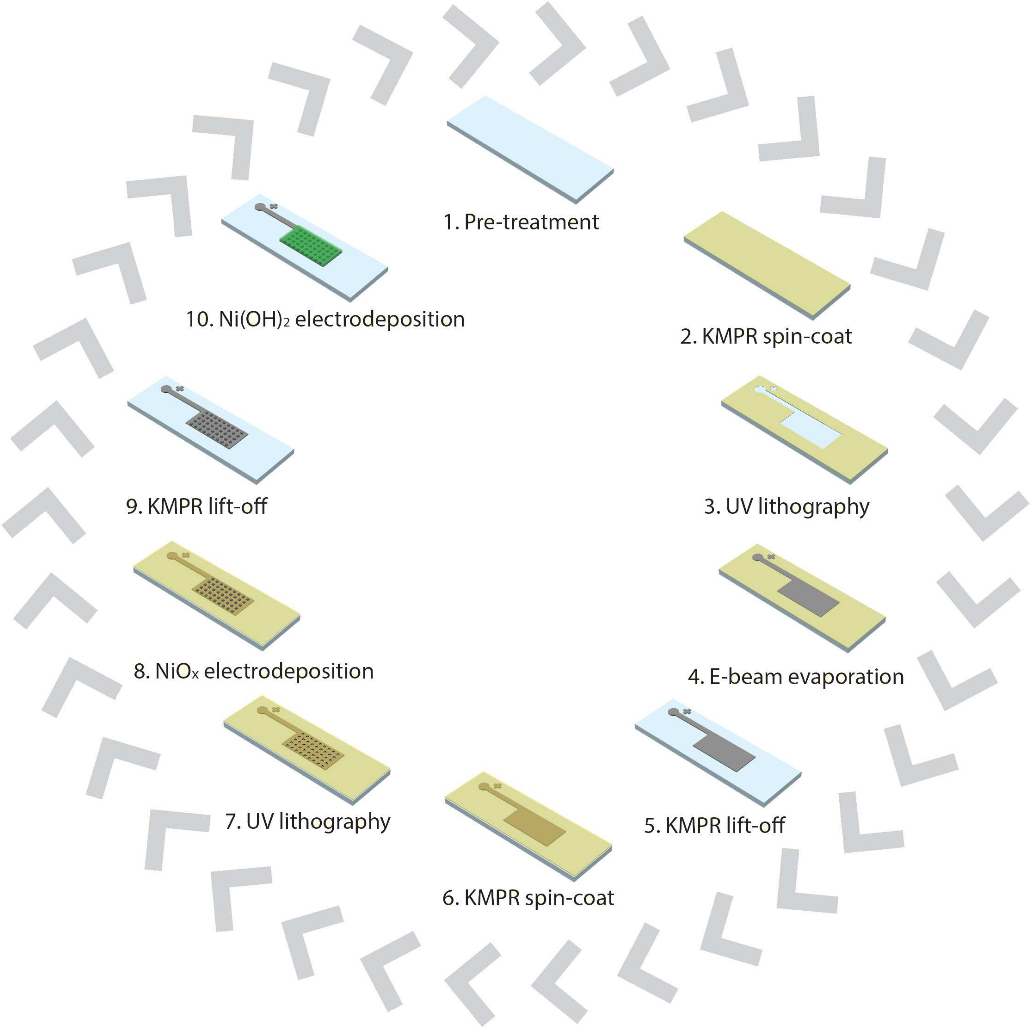

Figure 3.2: Fabrication process scheme of the patterned nickel hydroxide electrode.

The simultaneous generation of hydroxide raises the pH value at the cathode surface locally and the dissolved nickel ions react with the hydroxides and form insoluble nickel(II) hydroxides at the electrode surface according to

$$Ni^{2+} + 2OH^{-} \rightarrow Ni(OH)_2. \tag{3.2}$$

The electrodeposition is performed at a constant potential of $-0.9\,V$ vs. Ag/AgCl for 30 minutes; the observed current density is around 3.25 $mA\,cm^{-2}$.

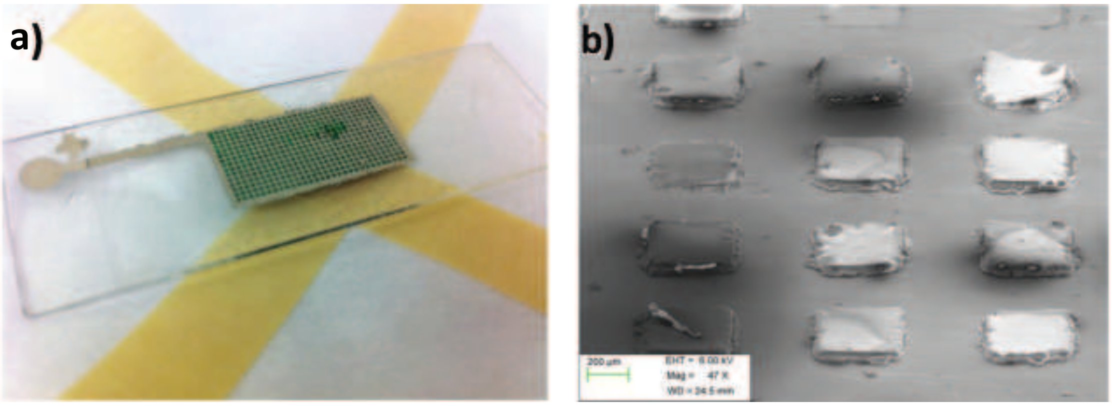

Figure 3.3: a) Picture of the electrode current collector after electroplating of Nickel which results in the three-dimensional grid-like pattern (the second photoresist layer is still present) ; b) FESEM image of the electroplated nickel surface with a detailed view of the 3D features.

Figure 3.3 gives an insight into the structure of the electrode pad after different steps of the micro-fabrication process. In detail, Figure 3.3a) shows a picture of the entire current collector after the electroplating of nickel, prior to stripping off the second photoresist layer and the electrodeposition of $Ni(OH)_2$. We notice the grid-like structure of the current collector which serves as an artificial surface roughness in order to improve the durability of the subsequently deposited $Ni(OH)_2$ film. Figure 3.3b) shows a detailed 60 degree tilt field emission scanning electron microscopy (FESEM) image of the electrode surface; i.e., before the electrodeposition of $Ni(OH)_2$. The micro-pillars have, to good approximation, a footprint of $400 \times 400\,\mu m^2$ and a distance of $400\,\mu m$ between each other. The average height of a micro-pillar is determined to be around $20\,\mu m$ by utilizing a (mechanical) stylus profiler. After the electrodeposition, the micro-pillars are covered by the $Ni(OH)_2$ layer with a thickness of around $35\,\mu m$. We observe that our patterning process significantly improves the stability of the films; the reason behind is unknown. The gain in surface area is roughly 3%. This rather small change makes it less likely to be the cause of the stability improvement. An explanation could be the singularity of the electric field which results from sharp (ideal) geometric discontinuities. That is, there is a significant increase of the electric field strength at the edges and corners of the pillars which may result in a compacted electrodeposited film which improves mechanical strength and adhesion. In the next section, we discuss our results obtained from the materials characterizations and compare them with the relevant literature.

3.4.2 Materials Characterization

As outlined in the section Introduction, the electrochemical performance of $Ni(OH)_2$ is significantly affected by its crystal structure, grain size and morphology. Hence, we employ several characterization methods to obtain insights into the composition, crystalline phase and morphology of the substrates which are fabricated in this work. This detailed insight is especially important since we use multiple complex chemicals and methods for the film fabrications and we are not able to predict their impact on the substrates and the subsequent process steps. We first utilize XPS measurements to investigate the surface composition of the different substrates. We follow Grosvenor et al. [39] in their interpretation on how the oxidation state of nickel at the surface is related to the binding energies and the chemical shifts in the XP spectra. In our study, the carbon offset is taken into account while the satellite peaks are not accounted for. Moreover, only the right-hand side set of peaks are used for the XP spectra interpretations and are fitted to the $Ni(2p)$ multiplet.

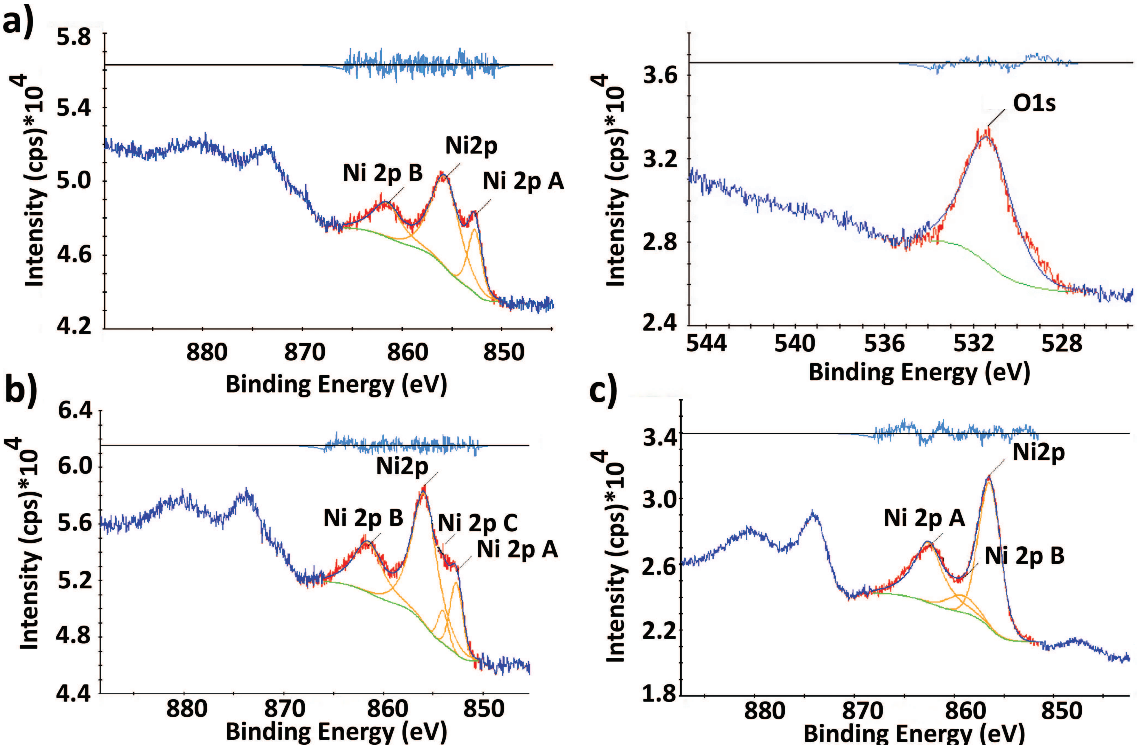

Figure 3.4: $Ni(2p)$ spectrum from a) a commercially available nickel sheet; b) the e-beam evaporated nickel current collector; and c) the electrodeposited nickel hydroxide film.

In detail, Figure 3.4a) shows the spectrum of the commercially available nickel sheet. This substrate is used to prepare a conventionally fabricated (patternless) $Ni(OH)_2$ electrode and is used as a benchmark for the micro-fabricated electrode. We observe two peaks at binding energies of 852.60 and 855.75 eV in the $Ni(2p_{3/2})$ spectrum which correspond to Ni^0 and Ni^{2+}, respectively; the latter can be associated with the nickel in NiO [39]. Additionally, the right-hand side of Figure 3.4a) shows another peak that is measured at 531.45 eV. This single $O(1s)$ peak can reflect both OH^- and O^- or a Ni_2O_3 defect structure [40]. In comparison, Figure 3.4b) shows the $Ni(2p)$ multiplet peaks measured on the nickel film which is grown on glass using e-beam evaporation. The observed binding energies are 852.75 and 855.85 eV and, hence, are almost identical to those observed for the nickel sheet. However, the peak associated with Ni^0 is considerably less pronounced. Additionally, we measure an almost identical $O(1s)$ peak (not shown) as for the nickel sheet. Generally, these results are in agreement with ref. [39] and indicate that both substrates, nickel sheet and e-beam evaporated nickel film, have similar surfaces which consists of elemental nickel and nickel oxide. Considering the ratios of the $Ni(2p_{3/2})$ peaks, it appears that the e-beam evaporated film has a higher fraction of nickel oxide compared to the nickel sheet. Figure 3.4c) shows the $Ni(2p)$ spectrum of the $Ni(OH)_2$ film which is electrodeposited on the patterned current collector surface. We observe distinct peaks at 856.50 eV for $Ni(2p_{3/2})$ and 531.45 eV for $O(1s)$ (not shown) which is similar to the nickel (and nickel oxide) surfaces discussed above. However, Kim and Winograd noted that this combination can also be assigned to $Ni(OH)_2$ since this spectrum is similar to that of Ni_2O_3 and NiO, except that the $O(1s)$ peak is broader [41]. Finally, our XPS measurements confirm that, despite the multiple process steps and the usage of complex chemicals, the fabricated films consist of Ni^0 and Ni^{2+} bonded to an oxide or hydroxide compound, respectively.

Further information on the crystal phase and structure of the $Ni(OH)_2$ films are obtained by utilizing X-ray diffraction (XRD) technique. Here, we peel an electrodeposited film from a micro-fabricated electrode since powder-like samples are required. Figure 3.5 shows the measured XRD pattern which can be indexed according to JCPDS No.38-0715 to the diffraction data of $Ni(OH)_2 \cdot 0.75H_2O$, i.e. to (hydrated) α-$Ni(OH)_2$. Similar patterns are observed in the work of others such as ref. [21]

who attributed the broadening of some of the diffraction peaks to small grain sizes or structural micro-distortions in the crystal structure.

Finally, we perform FTIR ATR spectroscopy of the electrodeposited $Ni(OH)_2$ films. The result gives a band which corresponds to a wave number of around 630 cm^{-1} (not shown). This can be attributed to the lattice vibration of hydroxyl groups (δNi-O-H) which is a typical feature of an α-$Ni(OH)_2$ structure [42, 21]. Note that we are not able to obtain bands below 500 cm^{-1} by using our FTIR-ATR instrument. Therefore, the peaks which can be attributed to Ni-O stretching vibrations, as mentioned in [42, 21], can not be found by using our instrument.

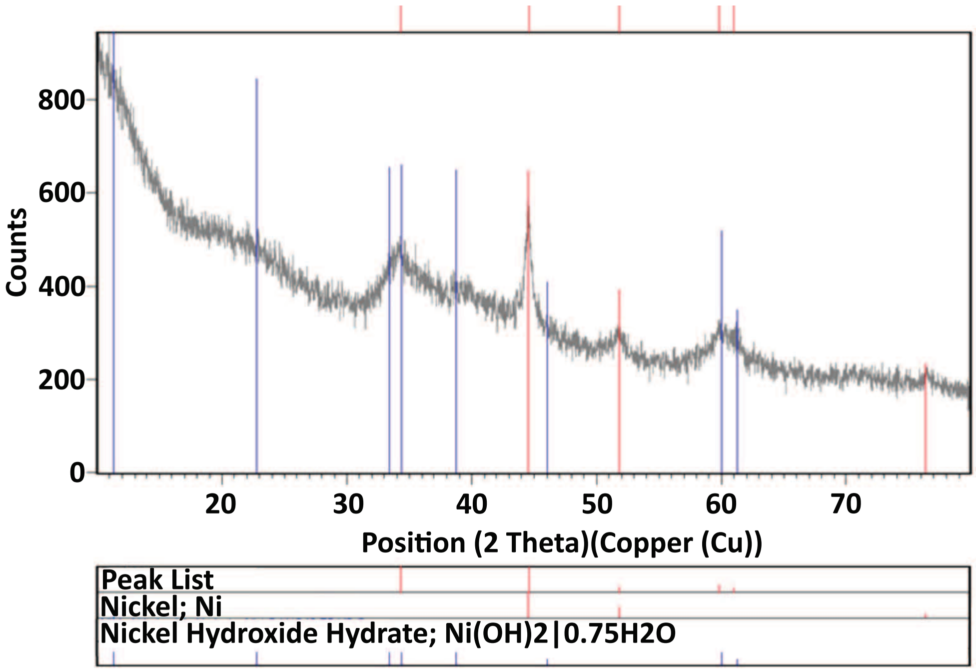

Figure 3.5: XRD pattern of the electrodeposited nickel hydroxide film.

3.4.3 Electrochemical Characterization

In this section, we discuss the results of cyclic voltammetry, electrochemical impedance spectroscopy, charge/discharge measurements as well as the durability of the differently fabricated $Ni(OH)_2$ film electrodes. Note that all electrochemical tests are performed in concentrated potassium hydroxide. Thus, the fabricated α-$Ni(OH)_2$ is dehydrated and converts into β-$Ni(OH)_2$.

Cyclic voltammetry

Cyclic voltammetry is commonly used to identify both capacitive and faradic currents which result from the application of a cycling potential. In this section, we present cyclic voltammograms (CVs) of differently fabricated $Ni(OH)_2$ thin films that we term *conventional*, *patterned* or *patternless* electrode. Here, the term conventional electrode means that the $Ni(OH)_2$ film is electrodeposited on a commercially available nickel sheet where the surface has been roughened with emery paper. The patterned and patternless electrodes are both deposited on glass and share most of the fabrication steps as described in subsection Microfabrication; however, one nickel surface is patterned with the micro-pillars while the other is plain. All CVs are measured in an aqueous 1M KOH electrolyte. The measured currents are normalized with the footprint area of the electrode. We initially perform a few cycles at a scan rate of $v = 0.5\, mVs^{-1}$ to condition the electrode. On average, around 20 cycles are required to obtain a steady and reproducible CV for the patterned or patternless electrodes while the conventional electrode requires fewer cycles for conditioning.

Figure 3.6 shows the CVs of the conventional electrode for different scan rates ranging from $v = 0.5$ to $15\, mVs^{-1}$. Note that we use an IR-drop compensation of 75%

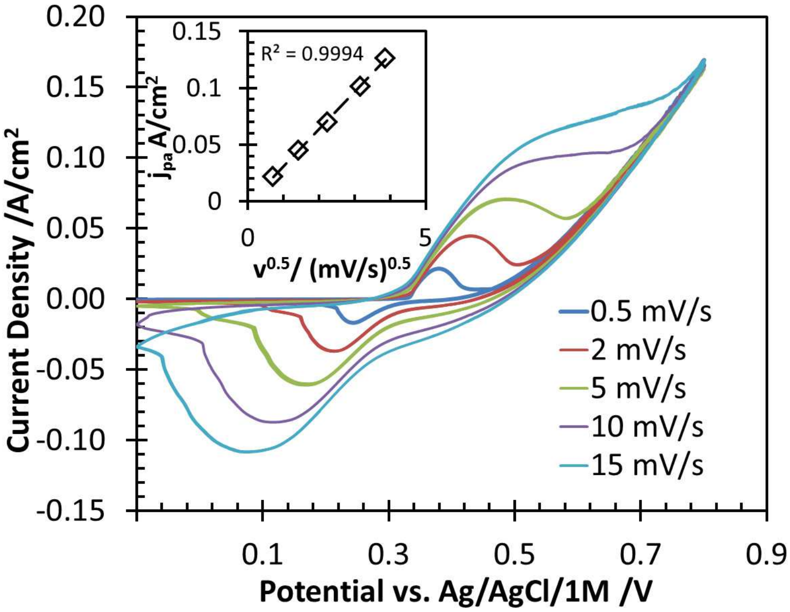

Figure 3.6: Cyclic voltammogram in 1M KOH of a thin film of $Ni(OH)_2$ deposited on a nickel sheet for scan rates of $v = 0.5$ to $15\, mVs^{-1}$. The insert demonstrates a linear correlation between the anodic current density and the square root of the scan rate.

for the measurements. Depending on the scan rate, we observe more or less distinct redox current peaks. That is, the higher the scan rate, the higher the magnitude of the measured current densities. Additionally, we observe a widening of the redox peaks with increasing scan rates. The redox peaks result from the electrochemical reaction between $NiOOH$ and $Ni(OH)_2$ where Ni^{3+} is reduced to Ni^{2+} according to:

$$\beta{-}NiOOH{+}H_2O{+}e^- \rightleftharpoons \beta{-}Ni(OH)_2{+}OH^-;\ E^{0\Theta} = 0.30\,V(\text{vs. Ag/AgCl 3M KCl}) \tag{3.3}$$

In the following, we use the classic correlations and interpretations of cyclic voltammetry derived for smooth electro-catalytic electrodes as described for example in ref.

[43]. It is understood that our $Ni(OH)_2$ films are porous substrates and not smooth surfaces and the redox reactions change the nature of the electrode surface as well. Nevertheless, since our porous films are very thin and the concentration gradients in the porous structure should be comparable to those on the surface, we think that this approach allows for a qualitative comparison. In other words, the aim of the interpretation is to quantify the variations of the differently-fabricated electrodes rather than claiming the identification of the detailed electrochemical steps.

We observe that, for increasing scan rate, the anodic and cathodic peaks shift to higher and lower potentials, respectively. We plot the anodic current density values j_{pa} versus the square root of the scan rate $\sqrt{v}$ as shown in the insert of Figure 3.6. A clearly linear correlation between these parameters is observed. The average anodic peak potential corresponds to $\bar{E}_{pa} = 0.50\,V \pm 0.11\,V$ while the cathodic peak potential is found at $\bar{E}_{pc} = 0.16\,V \pm 0.07\,V$. Hence, the average formal reduction potential corresponds to $\bar{E}^o = \frac{\bar{E}_{pa}+\bar{E}_{pc}}{2} = 0.33\,V \pm 0.02\,V$ which is in good agreement with the standard reduction potential. We further find that the difference between the anodic and cathodic peak potentials increases in a linear fashion with $\sqrt{v}$. The average peak difference is with $\Delta\bar{E}_p = 0.34\,V \pm 0.18\,V$ rather large. The ratio of cathodic to anodic peak current distinctly decreases when the scan rate increases; the average value is $\bar{j}_{pc}/\bar{j}_{pa} = 0.47 \pm 0.14$. Considering all these features of the current CVs, it is indicated that there is an intrinsic activation barrier resulting in a slow electron transfer followed by a reversible chemical step; that is, the system is quasi-reversible.

The tails in the CVs displayed in Figure 3.6 at the highest oxidation potential indicates the presence of the parasitic oxygen evolution reaction (OER). This mechanism is relatively complex and detailed investigations are outside of the scope of the present work; the reader is referred to [28] for further details on the OER in the presence of nickel. Snook et al. investigate the electrochemical performance of $Ni(OH)_2$ mixtures – consisting of $Ni(OH)_2$ particles, graphite flakes and a PTFE binder – pasted on thick nickel foil collectors. They report that the OER diminishes the mechanical integrity of their electrodes and that cycling to a lower positive switching potential stabilizes the capacity and reduces the OER so that less electrode degradation occurs [13]. We observe that our thin film electrodes, which are without any binder, have a certain stability if deposited on the metal sheet, but are very much susceptible to mechanical degradation due to OER if they are fabricated onto the glass substrate. Additionally, the potential associated with the OER decreases as the scan rate decreases. In order to measure CVs of the electrodes deposited on glass, we adjust the switching potential for each scan rate such that we observe a distinct anodic peak while avoiding oxygen evolution as much as possible.

Figure 3.7a) gives CVs of the patternless electrodes for scan rates ranging from $v = 0.5$ to $20\,mVs^{-1}$. Generally, we find distinct anodic and cathodic current peaks for all scan rates. We observe also that the magnitude and the width of the peaks increases with increasing scan rate. Additionally, the anodic peak shifts to higher potentials and the cathodic peak shifts to lower potentials when we increase the scan rate. We determine the average anodic and cathodic peak potential to be $\bar{E}_{pa} = 0.43\,V \pm 0.02\,V$ and $\bar{E}_{pc} = 0.27\,V \pm 0.01\,V$, respectively. The average peak difference over all scan rates is $\Delta\bar{E}_p = 0.16\,V \pm 0.04\,V$ while the average formal reduction potential corresponds to $\bar{E}^o = 0.35\,V \pm 0.01\,V$. Further evaluation of the CVs shows again a linear correlation between anodic peak current and the square root of the scan rate. The average ratio of the peak currents is with $\bar{j}_{pc}/\bar{j}_{pa} = 0.47 \pm 0.08$

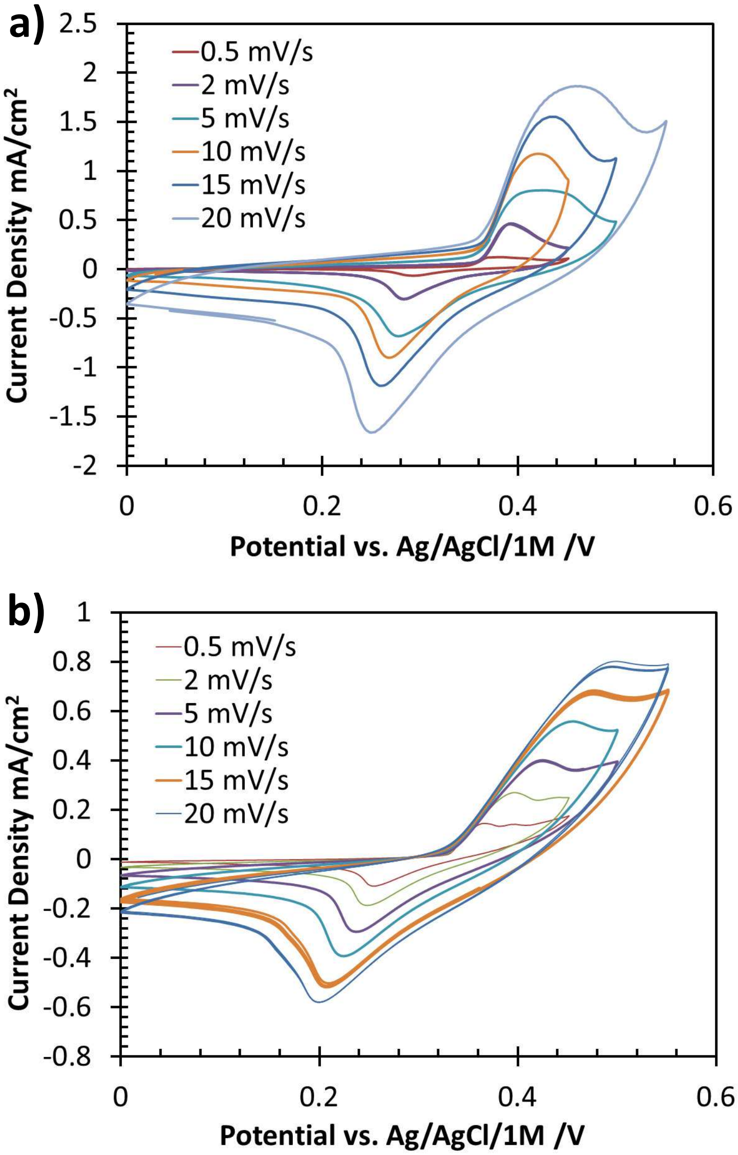

Figure 3.7: Cyclic voltammograms of the $Ni(OH)_2$ films at various scan rates for a) the patternless and b) the patterned electrode.

almost identical to that of the conventional electrode.

Figure 3.7b) gives the CVs which are measured on the patterned electrode for various scan rates in a range of $v = 0.5$ to $20mVs^{-1}$ while the switching potentials are individually adjusted. We again realize that the magnitude and the width of the redox peaks increases with increasing scan rate. Additionally, we observe a noticeable distortion of the anodic peak for all scan rates. That is, the current density approaches its maximum and more or less maintains it until the switching potential is reached. Likewise to the previous electrodes, we observe that with increasing scan rate, the difference between anodic and cathodic peaks increases. The average anodic peak potential corresponds to $\bar{E}_{pa} = 0.44\,V \pm 0.05\,V$ while the average cathodic potential is $\bar{E}_{pc} = 0.23\,V \pm 0.02\,V$. Hence, the average peak difference over all scan rates is $\Delta\bar{E}_p = 0.21\,V \pm 0.07\,V$. The average formal reduction potential corresponds to $\bar{E}^o = 0.33\,V \pm 0.01\,V$. We again find that the anodic peak current scales linearly with the square root of the scan rate. The ratio of forward to backward peak current slightly increases with the scan rate; the average value is $\bar{j}_{pc}/\bar{j}_{pa} = 0.58 \pm 0.05$.

Electrode	$\bar{E}^o/V$	$\Delta\bar{E}_p/V$	$\frac{\Delta E_p}{\sqrt{v}}/\sqrt{Vs}$	$\frac{j_{pa}}{\sqrt{v}}/\frac{A}{m^2\sqrt{V/s}}$	j_{pc}/j_{pa}
Conventional	0.33 ± 0.02	0.34 ± 0.18	0.229	10^{-4}	decreases with increasing v
Patternless	0.35 ± 0.01	0.16 ± 0.04	1.006	0.007	increases with increasing v
Patterned	0.33 ± 0.01	0.21 ± 0.07	0.652	0.019	increases with increasing v

Table 3.1: Comparison of the major CV characteristics for the differently fabricated electrodes.

Table 3.1 summarizes the major findings obtained from the measurement of the CVs. All three electrodes share similar features such as the formal reduction potential and the linear relationship between the difference of the peak potentials and the square root of the scan rate. However, significant differences are observed in the dependency of the current peak ratio and the scan rate. For increasing scan rate, we observe a decrease for the conventional electrode but an increase for both microfabricated electrodes. In terms of the “classical” CV interpretation, these characteristics indicate that the microfabricated electrodes feature a slow electron transfer followed by an irreversible chemical step contrary to the reversible one which is identified for the conventional electrode. However, as already noted we use the interpretation method only to describe the outcomes between the differently manufactured electrodes and do not claim that these are the real detailed mechanisms which occur. Additionally, the slope of the linear correlation between anodic peak current and square root of the scan rate is one order of magnitude smaller for the conventional electrode compared to those of the microfabricated electrodes. However, the material characterizations proved that the deposited films are equal in terms of composition despite the different electrode fabrication techniques. In conclusion, there is no obvious reason for these differences and the question arises whether these observations can be related to parameters other than the composition. Possible candidates are the variable turning potentials which may result in different concentration boundary layers at the electrodes, structural differences in the films, or the different current collectors which the films are deposited on; i.e. a thick nickel foil with low ohmic resistance vs. a very thin nickel layer on glass featuring a high resistance.

The difference between the anodic and cathodic peak potentials is a measure of the reversibility of the redox reactions. We find that the peak potential difference of the conventional electrode features the highest value while the patternless electrode has the lowest. That is, the reversibility of the microfabricated electrodes is better than that of the conventional one. Nevertheless, all electrodes that we measure indicate a good reversibility behavior compared to respective literature data. Wang et al. [35] fabricated electrodes from spherical clusters of $Ni(OH)_2$ nanosheets which are grown onto a nickel foam current collector and report a high value of $\Delta E_p = 0.445\,V$ at a scan rate of $2\,mVs^{-1}$. Fu et al. [21] deposited $Ni(OH)_2$ films on a nickel foil, just like our conventional electrode, featuring similar values of $\Delta \bar{E}_p \approx 0.26\,V$. Cai et al. [44] investigate $Ni(OH)_2$ meso-scale tubes and powders with measured peak potential differences of $\Delta \bar{E}_p = 0.12\,V$ and $\Delta \bar{E}_p = 0.18\,V$, respectively.

Another important parameter is the potential difference between the anodic peak and the OER. The larger the difference, the longer the electrode can be charged below the potential where the OER occurs which allows for an enhanced utilization of the electroactive material [45]. We generally observe that the potential differences of the patternless electrodes are larger than that of the patterned electrodes. Nevertheless, during our experiments it turns out that the patterned electrodes show a much better durability than the patternless electrode, especially when we cycle with switching potentials close to the OER region. That is, the patterning of the nickel surface with micropillars results in an improved stability of the nickel hydroxide films.

Despite the better electrochemical reversibility data of the microfabricated electrodes, we observe a one order of magnitude lower peak current density compared to that of the conventional electrode at a given potential. Smaller, but still considerable differences, in peak current densities between both microfabricated electrodes are found as well; the patternless electrode's peak current densities are up to twofold of the respective value of the patterned one. We assume that this is related to the varying ohmic resistances of the different current collectors and/or differences in the charge transfer resistance due to structural differences, and the difference in the roughness has an influence too.

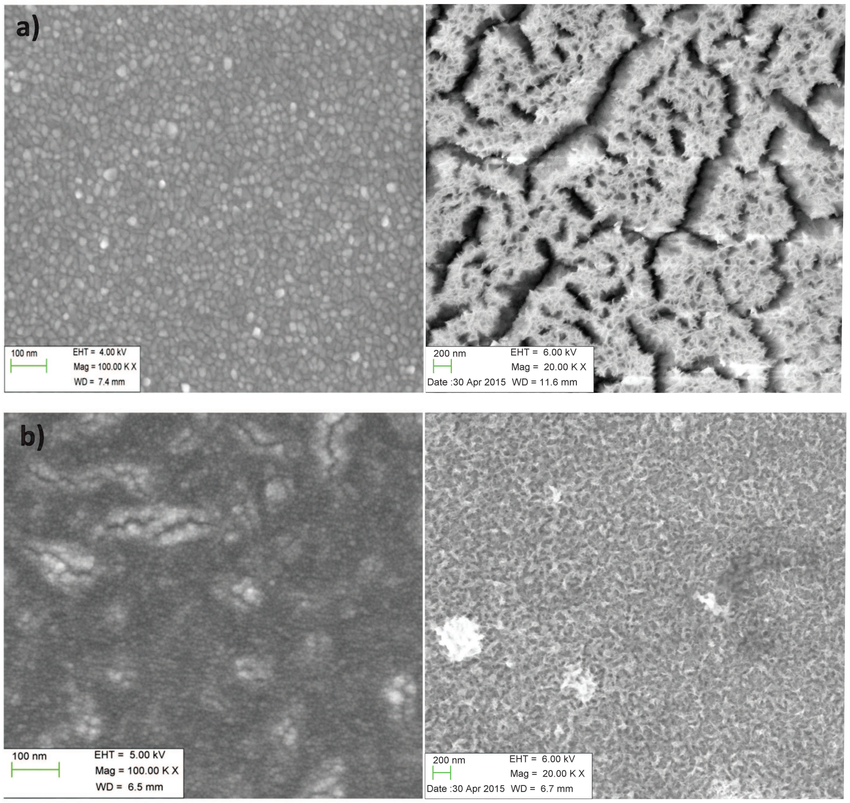

Figure 3.8: FESEM of current collector (left column) and electrodeposited $NiOH_2$ film (right column) for a) patternless electrode and b) patterned electrode.

Figure 3.8 gives an insight into the surface morphology of the a) patternless and the b) patterned electrodes by FESEM pictures. Here, the left and right column shows the surface of the current collectors and the $Ni(OH)_2$ films, respectively. We recognize that the current collector surface of the patternless electrode consists of more or less homogenously-arranged grains, while the surface of the patterned electrode, even though mainly consisting of somewhat finer grains, appears rather irregular with cracks and larger “islands”. Recall that the patterning of the electrode surface requires the lithography process with various complex chemicals, which we assume are responsible for the differences in the surface morphology. Interestingly, the situation is contrary for the electrodeposited films of $Ni(OH)_2$. That is, the surface of the patternless electrodes shows a coarse porous structure featuring many cracks despite the flawless current collector. Likewise, the patterned electrode has a finer homogeneous porous structure without cracks although the current collector was inferior. Essentially, the different $Ni(OH)_2$ film surfaces may explain the behaviour in terms of durability of the electrodes. That is, the many surface defects of the patternless electrode after the fabrication process are responsible for their limited life span.

To obtain a more quantitative statement, we employ the van-der-Pauw method [46] to determine the film (surface) resistance of the current collectors with a four-point probe station. Here, a small current is induced along the edge of the current collector while the potential is measured on the opposite edge. The film resistance R_f is then obtained from the correlation

$$\exp\left(-\frac{\pi R_A}{R_f}\right) + \exp\left(-\frac{\pi R_B}{R_f}\right) = 1 \tag{3.4}$$

where R_A and R_B are the resistances for both directions of the current collector calculated from Ohm’s law in conjunction with the applied current and measured potential. Note that the van-der-Pauw method is originally concerned with the determination of the resistivity, which can be easily inferred from $\rho = R_f d$ if the film thickness d is known. We measure area specific film resistances of around 1.38 and $2.08\,\Omega\,cm^{-2}$ for patternless and patterned electrodes, respectively. Different protocols for the lithography steps of the patterned electrodes are pursued, but we always essentially observe the film resistances mentioned above. That is, the lithography steps create surfaces with considerably higher resistances compared to the plain current collector which does not come in contact with any of the chemicals used in the lithography step. The area specific film resistance for the roughened nickel foil is measured to be $0.11\,\Omega\,cm^{-2}$. We realize that the ratios of the film resistances scale as the ratios of the peak current densities that we measure in the CVs.

We also measure the charge transfer resistance and the capacitance of the differently-fabricated micro electrodes by employing Electrochemical Impedance Spectroscopy (EIS) where we use the identical setup and conditioning as for the cyclic voltammetry measurements. In detail, EIS spectra are measured potentiostatically at a potential of $10\,mV$ and in a frequency range of $0.01\,Hz$ to $100\,kHz$. We use this small potential to avoid any redox reaction during the impedance measurements. Otherwise, the electrode surface and the conversion degree would considerably change over the measurements at low frequencies. Figure 3.9 shows the results of the EIS measurements in form of a Nyquist plot. Due to the low excitation potential along with the high capacitance of the electrodes, only a limited segment of the typical semi-circle is observed. The differences between patterned and non-patterned electrode are obvious for lower frequencies. The spectra are fitted to an equivalent circuit which consists of the serial connection of the electrolyte resistance with the parallel arrangement of the electrode charge transfer resistance and the electrode capacitance. The regression results in more or less identical capacitances of $1.85\,mF$ and $2.15\,mF$ for patterned and patternless electrode, respectively. The difference in the charge transfer resistances is more pronounced. The patternless electrode features a value of $1.53\,k\Omega$ while the patterned electrode is $4.22\,k\Omega$. It should be noted that the ohmic resistance of the current collector contributes to the charge transfer resistance. Furthermore, the ratio of the charge transfer resistances also scales approximately as the ratios of the peak current densities that we measure in the CVs. Hence, we conclude that the reason for the lower performance of the microfabricated electrodes in the CVs is due to the increased Ohmic resistance of the current collector along with a higher charge transfer resistance. While we are not sure whether we can easily optimize the charge transfer resistance of the film electrodes, it nevertheless appears promising to reduce the resistance of the current collector.

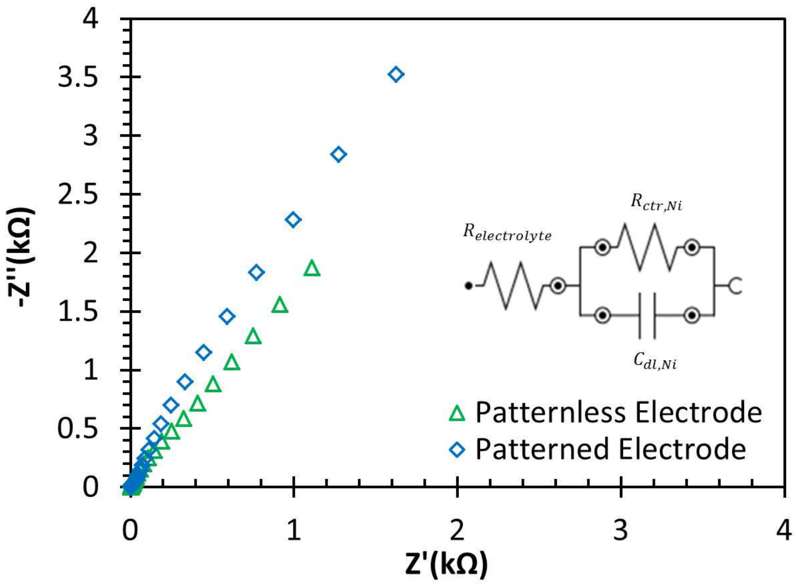

Figure 3.9: Nyquist plot of the patternless and the patterned electrode.

Charge and discharge characteristics

In this section, we examine charge and discharge characteristics of the three differently manufactured electrodes. Initially, all electrodes are preconditioned with cyclic voltammetry of low scan rates until a steady pattern is obtained; this usually takes

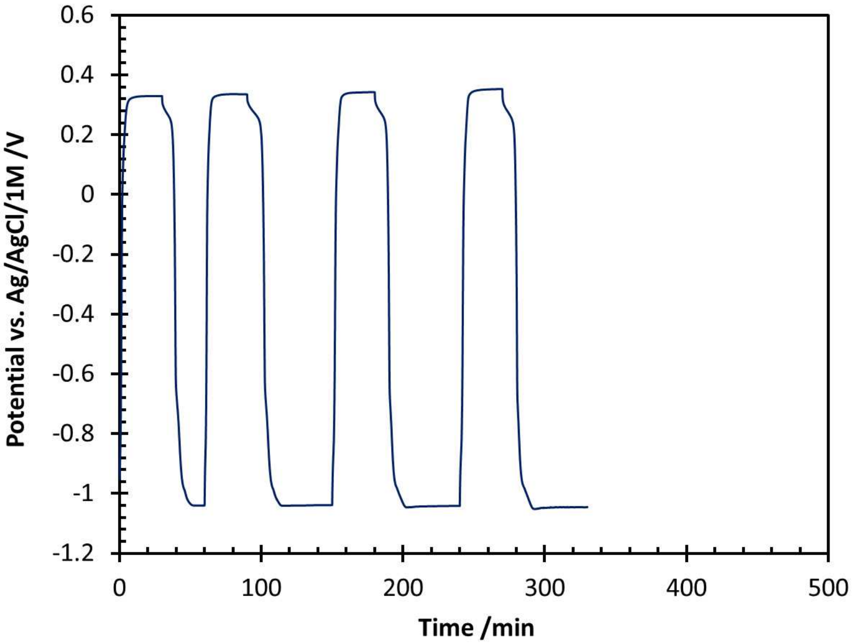

Figure 3.10: Charge and discharge behaviour of the patternless electrode at a constant current density of $0.1\, mA\, cm^{-2}$.

around 20 cycles. In terms of the charge/discharge characteristics, we have to distinguish between the capacitance, which is the charge stored in the electrical double layer (EDL), and the (faradic) capacity which is related to the electrochemical conversion. The capacitance of $Ni(OH)_2$ is relatively high and, hence, these two phenomena can be relatively easily distinguished in the charge/discharge plots. In detail, after the regime has switched from charge to discharge, we observe that the potential remains similar to the charge potential for a certain time Δt_{EDL} before it sharply drops to negative values. The associated current is capacitive which means that we first discharge the double layers before the electrochemical reaction inverts the polarity of the potential.

It is important to mention that we cannot charge the electrodes to their highest states

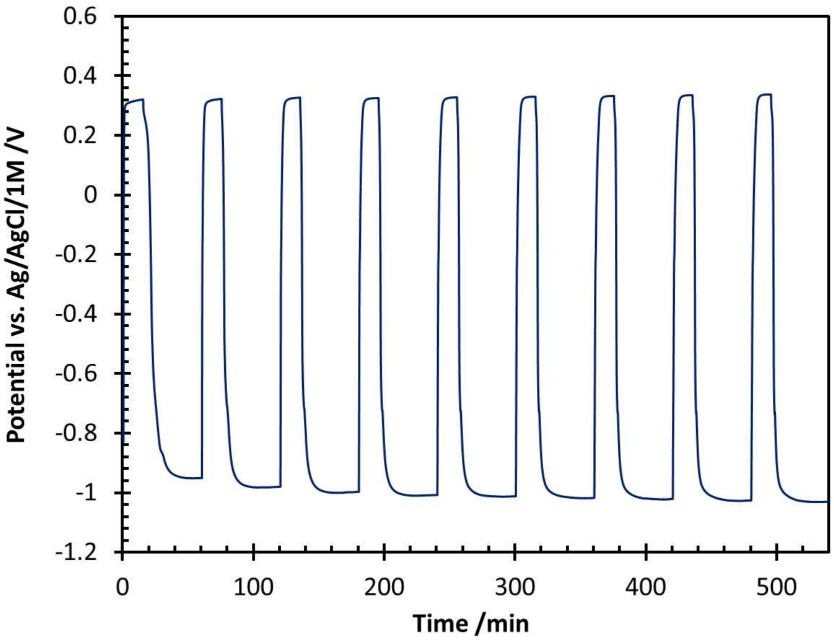

Figure 3.11: Charge and discharge behaviour of the patterned electrode at a current density of $0.1\, mA\, cm^{-2}$.

since the unavoidable potential increase triggers the OER which compromises the mechanical integrity of the films; i.e. we cannot reliably measure the maximum capacity of the electrode films. Therefore, we estimate the theoretical capacity of the films in order to infer their state of charge (SOC); i.e., the ratio of real amount of charge to that which can be theoretically stored. In detail, the electrochemical conversion occurs only at the surface of the porous thin films which is in contact with the electrolyte. Consequently, we assume that there is an electrochemically-active layer of $Ni(OH)_2$ with a thickness corresponding to the mean grain size. We define a mass specific electroactive volume $\bar{v}$ which is obtained from the product of BET surface area and the mean grain size of the $Ni(OH)_2$ film. We use a BET surface area of 62 $m^2 g^{-1}$ as reported in ref. [47]. The mean grain size is estimated using the Scherrer equation (cf. ref. [48]) while the required correlation parameters are obtained from the XRD measurements as described in subsection Materials Characterization 4.4.3. Note that this procedure is just an approximation due to the rather weak intensity of the XRD patterns. The electrochemically convertible mass of $Ni(OH)_2$ is then estimated by $V_{film}/\bar{v}$ where V_{film} is the (apparent) volume of the electrode; i.e., the electrode footprint area times the film thickness which is generally around $10\,\mu m$. Finally, the amount of charge which is required to convert the available material is calculated based on the stoichiometry of reaction (4.3). Note that in all calculations in this work a current efficiency of 100% is assumed.

At first, charge and discharge measurements of the conventional electrodes are investigated (results not shown). Since we cannot operate our microfabricated electrodes with charge/discharge current densities higher than $j = 0.1\,mA\,cm^{-2}$ without an immediate observation of electrode deterioration, we operate the conventional electrode with the same value to ensure comparability. The films are charged for 1000 minutes where we observe typical potentials of $0.30..0.35\,V$. Then, the films are discharged at the same current density for 1000 minutes to observe the electrode potential in the range of $-0.30..-0.40\,V$. For these parameters, we observe that the film electrodes deposited on the nickel foil are relatively stable. The specific capacitance of the conventional electrode is estimated via $(I \times \Delta t_{EDL})/(\Delta V \times m)$; where I is the discharge current, Δt_{EDL} is the discharge time of the EDL, ΔV is the potential drop during the discharge time, and m is the mass of the $Ni(OH)_2$ film. Based on our experimental data, we calculate a specific capacitance of around $3000\,Fg^{-1}$ which is in agreement with the work of Fu et al. [21]. Additionally, we estimate the faradic capacity to be around $250\,Cg^{-1}$ ($70\,mA\,h\,g^{-1}$) which corresponds to a

SOC of around 25%. In comparison, Chen et al. [49] reported that their electrodes compacted from a mixture of Ni and $NiOH_2$ powders feature a charge capacity of around $910\,C/g$ ($250\,mA\,h\,g^{-1}$) while the SOC is up to around 95%. Consequently, the comparison of our results to that of Chen et al. validates our method to estimate the electrochemically convertible mass of the films as outlined in the beginning of this section.

Figure 3.10 shows the charge/discharge characteristics of the patternless $Ni(OH)_2$ electrode at a current density of $0.1\,mA\,cm^{-2}$. In general, four stable cycles are observed before the first signs of film deterioration occur. The shape of the charge/discharge curves is more or less identical for all four cycles. During the charge and discharge process, the potential of the patternless electrode is around $0.32\,V$ and $-1.04\,V$, respectively.

Figure 3.11 depicts the charge/discharge characteristics of the patterned electrode at a current density of $0.1\,mA\,cm^{-2}$. Typical charge and discharge potentials correspond to around $0.3V$ and $-1\,V$, respectively; parameters which are similar to those of the patternless electrode. For these cycling conditions, we find no hint of electrode degradation even for a larger number of cycles. The capacity of the patternless and patterned electrodes are estimated to be around 140 and 70 $mA\,h\,g^{-1}$, respectively. Then, the corresponding SOC of the electrode films are 50% and 25%, respectively.

To enable a comparability of our results with those of Humble et al. [31, 32], who fabricated a roughly $100\mu m$ thick patternless films on epoxy-coated silicon, we scale their capacity with the respective film thickness and arrive at $0.4\,C\,mm^{-3}$. The much thinner patternless and patterned electrodes fabricated on glass in this work feature 0.36 and $0.1\,Cmm^{-3}$, respectively. We realize that we achieve similar values in terms of the patternless electrodes. In contrast, we do not observe the stability over a large number of cycles which is reported by Humble et al.; our patternless films last only very few cycles. An explanation could be on the one hand the different substrates (glass vs. epoxy). On the other hand there is an essential difference in the SOC. Humble et al. estimated a depth of discharge (DOD) of 10% while the electroactive materials in our patternless films are, with a SOC of 50%, utilized much more heavily. Finally, our approach to pattern the electrode surfaces does not only result in stable films, but also an increased utilization (SOC of 25%) of the electroactive materials.

3.5 Concluding Remarks

This study is concerned with the fabrication of nickel hydroxide thin film electrodes on glass substrates. A system which can be used, for instance, to realize integrated power sources on microfluidic devices. Indeed, we employ techniques which are commonly used for microfabrication along with electroplating and electrodeposition. We first utilize electron beam evaporation to deposit a chromium adhesion layer along with a nickel layer as the current collector on top of a glass surface. In the next step, nickel hydroxide films are electrodeposited onto the plane (patternless) current collector. We observe that the stability of these film electrodes is poor. Hence, we modify our film fabrication and include a lithography process in order to create a 3D array of micropillars onto the nickel current collectors. Extensive material characterization shows that, despite the utilization of multiple complex chemicals, patterned as well as patternless electrodes eventually consist of α-$Ni(OH)_2$. Cyclic voltammetry measurements of the patterned and the patternless electrodes on a glass substrate are performed and compared to comparable films deposited on a nickel sheet which serves as a benchmark case. The data that we measure indicate mainly similar electrochemical characteristics of all three electrode types, but the overall performance of the microfabricated electrodes on glass is inferior compared to those on the nickel sheet. Further investigations reveal that this can be assigned to the differences of the current collector film (surface) resistances and the charge transfer resistances. Finally, the investigation of the charge/discharge characteristics demonstrates that patterning of the electrode surface on glass results in significantly higher durability compared to a patternless surface, especially in the presence of the parasitic oxygen evolution reaction. With respect to future research, further investigations on patterning mechanisms are desirable. Here, the influence of feature size, shape and characteristic distance on the stability of the subsequently deposited electroactive films should be answered.

3.6 Acknowledgments

The authors gratefully acknowledge the financial support from the Natural Sciences and Engineering Research Council of Canada (NSERC), the Canada Foundation for Innovation (CFI), and CMC microsystems. We also thank Dr. Wojtek Halliop, research scientist at Queen's–RMC Fuel Cell Research Centre for useful discussion.

3.7 Nomenclature

d	Distance [m]
E	Potential [V]
I	Current [A]
j	Current density $[A\,cm^{-2}]$
m	Mass [g]
pa	Anodic peak
pc	Cathodic peak
R	Resistance [Ω]
t	Time (Duration) [s]
α	state of nickel
β	state of nickel
γ	state of nickel
ΔV	Potential difference [V]
ρ	Resistivity [Ω]

3.8 References

[1] Klavs F. Jensen. Microreaction engineering – is small better? *Chem. Eng. Sci.*, 56(2):293 – 303, 2001.

[2] P Abgrall and A-M Gué. Lab-on-chip technologies: Making a microfluidic network and coupling it into a complete microsystem – a review. *J. Micromech. Microeng.*, 17(5):R15, 2007.

[3] Luc Gervais, Nico De Rooij, and Emmanuel Delamarche. Microfluidic chips for point-of-care immunodiagnostics. *Adv. Mater.*, 23(24):H151–H176, 2011.

[4] Timothy S Arthur, Daniel J Bates, Nicolas Cirigliano, Derek C Johnson, Peter Malati, James M Mosby, Emilie Perre, Matthew T Rawls, Amy L Prieto, and Bruce Dunn. Three-dimensional electrodes and battery architectures. *MRS Bull.*, 36(7):523–531, 2011.

[5] Jean Louis Souquet and Michel Duclot. Thin film lithium batteries. *Solid State Ionics*, 148(34):375 – 379, 2002.

[6] L. Zhu, D. Kim, H. Kim, R.I. Masel, and M.A. Shannon. Hydrogen generation from hydrides in millimeter scale reactors for micro proton exchange membrane fuel cell applications. *J. Power Sources*, 185(2):1334 – 1339, 2008.

[7] K A Cook-Chennault, N Thambi, and A M Sastry. Powering mems portable devices–a review of non-regenerative and regenerative power supply systems with special emphasis on piezoelectric energy harvesting systems. *Smart Mater. Struct.*, 17(4):043001, 2008.

[8] Yang Yang and Jing Liu. Micro/nanofluidics-enabled energy conversion and its implemented devices. *Front. Energy*, 5(3):270–287, 2011.

[9] Arunabha Kundu, JH Jang, JH Gil, CR Jung, HR Lee, S-H Kim, B Ku, and YS Oh. Micro-fuel cells – Current development and applications. *J. Power Sources*, 170(1):67–78, 2007.

[10] Erik Kjeang, Ned Djilali, and David Sinton. Microfluidic fuel cells: A review. *J. Power Sources*, 186(2):353–369, 2009.

[11] C C Ho, J W Evans, and P K Wright. Direct write dispenser printing of a zinc microbattery with an ionic liquid gel electrolyte. *J. Micromech. Microeng.*, 20(10):104009, 2010.

[12] JFM Oudenhoven, RJM Vullers, and R Schaijk. A review of the present situation and future developments of micro-batteries for wireless autonomous sensor systems. *Int. J. Energy Res.*, 36(12):1139–1150, 2012.

[13] Graeme A. Snook, Noel W. Duffy, and Anthony G. Pandolfo. Evaluation of the effects of oxygen evolution on the capacity and cycle life of nickel hydroxide electrode materials. *J. Power Sources*, 168(2):513 – 521, 2007.

[14] Elisabet Ahlberg, Ulrik Palmqvist, Nina Simic, and Rune Sjövall. Capacity loss in Ni–Cd pocket plate batteries. the origin of the second voltage plateau. *J. Power Sources*, 85(2):245 – 253, 2000.

[15] Frank R McLarnon and Elton J Cairns. The secondary alkaline zinc electrode. *J. Electrochem. Soc.*, 138(2):645–656, 1991.

[16] Jeong Do Jin, Kim Woo-Seong, and Yung-Eun Sung. Improved electrochromic response time of nickel hydroxide thin film by ultra-thin nickel metal layer. *Jpn. J. Appl. Phys.*, 40:L708–L710, 2001.

[17] M.K. Carpenter and D.A. Corrigan. Photoelectrochemistry of nickel hydroxide thin films. *J. Electrochem. Soc.*, 136(4):1022–1026, 1989.

[18] EE Kalu, TT Nwoga, V Srinivasan, and JW Weidner. Cyclic voltammetric studies of the effects of time and temperature on the capacitance of electrochemically deposited nickel hydroxide. *J. Power Sources*, 92(1):163–167, 2001.

[19] Dan-Dan Zhao, Shu-Juan Bao, Wen-Jia Zhou, and Hu-Lin Li. Preparation of hexagonal nanoporous nickel hydroxide film and its application for electrochemical capacitor. *Electrochem. Commun.*, 9(5):869–874, 2007.

[20] Mao-Sung Wu, Yu-An Huang, and Chung-Hsien Yang. Capacitive behavior of porous nickel oxide/hydroxide electrodes with interconnected nanoflakes synthesized by anodic electrodeposition. *J. Electrochem. Soc.*, 155(11):A798–A805, 2008.

[21] GR Fu, ZA Hu, LJ Xie, XQ Jin, YL Xie, YX Wang, ZY Zhang, YY Yang, and HY Wu. Electrodeposition of nickel hydroxide films on nickel foil and its electrochemical performances for supercapacitor. *Int. J. Electrochem. Sci*, 4(8):1052–1062, 2009.

[22] Deepak P Dubal, Girish S Gund, Chandrakant D Lokhande, and Rudolf Holze. Decoration of spongelike $Ni(OH)_2$ nanoparticles onto MWCNTs using an easily manipulated chemical protocol for supercapacitors. *ACS Appl. Mater. Interfaces*, 5(7):2446–2454, 2013.

[23] Hongyuan Chen, Feng Cai, Yiran Kang, Sha Zeng, Minghai Chen, and Qingwen Li. Facile assembly of Ni-Co hydroxide nanoflakes on carbon nanotube network with highly electrochemical capacitive performance. *ACS Appl. Mater. Interfaces*, 6(22):19630–19637, 2014.

[24] Li Chen Wu, Yue Jiao Chen, Ming Lei Mao, Qiu Hong Li, and Ming Zhang. Facile synthesis of spike-piece-structured $Ni(OH)_2$ interlayer nanoplates on nickel foam as advanced pseudocapacitive materials for energy storage. *ACS Appl. Mater. Interfaces*, 6(7):5168–5174, 2014.

[25] Hongmei Du, Lifang Jiao, Kangzhe Cao, Yijing Wang, and Huatang Yuan. Polyol-mediated synthesis of mesoporous $\alpha - Ni(OH)_2$ with enhanced supercapacitance. *ACS Appl. Mater. Interfaces*, 5(14):6643–6648, 2013.

[26] Gao-Feng Han, Bei-Bei Xiao, Xing-You Lang, Zi Wen, Yong-Fu Zhu, Ming Zhao, Jian-Chen Li, and Qing Jiang. Self-grown $Ni(OH)_2$ layer on bimodal nanoporous auni alloys for enhanced electrocatalytic activity and stability. *ACS Appl. Mater. Interfaces*, 6(19):16966–16973, 2014.

[27] H. Bode, K. Dehmelt, and J. Witte. Zur kenntnis der nickelhydroxidelektrode–i. über das nickel(II)-hydroxidhydrat. *Electrochim. Acta*, 11(8):1079–87, 1966.

[28] M E Lyons and Michael P Brandon. The oxygen evolution reaction on passive oxide covered transition metal electrodes in aqueous alkaline solution. part 1-nickel. *Int. J. Electrochem. Sci.*, 3:1386–1424, 2008.

[29] Y.L. Zhao, J.M. Wang, H. Chen, T. Pan, J.Q. Zhang, and C.N. Cao. Different additives-substituted α-nickel hydroxide prepared by urea decomposition. *Electrochim. Acta*, 50(1):91 – 98, 2004.

[30] Wei-Kang Hu and Dag Noréus. Alpha nickel hydroxides as lightweight nickel electrode materials for alkaline rechargeable cells. *Chem. Mater.*, 15(4):974–978, 2003.

[31] Paul H. Humble, John N. Harb, and Rodney LaFollette. Microscopic nickel–zinc batteries for use in autonomous microsystems. *J. Electrochem. Soc.*, 148(12):A1357–A1361, 2001.

[32] Paul H. Humble and John N. Harb. Optimization of nickel–zinc microbatteries for hybrid powered microsensor systems. *J. Electrochem. Soc.*, 150(9):A1182–A1187, 2003.

[33] Jing-Shan Do, Sen-Hao Yu, and Suh-Fen Cheng. Thick-film nickel–metal-hydride battery based on porous ceramic substrates. *J. Power Sources*, 117(12):203 – 211, 2003.

[34] Jing-Shan Do, Sen-Hao Yu, and Suh-Fen Cheng. Preparation and characterization of thick-film Ni/MH battery. *Biosens. Bioelectron.*, 20(1):61 – 67, 2004.

[35] Ying Wang, Dianxue Cao, Guiling Wang, Shasha Wang, Jiyan Wen, and Jinling Yin. Spherical clusters of $\beta\text{-}Ni(OH)_2$ nanosheets supported on nickel foam for nickel metal hydride battery. *Electrochim. Acta*, 56(24):8285 – 8290, 2011.

[36] Michael EG Lyons, Anja Cakara, Patrick O'Brien, Ian Godwin, and Richard L Doyle. Redox, pH sensing and electrolytic water splitting properties of electrochemically generated nickel hydroxide thin films in aqueous alkaline solution. *Int. J. Electrochem. Sci*, 7:11768–11795, 2012.

[37] Dennis A. Corrigan. The catalysis of the oxygen evolution reaction by iron impurities in thin film nickel oxide electrodes. *J. Electrochem. Soc.*, 134(2):377–384, 1987.

[38] Dennis A. Corrigan and Richard M. Bendert. Effect of coprecipitated metal ions on the electrochemistry of nickel hydroxide thin films: Cyclic voltammetry in 1M KOH. *J. Electrochem. Soc.*, 136(3):723–728, 1989.

[39] Andrew P. Grosvenor, Mark C. Biesinger, Roger St.C. Smart, and N. Stewart McIntyre. New interpretations of XPS spectra of nickel metal and oxides. *Surf. Sci.*, 600(9):1771 – 1779, 2006.

[40] Lee M. Moroney, Roger St C. Smart, and M. Wyn Roberts. Studies of the thermal cecomposition of βNiO(OH) and nickel peroxide by X-ray photoelectron spectroscopy. *J. Chem. Soc., Faraday Trans. 1*, 79:1769–1778, 1983.

[41] K.S. Kim and Nicholas Winograd. X-ray photoelectron spectroscopic studies of nickel-oxygen surfaces using oxygen and argon ion-bombardment. *Surf. Sci.*, 43(2):625 – 643, 1974.

[42] P.Vishnu Kamath and G.N. Subbanna. Electroless nickel hydroxide: Synthesis and characterization. *J. Appl. Electrochem.*, 22(5):478–482, 1992.

[43] CH Hamann, A Hamnett, and W Vielstich. *Electrochemistry.* Wiley-VCH, 2007.

[44] Feng-Shi Cai, Guo-Ying Zhang, Jun Chen, Xing-Long Gou, Hua-Kun Liu, and Shi-Xue Dou. $Ni(OH)_2$ tubes with mesoscale dimensions as positive-electrode materials of alkaline rechargeable batteries. *Angew. Chem. Int. Ed.*, 43(32):4212–4216, 2004.

[45] Weiyang Li, Shaoyan Zhang, and Jun Chen. Synthesis, characterization, and electrochemical application of $ca(oh)_2$–, $co(oh)_2$–, and $y(oh)_3$–coated $ni(oh)_2$ tubes. *J. Phys. Chem. B*, 109(29):14025–14032, 2005.

[46] LJ van der Pauw. A method of measuring specific resistivity and hall effect of discs of arbitrary shape. *Philips Res. Rep.*, 13:1–9, 1958.

[47] Debao Wang, Caixia Song, Zhengshui Hu, and Xun Fu. Fabrication of hollow spheres and thin films of nickel hydroxide and nickel oxide with hierarchical structures. *J. Phys. Chem. B*, 109(3):1125–1129, 2005.

[48] F. W. Jones. The measurement of particle size by the X-Ray method. *Proc. R. Soc. London, Ser. A*, 166(924):16–43, 1938.

[49] J. Chen, D. H. Bradhurst, S. X. Dou, and H. K. Liu. Nickel hydroxide as an active material for the positive electrode in rechargeable alkaline batteries. *J. Electrochem. Soc.*, 146(10):3606–3612, 1999.

Chapter 4

Fabrication and Characterization of Thin-Film Metal Hydride Electrodes for Microbattery Applications[1]

4.1 Abstract

Utilization of micropower sources has attracted considerable attention especially in the field of portable microfluidic devices for which only small power densities and energy contents are required. In the present work, we report on the microfabrication of thin films of metal hydride electrodes on glass substrates which can be utilized for rechargeable microbatteries as well as for hydrogen sensing or storage applications.

---

[1] To be submitted for publication

A multi-layer deposition technique is developed by employing electron beam evaporative and sputtering techniques. The morphology and the structure of the metal hydride film electrodes are studied by using Field Emission Scanning Electron Microscopy coupled with an Energy Dispersive Spectroscopy module. We investigate the surface elemental composition of the metal hydride films using x-ray photoelectron spectroscopy method. Additionally, cyclic voltammetry and galvanostatic charge–discharge measurements are performed to evaluate the electrochemical performance of the electrodes. Finally, a semi-empirical model is derived to allow for the determination of the Galvani potential of the electrode as a function of its hydrogen content.

4.2 Introduction

Micro Electro Mechanical Systems (MEMS) as well as microfluidic systems have attracted considerable attention since they offer size reduction and integration of several functions on a single unit. These devices exceed the features of conventional systems, yet maintain the potential of being mass produced at low costs [1]. For instance, technological microfluidic concepts are comprised of Lab-on-a-Chip (LOC) [2] and Point-of-Care-Testing (POCT) [3] which applications are chemical analytics and medical diagnostics, respectively. Despite the development of such devices over the last decades, the supply of electrical power to these devices continues to impose a barrier since developments on power source miniaturization have not kept the same pace. An attractive approach to power micro devices seems to be the use of embedded power supplies within the device. However, sub-millimeter power sources with low power and energy densities have not yet been developed due to constraints on packaging, fuel storage, fuel delivery, and power generation [4].

Attempts to miniaturize electrical power supplies are limited and they are comprised of regenerative power technologies such as micro photovoltaic arrays, thermoelectric, electrostatic, and piezoelectric devices [5, 6] as well as non-regenerative power supplies, which have a finite amount, or continuous supply of active materials for power generation, such as microfluidic fuel cells [7]. Here, microbatteries are attractive since the battery chemistry is usually indistinguishable from conventional (macro) batteries. Though configurations, material deposition, post-processing and packaging methods applicable to macrobatteries are oftentimes not feasible below the centimeter scale and the resulting microbattery performance does not proportionally scale at such micro-scale dimensions [8]. Microbatteries typically utilize thin or thick films of electroactive materials which can be printed or deposited by various methods including sol-gel, electrodeposition, physical and chemical vapor deposition or atomic layer deposition [9].

In the current work, we investigate the fabrication of a hydrogen absorbing film which can be utilized for a nickel metal hydride (NiMH) microbattery. In general, hydrogen absorbing metal alloys can be used for many applications including hydrogen storage, hydrogen purification, hydrogen sensors and catalysts [10, 11], heat pumps [12], and cooling systems [13], along with the NiMH batteries. This wide range of applications is attributed to the reversibility of the hydrogen sorption, in particular, in AB_5-type intermetallic alloys [14]. AB_5 hydrogen absorbing metal alloys have a relatively low equilibrium pressure, a relatively high storage capacity paired with fast reaction kinetics [15] which makes them attractive choices in various commercialized and conventional battery applications as a negative electrode of NiMH batteries and microbatteries. The majority of research on $LaNi_5$ and its derivatives as a battery material published over the last decade is concerned with bulk/particulate hydrogen metal alloys such as in refs.[16, 17, 18, 19, 20]. The blending of additional elements in $LaNi_5$ can be beneficial in many aspects which is especially true for adding small amounts of aluminium Al. In detail, Liu et al. investigated that the partial substitution of Al in the B-site of the $LaNi_5$ alloy improves not only the cycling performance but also the anti-electro-oxidation and polarization ability [21]. Other works indicate that the addition of Al reduces the corrosion of the electrode which is mainly based on the formation of a protective oxide layer [22, 18]. Furthermore, Mendelsohn et al. have reported that the addition of Al reduces the plateau pressure of the metal alloys [23] which ultimately improves the activation process [24, 25]. This is of particular interest especially for microbatteries, as the in-situ activation of such metal alloys is not an easy task [25]. The addition of Al also results in an enhanced life cycle in electrochemical performance measurements and applications [26]. Given the multiple advantages of the Al addition, we consider alloys of $LaNi_{5-x}Al_x$ as promising electrode materials for a NiMH microbattery.

In terms of micropower applications, it is also promising to integrate the battery during the fabrication process of the microdevice. Consequently, this approach requires that the battery is manufactured with standard microfabrication techniques onto the state of the art materials. Traditionally, the metal hydride electrode of a NiMH battery has been prepared by adding binders to the intermetallic powder; an approach which does not appear suitable for microdevices. In terms of substrates, it is common to fabricate micro and microfluidic devices onto silica and/or its derivative such as glass. Hence, the typical microfabrication technique Physical Vapor Deposition (PVD) is used in this work to deposit films of $LaNi_{5-x}Al_x$ on glass substrates. Here, PVD is a synonym for a class of deposition techniques and several methods have been reported to deposit films of metal alloys such as ion sputtering [27], ion plating [28], RF magnetron sputtering/flash evaporation-deposition [29, 30, 31], and DC sputtering [32]. The utilization of a conventional evaporation method is not possible for $LaNi_{5-x}Al_x$ due to the significant difference in the vapor pressures of these metals. To the best of our knowledge, only very few works in the literature are concerned with the sputtering of $LaNi_5$ and its derivatives such as refs.[31, 33]. These works are mainly concerned with the characteristics as a hydrogen storage material but not with their performance as electrode for battery applications. One exception is the work of Wang et al. who reported on the electrochemical hydrogen storage capability of $LaNi_{4.25}Al_{0.75}$ alloy deposited on a copper substrate [34]. They consider the utilization of MH film electrodes as beneficial compared to bulk MH materials due to the higher thermal conductivity, good resistance to hydrogen pulverization and the formation of protective and catalytic layers [34]. In terms of pulverization, Adachi et al. [30] (as cited in [35]) noted that the volume increase associated with the hydride formation leads to mechanical stress in the hydride envelope surrounding the unhydrided core material. For further details on the phase change of MH materials, the reader is referred to ref.[31].

The objective of this work is twofold: On the one hand, we investigate the possibility of deposition of stable films of $LaNi_{5-x}Al_x$ on glass substrates using microfabrication methods. On the other hand, we study the electrochemical performance of such films in alkaline electrolytes in terms of electrolytic (de-)hydrogenation. This article continues with a section on the experimental methodologies and materials followed by a thorough discussions of our experimental results. Additionally, a model is introduced to infer the Galvani (equilibrium) potential of the MH electrode as a function of the hydrogen content from a single (dis)charge measurement. Such correlation is important not only for electrochemical characterization but also for the utilization of the electrodes as a hydrogen sensor. Finally, the article is summarized with some concluding remarks.

4.3 Experimental Methods and Materials

In this section, we specify materials, fabrication and characterization techniques which are used in the present work.

4.3.1 Microfabrication

Materials: Glass microscope slides (Fisher Scientific, Canada and Globe Scientific Inc., USA) of area 2.54 by 7.62 cm are used as substrates. Nickel and chromium pellets (Kurt J. Lesker Canada, Inc., Canada) with purities of 99.995% and 99.998% are used for the physical vapour deposition (PVD) of the thin films which serve as sticky layer and current collector, respectively. Ultra high purity hydrogen gas is used in all gas-sorption experiments (Grade 5-MEGS, Canada). The deposition material $LaNi_{5-x}AL_x$ is customized from Kurt J. Lesker Canada, Inc.. We receive the same material in two states from the manufacturer; i.e., as an ingot which serves as a target and as a powder for the hydrogen sorption testing. The size and purity of the target ingot are reported by the manufacturer to be 7.62 cm in diameter and 99.9%, respectively. The thickness of the target is $0.317 \pm 0.025\,cm$.

Instruments: Metal thin films of chromium and nickel are prepared using an electron beam evaporator (Balzers, USA). In terms of $LaNi_{5-x}AL_x$ films, we use a Varian in-house built metal sputter deposition system with the ability to work on either RF or DC mode. Temperature and argon pressure can be controlled within the sputter chamber. All film depositions are performed at the Microelectronics Fabrication Laboratory (MFL) at Carleton University in Ottawa, Canada. The hydrogen sorption characteristics of the target ingot materials are tested by employing a gravimetric technique using an in-house built instrument as described in ref.[36].

4.3.2 Materials and Physical Characterizations

The elemental composition of the deposited films is examined using an X-ray diffraction (XRD) instrument (X'Pert Pro, Philips Analytical B.V., The Netherlands) via Cu K-alpha radiation. The diffractometer is operated at $40\,kV$ and $45\,mA$. The raw data is analyzed using the X'Pert Highscore Pro software. Additionally, we employ an X-ray photoelectron spectrometer (XPS) (Thermo Instruments 310-F Microlab) using the Mg Kα method to gain further insights into the film composition. We also use a field emission scanning electron microscope equipped with an energy dispersive spectrometer(FESEM/EDS)(detector with a resolution of $129\,eV$ at Manganese and a light element detection limit of Boron, LEO 1530, Zeiss) to investigate the surface morphology and elemental composition of the films. A stylus profiler (TENCOR Instruments P-1; Long Scan Profiler) is employed to measure the thickness of the deposited films.

4.3.3 Electrochemical Characterization

The deposited intermetallic films are electrochemically characterized with cyclic voltammetry and galvanostatic charge-discharge measurements by utilizing a combined potentiostat/galvanostat (PGSTAT302N, Metrohm Autolab B.V., The Netherlands). Here, a three-electrode setup is employed consisting of the working electrode (La-Ni-Al), reference electrode (Ag/AgCl in 3M KCl, double junction, Metrohm Autolab B.V., The Netherlands) and a counter electrode (Pt-wire-mesh, Metrohm Autolab B.V., The Netherlands). All electrochemical measurements are performed in aqueous $1M$ potassium hydroxide (KOH) solutions at a room temperature of $23°C$. We also measure cyclic voltammograms (CVs) for electrolyte concentrations of $0.75M$, $0.5M$, $0.25M$ and $0.125M$ to investigate the effect of the electrolyte concentration on the electrochemical performance of the film electrodes. All electrolyte solutions are prepared with deionized water having a conductivity of approximately $2\,\mu S\,cm^{-1}$. Conductivities and pH values are tested using a modular pH and conductivity meter (Mettler-Toledo, SevenMulti, Switzerland). All chemicals are ACS grade and purchased from Sigma-Aldrich, Canada. Note that, the electrolyte solution is deoxygenated via bubbling with high purity nitrogen gas (99.999%) during the experiments in order to suppress unwanted side reactions.

4.4 Results and Discussion

In this section, we first give insights into the characteristics of the target materials used to fabricate the film electrodes by employing a DC magnetron sputter. Then, the sputtered film electrodes are characterized in terms of material (elemental) composition and surface morphology. Finally, we discuss our results obtained from the electrochemical characterization and introduce our modelling approach.

4.4.1 Target Material Characterization

The motivation for the target material characterization is twofold: On the one hand, the target material is custom-made using an arc-melting method by the manufacturer and its accurate material (elemental) composition has to be determined. On the other hand, we would like to obtain the gaseous hydrogen sorption capacity and the activation characteristics of this material. We perform these measurements because we can compare the results with those of intermetallic alloys previously reported in our work in ref.[36]. The hydrogen sorption measurements are more precise since a larger sample size can be tested compared to measuring hydrogen capacity of the very little mass of the film that we sputter as an electrode. Many researchers, such as [37, 38, 39, 11], have emphasized the similarity between the gas-solid sorption and the electrolytic (de-)hydrogenation mechanisms at the interfaces. In the latter one, the equilibrium potential as a function of hydrogen concentration in the electrode can be utilized to analyze the relationship between the hydrogen pressure and the hydrogen content at a given temperature for hydrogen sorption alloys. We use this analogy to bridge the gap between the gaseous hydrogen sorption and the electrolytic (de-)hydrogenation mechanisms when we derive a model for the electrolytic (de-)hydrogenation, and compare it to a similar model for the gas sorption. Hence, we receive the same material in two states from the manufacturer; i.e., as an ingot to serve as a target and as powder to be used in the hydrogen sorption measurements.

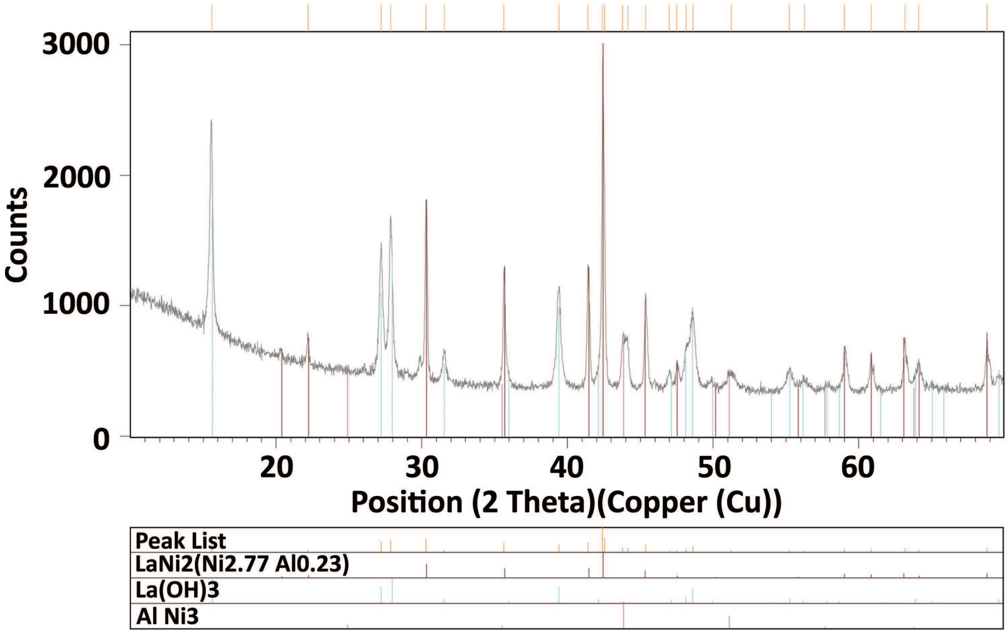

Figure 4.1: XRD pattern of the target material as received from the manufacturer.

We proceed this section with an investigation of the target material (elemental) composition. Figure 4.1 depicts the result of the XRD measurement. The XRD instrument operating software is used to obtain the elemental composition. We obtain an empirical formula of $LaNi_{4.77}Al_{0.23}$ for our target (ingot) which is relatively close to the formula reported by the manufacturer, i.e., $LaNi_{4.7}Al_{0.3}$. In terms of crystallographic parameters, we obtain lattice parameters and a cell volume as listed in Table 4.1. The XRD pattern along with the lattice parameters are in good agreement with the elemental composition which corresponds to $LaNi_{4.7}Al_{0.3}$ as reported in refs.[21, 40, 41]. The small deviations can be attributed to the variation in the elemental composition of the alloy studied in the present work. Moreover, we observe relatively sharp peaks in the XRD pattern indicating that the target features a crystalline metal structure. To further investigate the elemental composition at the surface, we perform XPS analysis on the powder-like target materials (results not shown). The XPS results also confirm the presence of lanthanum and aluminium oxide on the surface while nickel can be mainly observed in the underneath layers.

Parameter	$LaNi_{4.77}Al_{0.23}$ (This work)	$LaNi_{4.7}Al_{0.3}$ [21, 40]	$LaNi_{4.7}Al_{0.3}$ [41]
a ($\mathring{A}$)	5.0260	5.0270	5.02447
c ($\mathring{A}$)	3.9980	4.0041	4.00372
Cell volume ($\mathring{A}^3$)	87.46	87.6301	87.5

Table 4.1: Lattice parameters and volume of cell.

We now discuss our results obtained from the hydrogen sorption measurements. Figure 4.2 illustrates pressure–concentration (P-C) isotherms of the $LaNi_{4.77}Al_{0.23}$ intermetallic compound at three temperatures, $23\,°C$, $40\,°C$, and $60\,°C$. All hydrogen pressure values are scaled with a reference pressure of $P_{ref} = 1\,bar$ while the hydrogen concentration values are scaled with the maximum of the measured hydrogen content. In Figure 4.2, the solid and the open symbols denote the absorption and the desorption isotherms, respectively. Generally, we observe equilibrium pressures (plateaus) increase with increasing temperature. Additionally, the presence of a considerable hysteresis in the sorption process is indicated by the difference in the absorption and the desorption isotherms at a given temperature. Overall, when we compare the sorption values of the $LaNi_{4.77}Al_{0.23}$ alloy to the work we previously reported in ref.[36], we observe that the plateau pressure values are lower (at $T = 23\,\&\,40°C$). This can be attributed to the substitution of Al element in the B-site of the lattice structure of pure $LaNi_5$ alloy.

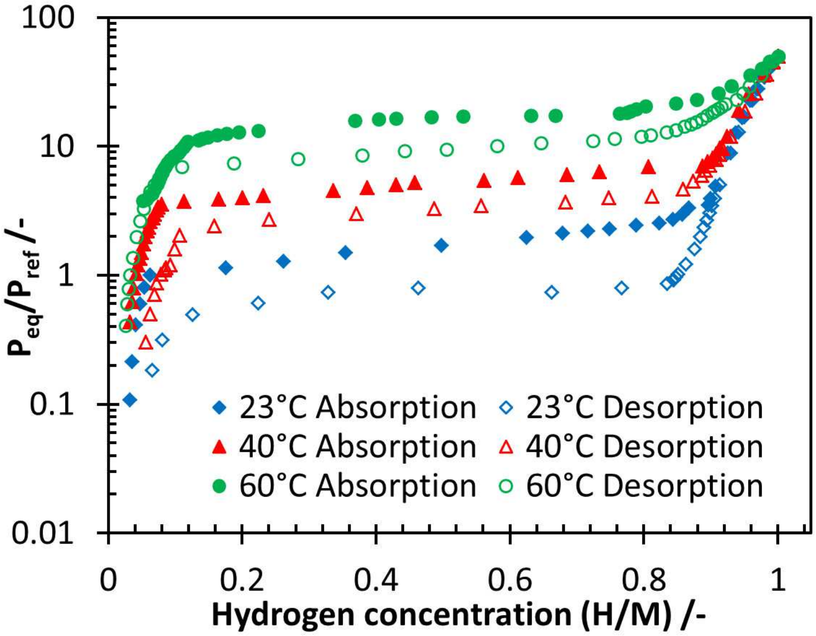

Figure 4.2: P-C isotherms of $LaNi_{4.77}Al_{0.23}$ target at three temperatures as received from the manufacturer.

In detail, a summary of the plateau pressure values of pure $LaNi_5$ (from ref.[36]) and Al-substituted alloy (used in this study) is given in Table 4.2. Given the non-ideality of the plateaus –ie., they feature a slope– only the mid-point plateau pressure values are reported here for the sake of comparison. Generally, we obtain lower plateau pressure values (absorption and desorption) of $LaNi_{4.77}Al_{0.23}$ in comparison with those of pure $LaNi_5$ at temperatures of 23 and 40 $^{\circ}C$. The plateau pressures of $LaNi_5$ are almost twice of those of the Al-substituted alloy at 23 $^{\circ}C$. However, we realize that the advantage in plateau pressure strongly depends on the temperature. At a temperature of 40 $^{\circ}C$, the plateau pressure values of Al-substituted alloy, for absorption and desorption, are only roughly 20% lower than those of pure $LaNi_5$. At a temperature of 60 $^{\circ}C$, we even observe higher plateau pressures for the $LaNi_{4.77}Al_{0.23}$

alloy than those for the $LaNi_5$ alloy. Additionally, we observe that the $LaNi_{4.77}Al_{0.23}$ can be activated easier than the $LaNi_5$ alloy. In terms of $LaNi_5$ alloy, the activation occurs over three days with a temperature and pressure of $180\,^oC$ and $30\,bar$, respectively. Then, the sample is cooled down to ambient temperature while the hydrogen pressure is maintained at $30\,bar$ for another three days before a few absorption and desorption cycles are performed during heating and cooling of the samples. In contrast, we are able to activate our $LaNi_{4.77}Al_{0.23}$ materials without high temperature and high pressure activation process by leaving the sample at a hydrogen pressure of about $5\,bar$ and ambient temperature of around $23\,^\circ C$ for four days. We attribute the easier activation process to the lower equilibrium pressure (plateau pressure) of the Al-substituted $LaNi_5$ alloy which also has been stated by others such as refs.[23, 24, 25].

In conclusion, our investigation shows that the addition of Al to $LaNi_5$–type metal results in better sorption characteristics at low temperatures along with an easier activation. Further, it can be inferred that for the same activity of hydrogen, a higher concentration of hydrogen in the metal (hydride) can be obtained at a lower equilibrium pressure. Hence, we favor the $LaNi_{4.77}Al_{0.23}$ alloy over the $LaNi_5$ in terms of electrode materials in micropower supplies where low temperatures are desired. We should also mention that the further addition of palladium to $LaNi_{4.7}Al_{0.3}$ –as reported in ref.[25]– may offer even easier material activation process. However, we expect that the increased complexity of such multi-component film deposition outweighs the further ease of the activation process.

Alloy/Temperature	$23\,^{\circ}C$	$40\,^{\circ}C$	$60\,^{\circ}C$
$LaNi_5$ Absorption (kPa)	335	614	1310
$LaNi_5$ Desorption (kPa)	188	394	853
$LaNi_{4.77}Al_{0.23}$ Absorption (kPa)	173	530	1560
$LaNi_{4.77}Al_{0.23}$ Desorption (kPa)	81	315	928

Table 4.2: Approximate mid-plateau pressure values of $LaNi_5$ (from ref.[36]) and $LaNi_{4.77}Al_{0.23}$.

4.4.2 Microfabrication

The La-Ni-Al film electrodes are fabricated using microfabrication techniques which are commonly utilized in the semiconductor industries. The different process steps are illustrated in Figure 4.3. The microscope glass slide is first subjected to a cleaning process involving ammonium hydroxide NH_4OH, hydrogen peroxide H_2O_2, and de-ionized water consecutively. The glass slide is transferred to the e-beam evaporation chamber where the chromium adhesion layer (step 1 shown in Figure 4.3) and subsequently the nickel current collector layer (step 2 shown in Figure 4.3) are grown; each film thickness is $60\,nm$. This step is required since nickel does not adhere to a glass surface very well; hence, we first deposit a thin layer of chromium –as an adhesion (seed) layer– onto the glass surface. The glass substrate with the nickel current collector is then transferred to the sputter chamber for the deposition of the La-Ni-Al film layer (step 3 shown in Figure 4.3). We measure the La-Ni-Al film thickness to be around $1.1\,\mu m$ by employing a stylus profiler. The operating conditions used to sputter the intermetallic films onto the glass substrates are listed in Table 4.3.

The deposited $LaNi_{5-x}Al_x$ film electrode is then undergone various material characterizations.

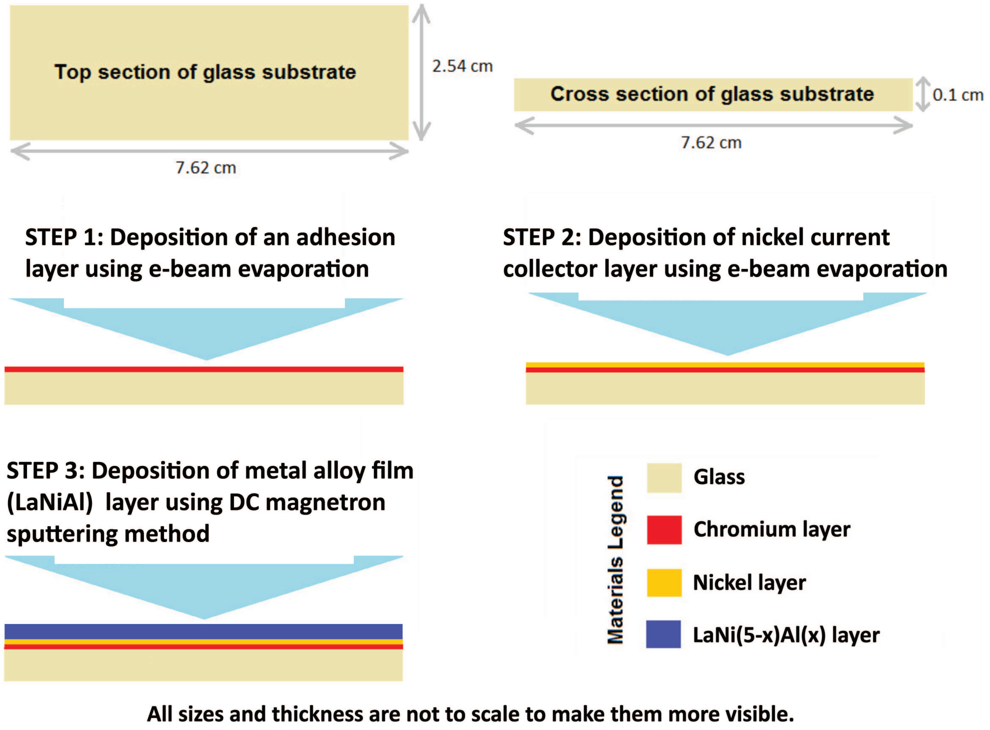

Figure 4.3: Fabrication process flow of the metal hydride film electrode on a glass substrate.

Parameter	Value
Vacuum pressure	$< 10^{-5}\,Pa$
Argon gas partial pressure	$0.53\,Pa$
Argon gas purity	99.999%
Target purity (as reported by the manufacturer)	99.9%
Approximate distance between substrate and target	$10\,cm$
Sputtering method	Magnetron DC
Sputtering power	$100\,W$
Deposition rate	$0.11\,nm\,s^{-1}$
Substrate temperature during deposition	$25\,^{\circ}C$

Table 4.3: Sputtering conditions used for the deposition of the La-Ni-Al film electrodes in this work.

4.4.3 Materials Characterization of the Sputtered Film Electrode

We use EDS and XPS methods to gain insights into the composition and morphology of the microfabricated intermetallic film electrodes. Figure 4.4 shows the EDS spectrum of the intermetallic La-Ni-Al film electrode. Generally, we see that most peaks correspond to nickel Ni and lanthanum La; we find also a small percentage of aluminium Al at around $1.5\,keV$. Additionally, the small amount of carbon at around $0.35\,keV$ indicates the presence of some impurities in our target, a cross-contamination in the sputter chamber, or impurities in the argon gas used during sputtering. Further EDS measurements at different sections of the electrode surface confirm carbon is present throughout the surface. We also measure a very small amount of cobalt Co –estimated to be around $0.06 \pm 0.12\,wt\%$– which is not visually identifiable in the spectrum. By offsetting carbon and cobalt contents, we obtain an approximate composition of $La_{1.11\pm0.05}Ni_{4.73\pm0.02}Al_{0.19\pm0.02}$ based on the EDS method. We conclude that the elemental compositions of the sputtered films are in a good agreement with the concentrations of the metal elements in the target which is used for sputtering.

The insert in Figure 4.4 gives a snapshot of the surface morphology of the microfabricated film electrode. We observe a relatively uniform grain size of roughly $20\,nm$ throughout the electrode surface which is basically a nanocrystalline structure. In comparison, Smardz et al. measured a grain size of $15\,nm$ of the nanocrystalline structures of sputtered $LaNi_5$ films which were made at $22\,°C$ with an argon partial pressure of $0.05\,Pa$ [32]. The relatively larger grain size of our films can be attributed to the higher argon partial pressure that we use for sputtering, i.e., $0.53\,Pa$. We also perform XPS measurements to investigate the elemental composition at the surface of the film electrodes. We measure the spectra of our samples ex-situ, because the XPS instrument is not coupled with the sputter chamber, and do not perform any surface etching due to the small thickness of the films. Figure 4.5 gives the results for the sputtered MH film electrode. In detail, Figure 4.5(a) shows a wide scan over the entire binding energy (BE) range while Figures 4.5(b),(c) and (d) illustrate scans of smaller BE ranges attributable to $La(3d)$, $Ni(2p)$ and $Al(2p)$, respectively. Here, the carbon offset is taken into account while the satellite peaks are not accounted for. It should also be mentioned that the presence of metal oxides is likely as we do not perform in-situ spectroscopy. We observe peaks at $841.59\,eV$ and $858.69\,eV$ which correspond to $La(3d)$ and $Ni(2p)$, respectively. Furthermore, a much lower binding energy peak is observed at $72.2\,eV$ which is attributed to $Al(2p)$. The BE values that we obtain for $La(3d)$ and $Ni(2p)$ are in agreement with ref.[32]. Overall, the spectra show that the electrode surface consists of lanthanum, nickel, aluminium, and their oxides. It can also be inferred that the elemental contents of Al- and La-compounds are slightly higher at the surface compared to Ni-compounds. Additionally, we obtain peaks for oxygen and carbon (results not shown).

The oxidation state of the nickel element at the surface is related to the binding energies and the chemical shifts in the XP spectra. Schlapbach et al. also observed that the XP spectrum of an air-exposed $LaNi_5$ powder and that of raw bulk contain oxidized nickel [42]. Note that we do not perform XRD measurements as our instrument does not measure any peak for the intermetallic films due to the small thickness of the films.

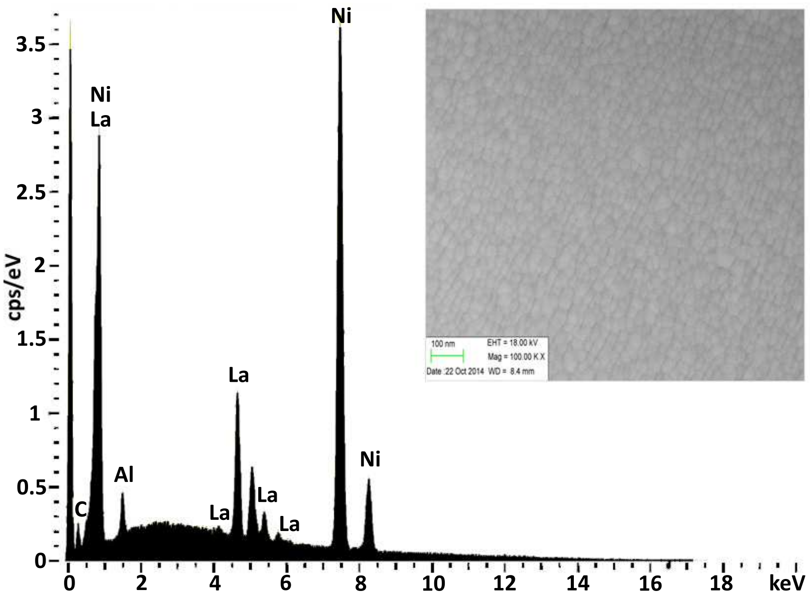

Figure 4.4: Energy Dispersive Spectrum and Field Emission Scanning Electron Micrograms (insert) of the sputtered intermetallic film at $P_{Ar} = 0.53\,Pa$; $T = 25°C$.

4.4.4 Electrochemical Characterization

In this section, we discuss the results of cyclic voltammetry and charge-discharge measurements of the intermetallic film electrodes. Also, we give an insight into how a mathematical model can describe the plateau and transition regions during hydrogenation. Finally, this section is concluded through a discussion about the effect of electrolyte concentration on the performance of the film electrodes.

Cyclic voltammetry

The cyclic voltammetry measurements of the intermetallic film electrodes, as given in Figure 4.6, are performed in an aqueous solution of 1M KOH at various scan rates. All currents are normalized with the footprint area of the electrode which is

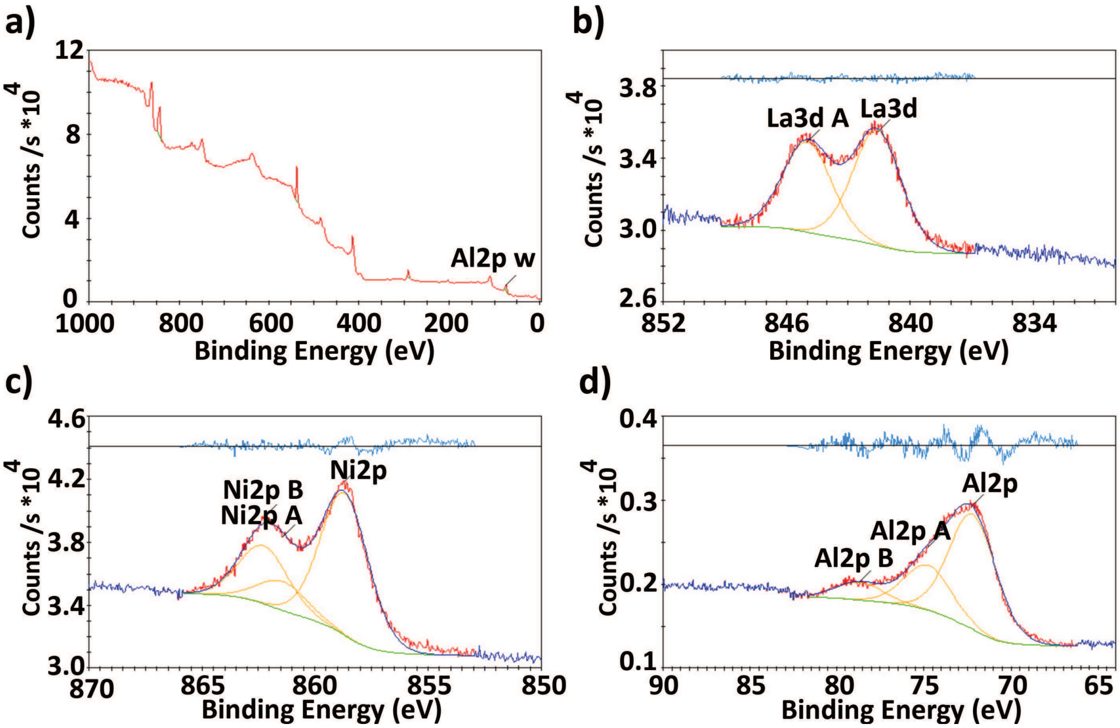

Figure 4.5: XP spectra of the microfabricated film electrode: a) wide scan of the entire range; b) $La(3d)$ spectrum; c) $Ni(2p)$ spectrum; d) $Al(2p)$ spectrum.

in contact with the electrolyte. Initially, we perform a few cycles at a scan rate of $v = 10\, mV s^{-1}$ to condition the electrode surface prior to recording the actual CV data points. On average, around 15 cycles are required to obtain steady and reproducible CVs for the film electrodes. Depending on the scan rate, rather different CVs can be observed. Figure 4.6(a) shows a CV at a low scan rate of $v = 200\, \mu V s^{-1}$ and for a potential window ranging from -1.2 to $-0.55\, V$. We choose the limit of the potential window to be $-1.2\, V$ in order to avoid excessive hydrogen evolution due to the Heyrovsky reaction which is discussed in conjunction with the higher scan rates below. Essentially, two redox peaks are observed. We do not observe more peaks at higher anodic switching potentials for the slow scan rate contrary to the fast scan rates as discussed below. We find a broad anodic peak at a potential of around $-0.8\,V$ with an anodic peak current density j_{pa} of around $6 \times 10^{-5} A\,cm^{-2}$. The cathodic peak appears "tail-like" and is shifted to higher reduction potentials while the cathodic current densities j_{pc} continuously increase to a maximum of around $-0.45 \times 10^{-3} A\,cm^{-2}$ at the switching potential.

Generally, the anodic current represents the discharge process where the metal hydride releases hydrogen (dehydriding) while the cathodic current represents a charging process (hydriding). That is, the redox peaks result from the electrolytic (de-)hydrogenation at the solid-liquid interface according to the Volmer reaction:

$$M + H_2O + e^- \rightleftharpoons MH_{ads} + OH^-; \qquad E^{0\Theta} = 0.83\,V vs.\,SHE \tag{4.1}$$

in combination with the (de-)hydriding of the solid phase. In other words, the anodic peak at around $-0.8\,V$ indicates that the adsorbed hydrogen is undergone an electro-oxidative desorption. Here, any consumption of adsorbed hydrogen induces the diffusion of bulk hydrogen to the surface where it can be electro-oxidized as well. The broadness of the anodic peak might be attributed to the relatively slow transport of hydrogen from the bulk to the surface [43]. The cathodic current is related to the electro-reduction of water which results in the adsorption of hydrogen on the electrode surface. Most of these adsorbed molecules diffuse into the metal bulk and form the solid solution until the metal hydride is saturated. With respect to the tail-like shape of the reduction peak in Figure 4.6(a), we assume that the electro-reduction of water is not the sole reaction and the Heyrovsky reaction occurs as well.

In contrast, four distinguishable redox peaks at the higher scan rates can be found in Figure 4.6(b). These CVs are obtained at scan rates of $v = 2, 5, 10, 15\,mVs^{-1}$ and

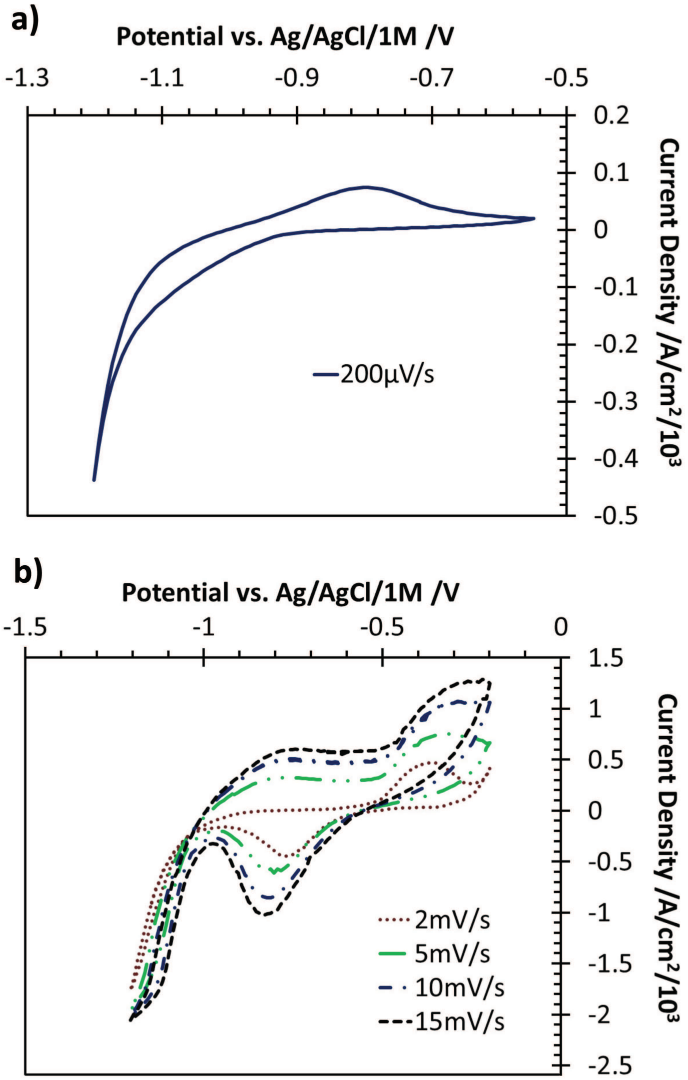

Figure 4.6: Cyclic voltammograms in 1M KOH for intermetallic film electrodes at various scan rates.

a potential window of -1.2 to $-0.2\,V$. Generally, we observe a small and a large oxidation peak at around $-0.8\,V$ and $-0.3\,V$ with the respective peak current densities of roughly $10^{-4}\,A\,cm^{-2}$ and $10^{-3}\,A\,cm^{-2}$. Likewise, we observe a considerable reduction peak at around $-0.8\,V$, with a peak current density on the order of $10^{-3}\,A\,cm^{-2}$, and another “tail-like” peak around $-1.1\,V$ with increasing current densities up to roughly $2 \times 10^{-3}\,A\,cm^{-2}$. We also observe that the peak current density increases as the scan rate increases. We assume that the differences in the CV characteristics for slow and fast scan rates are related to a rather slow bulk diffusion of hydrogen. For fast scan rates, the bulk transfer of hydrogen cannot follow the Volmer reaction (4.1) anymore. Then, the adsorbed hydrogen participates in the following electrochemical and chemical recombination steps resulting in the evolution of hydrogen [44]; i.e., the Heyrovsky reaction

$$MH_{ad} + H_2O + e^- \rightleftharpoons H_2 + OH^- + M \tag{4.2}$$

and the Tafel reaction

$$2MH_{ad} \rightleftharpoons H_2 + 2M \tag{4.3}$$

That is, during sweeping to higher reduction potentials, the absorption rate of adsorbed hydrogen is limited so that the adsorbed hydrogens desorb and recombine according to the Tafel reaction (4.3). This creates free metal surface sites and more water can be electro-reduced via the Volmer reaction (4.1). We assume that this explains the large cathodic peak at around $-0.8\,V$. The other cathodic “tail-like” peak at a potential of $-1.1\,V$ is a result of Heyrovsky reaction where adsorbed hydrogen is also electro-reduced to molecular hydrogen.

During the sweep towards higher oxidation potentials, the small oxidation peak at $0.8\,V$ should be related to the electro-oxidation of adsorbed hydrogen according to the Volmer reaction (4.1). Since this reaction is limited by the bulk transfer of hydrogen to the surface, the dissolved molecular hydrogen, which is still present at the electrode surface, is oxidized at the higher oxidation potential of $-0.3\,V$and adsorbs on the metal surface. The adsorbed hydrogen is then converted back into molecular hydrogen via the Tafel reaction (4.3).

Galvanostatic charging and discharging characteristics

In this section, we examine charge and discharge characteristics of the metal hydride (MH) film electrode which is especially important for microbattery applications. During our experiments, we realize that the durability of the film electrodes greatly depends on the maximum state of charge (SOC). This is probably related to the uptake/release of hydrogen that expands/shrinks the lattice of the metal which induces internal stresses in the bulk along with stresses at the interface of nickel current collector and deposited films. Interestingly, Willems and Buschow have noted that the hydrogen uptake/release in the metal alloys causes both expansion and shrinkage of the lattice while this mechanical stress may lead to a peristaltic transport of lanthanum to the surface. They also mention that the volume expansion of $LaNi_5$ during hydriding can be around 24% [45]. Hence, we are not able to reliably measure the maximum possible hydrogen content of the film electrodes which is related to the fabrication method; i.e., sputtered film electrodes without any binders which can mitigate mechanical stresses. However, the electrochemical hydrogenation of films is very similar to that of powder ones if the materials are crystalline in structure with identical composition [34]. Additionally, since the hydrogen content in the metal alloy is proportional to the number of hydrogen atoms present in the metal interstitial sites (usually six in the case of AB_5–type materials, i.e., $LaNi_{5-x}Al_xH_6$), it can be inferred that, despite the difference in fabrication, we can use capacity values reported in the literature. Wang et al. have reported a maximum discharge capacity of about $220\,mAhg^{-1}$ for a sputtered $4.2\,\mu m$ $LaNi_{4.25}Al_{0.75}$ film [34]. To summarize, a charging protocol with an optimized SOC value is required for our MH film electrodes which are deposited on glass substrates. Figure 4.7 illustrates the charge-discharge behavior of the MH electrode once it is subjected to conditioning step where we perform CVs at a scan rate of $v = 10\,mVs^{-1}$. Typically, the electrodes are preconditioned after around 40 CV cycles when steady and reproducible patterns are obtained.

Initially, we obtain a total number of 4 reliable charge-discharge cycles recorded at a current and current density of $0.1\,mA$ ($0.04\,mA\,cm^{-2}$) for $120\,min$ charge followed by $120\,min$ discharge as shown in Figure 4.7(a). As it can be seen in Figure 4.7(a), the shape of the single charge-discharge cycles is more or less identical but for the first cycle which we attribute to the conditioning step. During the charge process, the potential of the electrode rises to $V_{ch} \approx 0.55\,V$ while a discharge potential of $V_{dis} \approx -1.1\,V$ is obtained. The plateau appears at around $0.25\,V$ in the charging process with a rather upward slope. This step indicates the transition from metal α-phase to hydride β-phase. Likewise, we observe a transition around $-1\,V$ during the discharge.

We further investigate the possibility of obtaining a higher number of reliable charge-discharge cycles by lowering the SOC ($< 25\%$ SOC which corresponds to the capacity of $\leq 50\,mAh\,g^{-1}$). In detail, we show ten reliable charge-discharge cycles recorded at $0.1\,mA$ ($0.04\,mA\,cm^{-2}$) for $45\,min$ charge followed by $45\,min$ discharge in Figure 4.7(b), i.e., SOC of $\approx 10\%$. Note that if we further reduce the SOC by using a shorter charge-discharge duration of $30\,min$ equally (i.e., $30\,min$ charge followed by $30\,min$ discharge), we are able to obtain around 45 stable cycles (results not shown) at

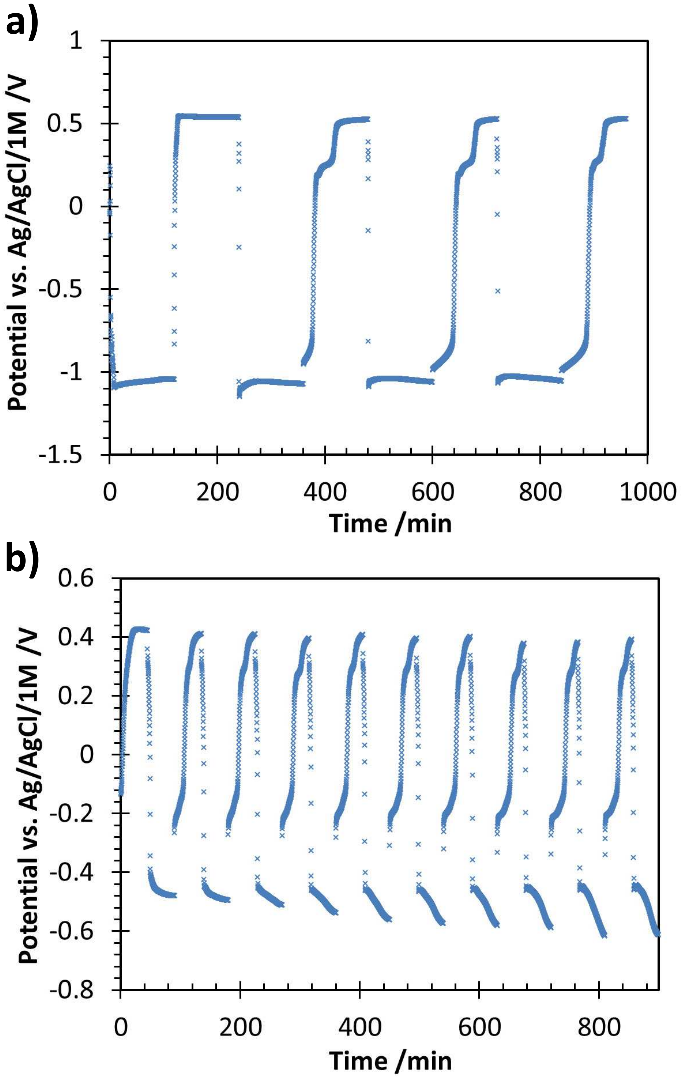

Figure 4.7: Charge–discharge behavior of the MH film electrode at a current of 0.1 mA (at a current density of around $0.04\,mA\,cm^{-2}$): a) high SOC $\approx 25\%$; b) low SOC $\approx 10\%$.

the same current mentioned above. As it can be seen in Figure 4.7(b), the shape of the single charge-discharge cycles is more or less identical but for the first cycle which we again attribute to the conditioning step. For the 10% SOC, during the charge process, the potential of the electrode rises to around $0.44\,V$ while the discharge potential of around $-0.5\,V$ is obtained. Note that the discharge potential increases as more cycles are performed. We observe a plateau at around $0.3\,V$ during the charging process with an upward slope. Additionally, another plateau is found at around $-0.2\,V$ which indicates a multi-plateau transition. This can be attributed to an inherent characteristic of the sputtered film material. The multi-plateau behavior has been found in various metallic compounds such as titanium cobalt TiCo as mentioned in ref.[46]. Overall, we do not observe any (mechanical) degradation of the MH films on glass for this controlled charging-discharging (duration) mechanism for a number of 45 cycles at a SOC of around 7%. Note that the difference in potentials observed for the high SOC (25%) and the low SOC (10%) (in Figure 4.7) can be attributed to the different hydrogen concentrations in the metal. In other words, a higher utilization of materials (i.e., higher hydrogen contents) results in higher potentials of charge and discharge (absolute values).

To summarize, we are able to charge the electrode for around $50\,mAh\,g^{-1}$ ($40\,\mu Ah\,cm^{-2}$ with electrode thickness of $1.1\,\mu m$ and weighted average film density of $8.24\,g\,cm^{-3}$) which is a state of charge (SOC) of $\approx 25\%$ (Figure 4.7(a)). We realize that around 25% SOC, we can use the MH films for a few number of charge-discharge cycles. However, a larger number of charge-discharge cycles can be obtained at a SOC of $7 \sim 10\%$.

Derivation of an electrolytic (de-)hydrogenation rate model

In our previous work ref.[36], we reviewed selected models for the (de-)hydrogenation of hydrogen absorbing metals/alloys. These models are used to describe the P–C–isotherms of the metal hydride materials. Here, Feng et al. suggested a model which is able describe the transition regions assuming that the sorption at the interface is a first-order kinetic reaction [39]. Since gaseous and electrolytic (de-)hydrogenation share many similar reaction steps, we derive the following model which is based on the similar assumptions as the Feng model. The result can be considered as an electrolytic (de-)hydrogenation equivalent of the P–C-isotherm. That is, we can infer the Galvani (equilibrium) potential of the metal hydride electrode as a function of the hydrogen content from charge/discharge measurements which reduces the experimental efforts considerably. Such a correlation is also useful for sensing purposes.

We begin this section with a brief review of the Feng model to emphasize on the similarities. Feng et al. considered that (de)hydriding with a very slow hydrogen sorption rate can be considered as a continuous sequence of equilibrium states. The typical plateau region of the P–C isotherms is controlled by the transition from α- to β-phase and vice versa. In case of dehydriding, there are three reaction steps:

1. Diffusion of hydrogen atoms through the β-phase hydride;
2. Transition of hydrogen from the absorbed sites to the adsorbed sites on the particle surface according to

$$MH_{abs} \underset{k_{-4}}{\overset{k_4}{\rightleftharpoons}} MH_{ads}; \tag{4.4}$$

3. Desorption reaction of hydrogen at the surface similar to the Tafel equation (4.3).

We denote k_i and k_{-i} as the rate constants of the forward and the reverse reaction i, respectively. Reaction (4.3) and (4.4) are considered as the rate-controlling steps and can be modelled by assuming first-order rate reactions according to

$$k_3 C_H (1-\theta) = k_{-3}\theta (C_{max} - C_H) \tag{4.5}$$

and

$$k_4\theta = k_{-4}(1-\theta) P_{eq}^{\frac{y_0-x_0}{2}}, \tag{4.6}$$

where C_H is the bulk hydrogen concentration (in atoms per metal atom), C_{max} is the maximum theoretical hydrogen concentration, θ is the hydrogen coverage on the surface, P_{eq} is the hydrogen equilibrium pressure, and $y_0 - x_0$ is the length of the plateau region. Introducing an Arrhenius-like expression for the rate constants, the kinetic based model arrives at [36, 39]

$$RT \ln\left(\frac{P_{eq}}{P_{ref}}\right) = \frac{2}{y_0 - x_0}\left(A + RT\ln\left(\frac{C_H}{C_m - C_H}\right) + \frac{\gamma^H C_H}{C_m}\right). \tag{4.7}$$

Here, P_{ref} ($\equiv 1\,atm$) is the reference pressure; T is the absolute temperature; R is the universal gas constant; γ^H is the attractive interaction coefficient of H–H absorbed; and the parameter A is a function of the enthalpy of hydrogen sorption, the temperature and the frequency factors of the rate constants. The left-hand side of the equation is similar to the Gibbs–Helmholtz equation; i.e., $\Delta G \approx RT\ln\left(\frac{P}{P_0}\right)$. We fit the data of the desorption P-C isotherms in Figure 4.2 to Eq.(4.7) and obtain the average values for the absolute Gibbs energy, enthalpy and entropy of reaction to be $|\Delta G| = 4.14\,kJ\,(mol\,H_2)^{-1}$, $|\Delta H| = 31.5\,kJ\,(mol\,H_2)^{-1}$ and $|\Delta S| = 113.5\,J\,(mol\,K)^{-1}$, respectively.

Likewise to the gaseous hydrogen sorption, the electrolytic (de-)hydrogenation occurs in three consecutive steps. Here, step (4.3) and (4.4) are identical for both processes but the last step differs. That is, in case of an electrolytic (de)hydrogenation, the Volmer reaction (4.1) takes place. The following approach is inspired by the work of Yang et al. who modelled the anodic overpotential of hydride electrodes for considerable discharge currents; i.e., for large overpotentials which allow for linearization of the exponential functions [47]. We use parts of this model to describe the electrode potential as a function of the hydrogen concentration in the electrode. In detail, if the current is small, the electrochemical reaction, the hydrogen sorption at the surface and the hydrogen bulk diffusion are in a steady state; an assumption similar to the Feng model. Note that a comparable approach, also based on the work of Yang et al., was reported in ref.[37]. The authors assumed that the charging electrode potential is similar to the Galvani potential. In contrast, we account for irreversibilities/overpotentials which allow to infer the "real" Galvani potential φ_0. On the one hand, even for zero currents, equilibrium is usually not achieved due to parasitic reactions or sluggish kinetics; these losses are captured by the equilibrium overpotential η_{eq}. On the other hand, even the smallest net current requires the activation overpotential η_{act} to be overcome. Hence, the electrode potential for small currents can be written as $\varphi = \varphi_0 + \eta_{eq} + \eta_{act}$. To obtain an expression for the Galvani potential, we employ Eq.(4.5) while the electrolytic (de)hydrogenation (Volmer) rate equations in case of equilibrium can be written as

$$k_1 c_{OH^-} \theta \exp\left(\frac{\beta F \varphi_0}{RT}\right) = k_{-1} c_{H_2O} (1-\theta) \exp\left(\frac{(1-\beta) F \varphi_0}{RT}\right). \tag{4.8}$$

Inserting Eq.(4.8) in Eq.(4.5) to obtain, after some rearrangements

$$\varphi_0 = \frac{RT}{F}\left[\ln\left(\frac{k_{-3} k_{-1} c_{H_2O}}{k_3 k_1 c_{OH^-}}\right) + \ln\left(\frac{C_H}{C_{max} - C_H}\right)\right], \tag{4.9}$$

where c_{H_2O}, c_{OH^-} are the concentrations of water and hydroxide in the solution, respectively; F is the Faraday constant; R is the universal gas constant, T is the absolute temperature; and β is the symmetry factor. The Tafel equation $\eta = A_T + B_T \ln\left(\frac{|j|}{j^{\ominus}}\right)$ can be used to infer a correlation for the equilibrium overpotential. At equilibrium state, the current density j is zero so that we cancel the corresponding term and the equilibrium overpotential corresponds to the Tafel intercept:

$$\eta_{eq} \approx A_T\left(j_0\right), \tag{4.10}$$

which is still a function of the exchange current density j_0. The final definition of the equilibrium overpotential depends on whether a reduction or an oxidation reaction occurs. The activation overpotential is considered using the linearized Butler-Volmer equation $j \approx j_0 \frac{F}{RT}\eta$; it is

$$\eta_{act} \approx \frac{RT}{F}\frac{|j|}{j_0}. \tag{4.11}$$

Hence, based on Eqs.(4.9-4.11), the electrode potential for a small current can be written as

$$\varphi = \varphi_0 + \eta_{eq} + \eta_{act} \approx \frac{RT}{F}\left[\ln\left(\frac{k_{-1}k_{-3}c_{H_2O}}{k_1 k_3 c_{OH^-}}\right) + \ln\left(\frac{C_H}{C_{max} - C_H}\right) + \frac{|j|}{j_0}\right] + A_T\left(j_0\right) \tag{4.12}$$

The final form of Eq.(4.12) depends on whether a cathodic or an anodic reaction occurs. Furthermore, the exchange current density j_0 also depends on the hydrogen concentration of the electrode [47]; a respective correlation is not readily available.

In the following, we formulate the electrode potential for a reduction reaction with charging current j_c. Hence, the Tafel intercept becomes $A_T = -\frac{RT}{\beta F} \ln\left(\frac{j_0}{j^{\Theta}}\right)$ where β and $j^{\Theta} \equiv 1A\,m^{-2}$ are the symmetry factor and the standard current density, respectively. We further assume that the correlation of exchange current density-hydrogen concentration can be approximated by $j_0 \sim \left(\varepsilon_0 {C_H}^n\right)^{\beta} j^{\Theta}$ and that the symmetry factor β is similar to 0.5. Based on this, the electrode potential in Eq.(4.12) can be rewritten in terms of hydrogen concentration as

$$\varphi \approx \frac{RT}{F}\left[A_1 + \ln\left(\frac{{C_H}^{1-n}}{\varepsilon_0(C_{max} - C_H)}\right) - \frac{1}{\sqrt{\varepsilon_0 {C_H}^n}}\frac{|j_c|}{j^{\Theta}}\right] \tag{4.13}$$

where we group the reaction parameters according to $A_1 = \ln\left(\frac{k_{-1}k_{-3}c_{H_2O}}{k_1 k_3 c_{OH^-}}\right)$ and consider the A_1, ε_0, n as regression parameters. Note that this correlation can also be used for an anodic reaction due to the value of the symmetry factor.

Finally, we use Eq.(4.13) to infer the equilibrium potential depending on the hydrogen concentration based on the hydrogenation process of the metal electrode with a low charging current. In detail, we use the second cycle of the charge-discharge plot (Figure 4.7(a)) and first correlate the specific charge content and the hydrogen concentration based on

$$C_H\left(\frac{H}{M}\right) = \frac{3.6\,W\,Q}{F} \tag{4.14}$$

as shown in Figure 4.8. Here, Q is the specific capacity of the metal hydride alloy in $mAh\,g^{-1}$ and W is molecular weight of the alloy. A weighted average method is used to estimate the density and the molecular weight values of the MH film electrode.

We perform a regression of Eq.(4.13) to the so-plotted experimental results

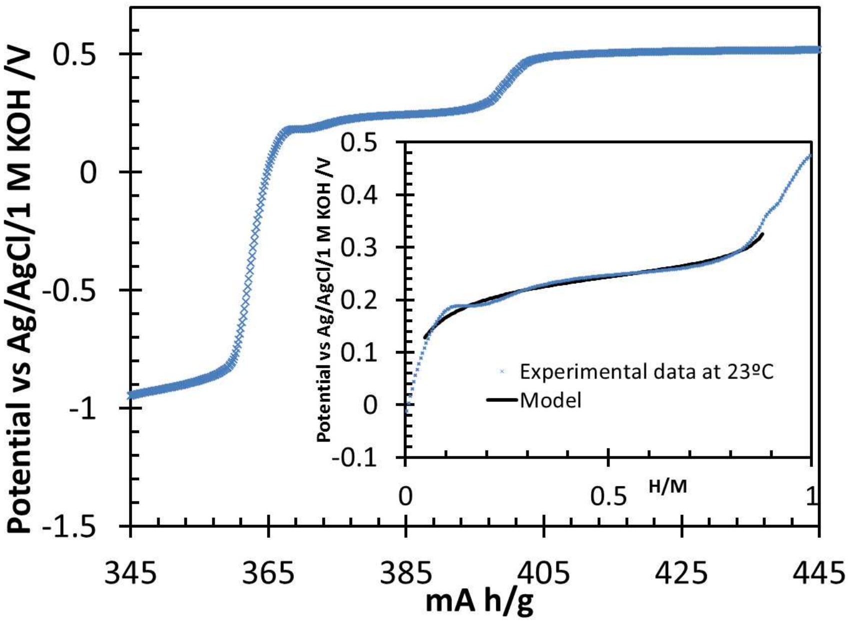

Figure 4.8: Electrode potential versus specific capacity of the MH film electrode. The insert gives a comparison of the Kinetic model and the experimental data.

by using the minimization of the sum of the squared residuals. We compute the model parameters by employing the Generalized-Reduced-Gradient (GRG) technique for nonlinear optimizations. In detail, the regression results in $A_1 = 8.123, \varepsilon_0 = 0.012, n = -1.387$ at a temperature of $296K$. As it can be seen in Figure 4.8, our model (solid line in the insert) is able to describe the experimental data relatively well in all regions. The model accounts for the non-ideality of the plateau region – i.e., for a plateau with a slope – and offers a smooth transition between the different regions of the plot. The model does not describe the outer boundaries of the $\alpha-$ and $\beta-$ regions; i.e., $C_H = 1$ and $C_H = 0$ since the C_{max} is taken to be 0.9 and values larger than C_{max} have a negative argument in the logarithm in Eq.(4.13). The equilibrium potential with respect to the

Ag/AgCl in 3M KCl reference electrode is then obtained from $\varphi_0 = \varphi - \eta_{eq} - \eta_{act}$ to be

$$\varphi_0 \approx A_1 \frac{RT}{F} + \frac{RT}{F} \ln\left(\frac{C_H}{C_{max} - C_H}\right) = 0.207V + 0.026V \ln\left(\frac{C_H}{C_{max} - C_H}\right). \quad (4.15)$$

Here, the similarity to the Nernst equation is right away obvious. The first term can be considered as the standard-like potential while the second term is a correction for the concentrations. After relating the values to SHE and using $\Delta G = -F\varphi_0$, we obtain the Gibbs energy of the entire hydrogenation process for a concentration of $C_H = 0.5$ to be around $1\,kJ\,(mol\,H_2)^{-1}$. This value is on the same order as the Gibbs energy of the entire gaseous sorption process.

The effect of electrolyte concentration on cyclic voltammograms

In this section, we discuss our CV results which are obtained by varying the electrolyte concentration (KOH) to give insights into the performance of the MH film electrodes. The motivation is that a highly-concentrated electrolyte may degrade the compounds of the microbattery and also presents a safety issue in case of leakage. We would like to infer whether the battery can be operated with relatively low electrolyte concentrations. Therefore, we perform cyclic voltammetry on the MH film electrodes at KOH concentrations of $1M$, $0.75M$, $0.5M$, $0.25M$, and $0.125M$ at a scan rate of $200\,\mu V s^{-1}$ as illustrated in Figure 4.9.

Generally, we observe that the anodic peaks are shifted to higher oxidation potentials. Interestingly, the cathodic potentials are shifted to lower reduction potentials. It is found that, at KOH electrolyte concentrations of $0.25M$ and $0.125M$, the cathodic peak can be differentiated to some extent from the tail of the CV. This is not the case for higher KOH concentrations, though. Thermodynamically, a lower KOH

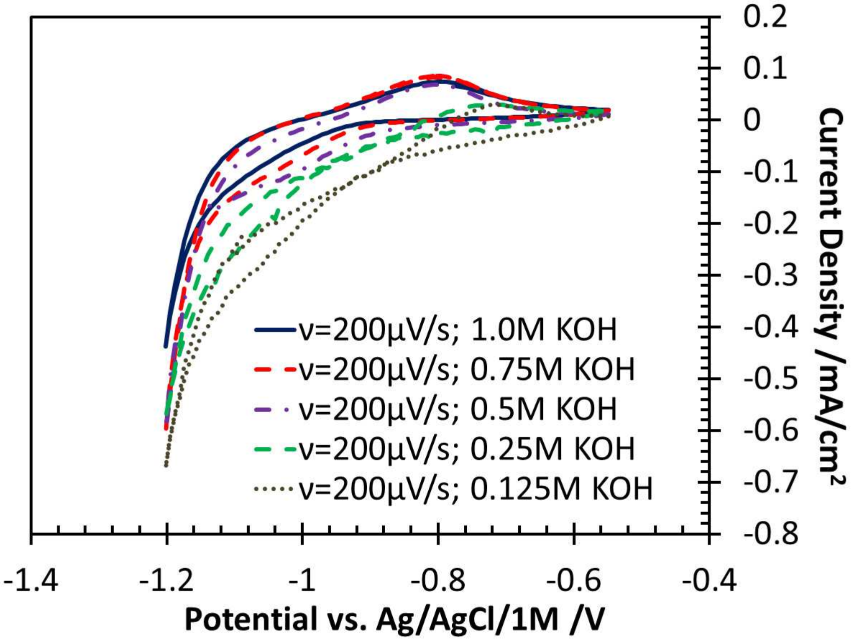

Figure 4.9: Cyclic Voltammograms for MH film electrode at various KOH electrolyte concentrations at a scan rate of $200\,\mu V s^{-1}$.

concentration shifts the equilibrium potential of the Volmer equation towards the reduction reaction. It is also understood that less-concentrated electrolytes (with lower conductivities) increase the ohmic overpotential. Hence, the shift to the higher oxidation potentials can be attributed to the shift towards the reduction reaction and to a higher ohmic overpotential within a less-concentrated electrolyte. However, the estimated IR-drop due to concentration variation ranges between $I_{min}R_{min} \approx 2.09 \times 10^{-3}$ and $I_{max}R_{max} \approx 20\,mV$, therefore, the contribution of the concentration (ohmic overpotential) on the potential shifts seems relatively small with respect to the potential shifts at electrolyte concentrations of $0.25M$ and $0.125M$ which are around $\approx 100\,mV$. The situation is different for the cathodic reactions as can be seen in the CVs. It appears that the improvement of the reduction of water occurs at $\approx -1.05\,V$ (i.e., a potential shift of around $150\,mV$), a higher measure than the negative influence of the electrolyte resistance. Overall, the performance of the MH film electrode, in terms of hydrogen oxidation-reduction, deteriorates significantly at KOH electrolyte concentrations of $\leq 0.5M$.

4.5 Concluding Remarks

This work is concerned with the microfabrication of metal hydride film electrodes on glass substrates which can be utilized in various applications such as rechargeable nickel metal hydride batteries. Furthermore, since these electrodes are fabricated by commonly-used microfabrication techniques and on a common substrate for micro electro mechanical devices, they can be easily integrated during the regular manufacturing processes. We conclude this article with the following remarks:

1) In this work, an electron beam evaporation technique is utilized to create a thin layer of nickel as a current collector of the electrode. We microfabricate an AB_5-type intermetallic film on a glass (silica) substrate using a DC magnetron sputtering method.

2) The film electrode materials are characterized by employing Energy Dispersive Spectroscopy and X-ray Photoelectron Spectroscopy methods. The results are in good agreement with the characteristics of the materials which are utilized in macroscale fabricated electrodes. The electrochemical performance is tested by comparing cyclic voltammograms of the microfabricated electrodes. In general, we observe a good performance with respect to the application as electrode in microscale systems fabricated on glass. As for the mechanical stability during charge-discharge cycling, we obtain good durability; however, this depends on the chosen state of charge (SOC). Even

though we obtain around 45 stable charge-discharge cycles at lower SOC due to lower utilization of the electro-active materials, further investigation is required to improve the mechanical stability of the film electrodes at higher SOCs. One possibility would be to use a pattering technique similar to the one we previously reported in ref.[48].

3) Finally, we derive a kinetic model which allows to infer the equilibrium potential from the electrolytic (de)hydrogenation at low currents. The model reduces the experimental costs considerably since only a single measurements is required and can be used, beside as a measure for electrochemical characterization, for hydrogen sensing applications.

4.6 Acknowledgments

The authors gratefully acknowledge the financial support from Queen's University, the Natural Sciences and Engineering Research Council of Canada (NSERC), and CMC microsystems. We also thank the personnel of Microelectronics Fabrication Laboratory (MFL) at Carleton University, Ottawa, Canada, for assistance with the DC magnetron sputter instrument. Thank you to Karl Murray, undergraduate student at Queen's University, for performing gaseous hydrogen sorption experiments for materials testing.

4.7 Nomenclature

a	Lattice parameter [-]
A	Regression parameter
c	Lattice parameter [-]
C_H	Hydrogen concentration [atoms per metal atom]
C_{max}	Maximum hydrogen concentration [atoms per metal atom]
E	Potential [V]
F	Faraday constant
I	Current [A]
j_0	Exchange current density [$A\,cm^{-2}$]
j	Current density [$A\,cm^{-2}$]
k	Reaction rate constant
n	Regression parameter [-]
P	Pressure [Pa]
Q	Specific capacity [$mAh\,g^{-1}$]
R	Universal gas constant [$L\ atm\ K^{-1}\ mol^{-1}$]
T	Temperature (Absolute) [$^\circ C$ and (K)]
v	Scan rate [$V\ s^{-1}$]
W	Molar mass [$g\,mol^{-1}$]
$y_0 - x_0$	Regression parameter
β	Symmetry factor [-]
γ^H	Absorbed hydrogen-hydrogen attractive interaction [$kJ\,(mol\,H_2)^{-1}$]
ΔG	Gibbs energy [$kJ\,(mol\,H_2)^{-1}$]
ΔH	Enthalpy energy [$kJ\,(mol\,H_2)^{-1}$]
ΔS	Entropy [$J\,(K\,mol\,H_2)^{-1}$]
ε	Regression parameter [-]
θ	Hydrogen coverage on the surface [-]
φ	Galvani potential [V]
η	Overpotential [V]

4.8 References

[1] Klavs F. Jensen. Microreaction engineering – is small better? *Chem. Eng. Sci.*, 56(2):293 – 303, 2001.

[2] P Abgrall and A-M Gué. Lab-on-chip technologies: making a microfluidic network and coupling it into a complete microsystem–a review. *J. Micromech. Microeng.*, 17(5):R15, 2007.

[3] Luc Gervais, Nico De Rooij, and Emmanuel Delamarche. Microfluidic chips for point-of-care immunodiagnostics. *Adv. Mater.*, 23(24):H151–H176, 2011.

[4] L. Zhu, D. Kim, H. Kim, R.I. Masel, and M.A. Shannon. Hydrogen generation from hydrides in millimeter scale reactors for micro proton exchange membrane fuel cell applications. *J. Power Sources*, 185(2):1334 – 1339, 2008.

[5] K A Cook-Chennault, N Thambi, and A M Sastry. Powering MEMS portable devices–a review of non-regenerative and regenerative power supply systems with special emphasis on piezoelectric energy harvesting systems. *Smart Mater. Struct.*, 17(4):043001, 2008.

[6] Yang Yang and Jing Liu. Micro/nanofluidics-enabled energy conversion and its implemented devices. *Front. Energy*, 5(3):270–287, 2011.

[7] Erik Kjeang, Ned Djilali, and David Sinton. Microfluidic fuel cells: A review. *J. Power Sources*, 186(2):353–369, 2009.

[8] C C Ho, J W Evans, and P K Wright. Direct write dispenser printing of a zinc microbattery with an ionic liquid gel electrolyte. *J. Micromech. Microeng.*, 20(10):104009, 2010.

[9] JFM Oudenhoven, RJM Vullers, and R Schaijk. A review of the present situation and future developments of micro-batteries for wireless autonomous sensor systems. *Int. J. Energy Res.*, 36(12):1139–1150, 2012.

[10] XL Wang and S Suda. Reaction kinetics of hydrogen-metal hydride systems. *Int. J. Hydrogen Energy*, 15(8):569 – 577, 1990.

[11] F Feng, M Geng, and Derek O. Northwood. Electrochemical behaviour of intermetallic-based metal hydrides used in Ni/metal hydride (MH) batteries: A review. *Int. J. Hydrogen Energy*, 26(7):725 – 734, 2001.

[12] H Bjurström, Y Komazaki, and S Suda. The dynamics of hydrogen transfer in a metal hydride heat pump. *J. Less-Common Met.*, 131(1-2):225 – 234, 1987.

[13] J Payá, M Linder, R Mertz, and JM Corberan. Analysis and optimization of a metal hydride cooling system. *Int. J. Hydrogen Energy*, 36(1):920 – 930, 2011.

[14] L Schlapbach and A Züttel. Hydrogen-storage materials for mobile applications. *Nature*, 414(6861):353–358, 2001.

[15] KS Nahm, WY Kim, SP Hong, and WY Lee. The reaction kinetics of hydrogen storage in $LaNi_5$. *Int. J. Hydrogen Energy*, 17(5):333 – 338, 1992.

[16] F. Meli, A. Zuettel, and L. Schlapbach. Surface and bulk properties of $LaNi_{5-x}Si_x$ alloys from the viewpoint of battery applications. *J. Alloys Compd.*, 190(1):17 – 24, 1992.

[17] Kohta Asano, Yoshiji Hashimoto, Takahiro Iida, Masayuki Kondo, and Yoshiaki Iijima. Hydrogen diffusion by substitution of aluminum and cobalt for a part of nickel in $LaNi_5$-H alloy. *J. Alloys Compd.*, 395(12):201 – 208, 2005.

[18] J.J. Reilly, G.D. Adzic, J.R. Johnson, T. Vogt, S. Mukerjee, and J. McBreen. The correlation between composition and electrochemical properties of metal hydride electrodes. *J. Alloys Compd.*, 293295(0):569 – 582, 1999.

[19] R. Baddour-Hadjean, H. Mathlouthi, J.P. Pereira-Ramos, J. Lamloumi, M. Latroche, and A. Percheron-Gugan. An electrochemical study of mono-substituted intermetallic hydrides. *J. Alloys Compd.*, 356-357(0):750 – 754, 2003.

[20] Tetsuo Sakai, Keisuke Oguro, Hiroshi Miyamura, Nobuhiro Kuriyama, Akihiko Kato, Hiroshi Ishikawa, and Chiaki Iwakura. Some factors affecting the cycle lives of $LaNi_5$-based alloy electrodes of hydrogen batteries. *J. Less-Common Met.*, 161(2):193 – 202, 1990.

[21] Jun Liu, Yifu Yang, Peng Yu, Yan Li, and Huixia Shao. Electrochemical characterization of $LaNi_{5-x}Al_{x(x=0.1-0.5)}$ in the absence of additives. *J. Power Sources*, 161(2):1435 – 1442, 2006.

[22] Tetsuo Sakai, Hiroshi Miyamura, Nobuhiro Kuriyama, Akihiko Kato, Keisuke Oguro, Hiroshi Ishikawa, and Chiaki Iwakura. The influence of small amounts of added elements on various anode performance characteristics for $LaNi_{2.5}Co_{2.5}$-based alloys. *J. Less-Common Met.*, 159(0):127 – 139, 1990.

[23] MH Mendelsohn, DM Gruen, and AE Dwight. The effect of aluminum additions on the structural and hydrogen absorption properties of AB_5 alloys with particular reference to the $LaNi_{5-x}Al_x$ ternary alloy system. *J. Less-Common Met.*, 63(2):193–207, 1979.

[24] Gary Sandrock. A panoramic overview of hydrogen storage alloys from a gas reaction point of view. *J. Alloys Compd.*, 293295(0):877 – 888, 1999.

[25] Xi Shan, Joe H. Payer, and Jesse S. Wainright. Increased performance of hydrogen storage by Pd-treated $LaNi_{4.7}Al_{0.3}$, $CaNi_5$ and Mg_2Ni. *J. Alloys Compd.*, 426(12):400 – 407, 2006.

[26] A Merzouki, C Cachet-Vivier, V Vivierb, JY Nedelec, LT Yu, N Haddaoui, JM Joubert, and A Percheron-Gueganc. Microelectrochemistry study of metal-hydride battery materials: Cycling behavior of $LaNi_{3.55}Mn_{0.4}Al_{0.3}Co_{0.75}$ compared with $LaNi_5$ and its mono-substituted derivatives. *J. Power Sources*, 109(2):281 – 286, 2002.

[27] H. Okuno and Y. Sakurai. Electrical conduction in amorphous Gd-Co films. *J. Appl. Phys.*, 53(11):8245–8247, 1982.

[28] D.M. Mattox. Fundamentals of ion plating. *J. Vac. Sci. Technol.*, 10(1):47–52, Jan 1973.

[29] Gin-Ya Adachi, Ken-Ichi Niki, and Jiro Shiokawa. The effect of hydrogen absorption on the electrical resistivity of $LaNi_5$ film. *J. Less-Common Met.*, 81(2):345 – 348, 1981.

[30] G. Adachi, H. Sakaguchi, K. Niki, N. Nagai, and J. Shimokawa. Preparation of $LaNi_5$ films and their electrical properties under a hydrogen atmosphere. *J. Less-Common Met.*, 108(1):107 – 114, 1985.

[31] L. Huang, H. Gong, and W. Gao. Phase change of sputtered $LaNi_5$ thin films due to hydrogenation. *Thin Solid Films*, 339(12):78 – 81, 1999.

[32] L Smardz, K Smardz, M Nowak, and M Jurczyk. XPS studies of nanocrystalline and polycrystalline $LaNi_5$ thin films. *Mol. Phys.*, 38:118–123, 2003.

[33] H. Sakaguchi, N. Taniguchi, H. Seri, J. Shiokawa, and G. Adachi. Mechanical properties of $LaNi_5$ thin films prepared by sputtering and vapor deposition methods and determination of the hydrogen content in these films. *J. Appl. Phys.*, 64(2):888–892, 1988.

[34] ZM Wang, Chi Ying Vanessa Li, Huaiying Zhou, Shi Liu, and SLI Chan. Electrochemical hydrogen storage in $LaNi_{4.25}Al_{0.75}$ alloys: A comparative study between film and powder materials. *Mater. Charact.*, 59(4):468–472, 2008.

[35] JHN Van Vucht, FAr Kuijpers, and HCAM Bruning. Reversible room-temperature absorption of large quantities of hydrogen by intermetallic compounds. *Philips Res. Rep. 25: 133-40*, 1970.

[36] H Falahati and DPJ. Barz. Evaluation of hydrogen sorption models for $LaNi_5$-type metal alloys by employing a gravimetric technique. *Int. J. Hydrogen Energy*, 38(21):8838 – 8851, 2013.

[37] Feng Feng, Xinyi Ping, Ziqiang Zhou, Mingming Geng, Jianwen Han, and Derek O. Northwood. The relationship between equilibrium potential during discharge and hydrogen concentration in a metal hydride electrode. *Int. J. Hydrogen Energy*, 23(7):599 – 602, 1998.

[38] N. Furukawa. Development and commercialization of nickel-metal hydride secondary batteries. *J. Power Sources*, 51(12):45 – 59, 1994.

[39] F. Feng, M. Geng, and Derek O. Northwood. Mathematical model for the plateau region of P-C-isotherms of hydrogen-absorbing alloys using hydrogen reaction kinetics. *Computational Materials Science*, 23(14):291 – 299, 2002.

[40] Jun Liu, Yifu Yang, Yan Li, Peng Yu, Yonghao He, and Huixiao Shao. Comparative study of by powder microelectrode technique. *Int. J. Hydrogen Energy*, 32(12):1905 – 1910, 2007.

[41] Elki C. Souza and Edson A. Ticianelli. Effect of partial substitution of nickel by tin, aluminum, manganese and palladium on the properties of $LaNi_5$-type metal hydride alloys. *J. Braz. Chem. Soc.*, 14:544 – 550, 08 2003.

[42] L. Schlapbach, A. Seiler, F. Stucki, and H.C. Siegmann. Surface effects and the formation of metal hydrides. *J. Less-Common Met.*, 73(1):145 – 160, 1980.

[43] Tohru Kitamura, Chiaki Iwakura, and Hideo Tamura. Comparative study of $LaNi_5$-type alloy electrodes with and without Pd-plated layer by means of cyclic voltammetry. *Electrochimica Acta*, 27(12):1729 – 1731, 1982.

[44] J Kleperis, G Wójcik, A Czerwinski, Jm Skowronski, M Kopczyk, and M Beltowska-Brzezinska. Electrochemical behavior of metal hydrides. *J. Solid State Electrochem.*, 5(4):229–249, 2001.

[45] J.J.G. Willems and K.H.J. Buschow. From permanent magnets to rechargeable hydride electrodes. *J. Less-Common Met.*, 129(0):13 – 30, 1987.

[46] F. Cuevas, J.-M. Joubert, M. Latroche, and A. Percheron-Guagan. Intermetallic compounds as negative electrodes of Ni/MH batteries. *Appl. Phys. A*, 72(2):225–238, 2001.

[47] QM Yang, M Ciureanu, DH Ryan, and JO Ström-Olsen. Hydrogen surface concentration and overpotential for galvanostatic discharge of hydride electrodes i. development of the model. *J. Electrochem. Soc.*, 141(8):2108–2112, 1994.

[48] H Falahati, E Kim, and D.P.J. Barz. Fabrication and characterization of thin-film nickel hydroxide electrodes for micro-power applications. *Accepted for publication in ACS Applied Materials & Interfaces, 22/05/2015*, 2015.

Chapter 5

A Nickel/Metal Hydride Microbattery for Microfluidic Applications[1]

5.1 Abstract

The utilization of micropower sources is of great interest especially in portable microfluidic devices where only low power densities and energy contents are required. In the present work, we report on a rechargeable microbattery which can be integrated into microfluidic and other Micro Electro Mechanical Systems devices. In detail, the microbattery is based on a nickel/metal hydride chemistry and is integrated on the typical microfluidic glass substrate. Galvanostatic charge-discharge and voltage-current measurements are performed in order to evaluate the electrochemical performance of the microbattery. We also give insights into the durability

---

[1] To be submitted for publication

of the microbattery electrodes based on electrochemical impedance spectroscopy.

5.2 Introduction

The increasing utilization of portable and wearable microdevices has resulted in a demand for microscale power supplies which are directly integrated in microdevices during the manufacturing process. Microdevices which can benefit from such on-board integrated power sources include micro-electro-mechanical-systems (MEMS) [1], microfluidic systems such as micro-total-analysis-systems (μTAS) [2], Lab-on-a-Chip (LOC) [3], and Point-of-Care-Testing (POCT) devices [4].

There have been various devices and technologies reported with different power requirements. For instance, Humble et al. have suggested power requirements for standby and data collection/processing activities in the range of 3 to 30 μW and 100 to 1000 μW, respectively [5]. Puers and Wouters have mentioned a flexible temperature and motion sensing device based on electronic interface circuits with a low power consumption of 35 μW [6]. Further MEMS wireless sensors with ultra-low-power requirements of around 0.5 μW are reported for health monitoring systems in refs.[7, 8]. In terms of medical applications, a power requirement of smaller than 10 μW for cardioverter-defibrillator while a range of 100 to 2000 μW are reported for hearing aids in ref.[9].

In terms of capacity requirements, if we assume an operation time of around $4\,hr\,day^{-1}$ for the wireless sensor node reported for health monitoring system by Okada et al.[8, 7] as mentioned above, a capacity of $\approx 1.7\,\mu Ah$ per day ($\approx 50\,\mu Ah$ per month) at a nominal voltage of $1.2\,V$ is required. This capacity is adequate for the sensor to perform the measurement every minute for a duration of 10 seconds.

Amongst various types of power sources which are potential candidates for this task, batteries offer simplicity as they do not require continuous supply of reactants or materials. Additionally, a vast amount of technical knowledge is readily available from conventional battery systems. A short review on advances in microbatteries is available by Albano et al. in ref.[10], however, this source only covers the years between 1995 and 2007.

Generally, we can categorize batteries into solid state and liquid (aqueous) electrolyte cells. Aqueous electrolyte batteries have some advantages due to their relatively low costs, high ionic conductivity (lower ohmic overpotentials), better safety, and less environmental issues [11, 12]. Among microbatteries reported in the literature, lithium-(refs.[13, 14]), nickel- (refs.[5, 15]), and zinc- (refs.[10, 16]) based batteries have gained attention for application in microscale devices. Pikul et al. reported a high power density lithium microbattery which provides power densities for up to $74\,W\,cm^{-3}$ [17]. While lithium-based microbatteries provide high power densities, a lithium-based microbattery requires an electronic circuit to maintain a certain potential range to avoid thermal runaway and high variations in the cell potential if over(dis-)charged [18]. This leads to more complexity especially when microscale devices are concerned and complications may arise in cell encapsulations due to high reactivity of the lithium when it is exposed to moist. Despite these difficulties, a large number of recent works is related to lithium-based microbatteries due to their high energy content and better cyclability.

A nickel-zinc microbattery was introduced by Humble et al. fabricated on a epoxy-coated silicon substrate which delivers energy densities of $0.555\,mWh\,cm^{-2}$ [5]. One of the concerns with respect to nickel-zinc microbatteries is the possibility of morphology change of the zinc electrode after several charge-discharge cycles. A three dimensional primary zinc-air microbattery with a micromachined metallic scaffold which can deliver an energy density of around $3\,mWh\,cm^{-2}$ was reported in ref.[19]. Albano et al. reported an integrated zinc-silver oxide primary microbattery for implantable MEMS devices which delivers around $138\,\mu Ah\,cm^{-2}$ [10]. They fabricated the cathode (silver-oxide) on a glass substrate (titanium and gold were used as adhesion and current collector layers, respectively) using physical vapor deposition while the anode (zinc) was directly sprayed on a copper foil from a nanopowder zinc solution [10]. In addition, Ho et al. reported on a novel ink jet printing technique to fabricate zinc-silver microbatteries directly onto a substrate which delivers 2.3 and $3.9\,mWh\,cm^{-2}$ for two and three dimensional-type electrode microbatteries, respectively [20, 21].

Among the microbatteries reported in the literature over the last decades, there is almost no attempt to utilize a nickel metal hydride (NiMH) chemistry. Even though the NiMH cell does not provide as high energy density as a lithium-based cell, it does not suffer from morphology change at the electrode surface as that of zinc electrode in a nickel-zinc cell, for instance. We are not aware of a systematic preparation and characterization of a NiMH microbattery which is fabricated by using microfabrication techniques. However, Do et al. reported a NiMH battery fabricated using a thick film electrode approach where they screen-printed the electrodes using a binder (polyvinyl alcohol) onto the sides of a porous ceramic substrate as a separator (and support) of the electrodes while the current collectors were deposited using a sputtering technique [22, 23]. They reported specific discharge capacities of $1.2\,\text{to}\,3.2\,mAh\,cm^{-2}$ [22]. The question arises whether such a screen printing porous media-based approach can be easily integrated into the regular microfabrication process. In terms of microbattery architectures, two different approaches have been employed to design and fabricate the electrodes; i.e., two dimensional (2D) thin and thick films such as refs.[24, 25] and three dimensional (3D) electrodes [26]. The latter has gained rather more attention recently due to advances in microfabrication technologies. In the 2D approach, the electrodes (and electrolytes) are fabricated as film layers which, if combined, form an electrochemical cell. In this approach, thin or thick films of electro-active materials are utilized which can be either printed, or deposited by various techniques such as sol-gel, electrodeposition, physical and chemical vapor deposition or atomic layer deposition [18].

In the present work, we report on a NiMH microbattery which is fabricated on a glass substrate. In fact, silicon dioxide-based materials (e.g. glass) have been extensively utilized for the fabrication of microfluidic devices in academia while polymers are more explored as microfluidic substrates in industry. The microfabrication process is comprised of methods which are commonly utilized for the microfabriction of microdevices. In detail, the positive electrode of the microbattery is based on the nickel hydroxide $Ni(OH)_2$/nickel (oxy)hydroxide $NiOOH$ chemistry while the negative electrode consists of metal alloy material $La_{1.11\pm0.05}Ni_{4.73\pm0.02}Al_{0.19\pm0.02}$; both electrodes are in a direct contact with an aqueous alkaline electrolyte. This microbattery can be easily integrated into MEMS and microfluidic devices because it is fabricated on glass (which is one of the most common substrates for such devices). We further introduce a modular design concept for the electrodes. We have previously reported on microfabrication and characterization of single electrodes of the microbattery in refs.[27, 28]. Here, we are focused on assembling the entire microbattery and providing insights into the overall performance of the cell rather than a single electrode. This article is proceeded with a brief introduction to our experimental methodologies and materials utilized to fabricate all components of the microbattery. It is then followed by thorough discussions of our experimental results on microfabrications and electrochemical performance of the microbattery. The last section of this article provides further details with respect to the durability of the microbattery electrodes by using an impedance spectroscopy analysis. Finally, the article is summarized with some concluding remarks.

5.3 Experimental Methods and Materials

In this section, we briefly specify the materials, fabrication and characterization techniques which are used in the present work. Further details are available in refs.[27, 28].

5.3.1 Microfabrication

Materials: Glass microscope slides (Globe Scientific Inc., USA) with an area of 2.54 by 7.62 cm are used as substrates for the microfabrication of both electrodes. We employ different metal targets for the deposition of metal films on the glass substrate. Here, we use electron beam evaporation with nickel and chromium pellets (Kurt J. Lesker Canada, Inc., Canada) with purities of 99.995% and 99.998%, respectively, to grow chromium and nickel thin films serving as current collectors of the electrodes. The metal (hydride) electrodes are sputtered by using a custom made target material of $LaNi_{4.77}Al_{0.23}$ which is received from Kurt J. Lesker Canada, Inc.. The size and purity of the target are reported to be $7.62\,cm$ in diameter and 99.9%, respectively. The thickness of the target ingot is $0.317 \pm 0.025\,cm$. Materials for the preparation of the nickel (hydroxide) electrode comprise nickel(II) chloride hexahydrate (puriss. p.a., $> 98\%$, Sigma-Aldrich Canada Co., Canada), nickel(II) nitrate hexahydrate (99.999% trace metals basis, Sigma-Aldrich Canada Co., Canada), and cobalt(II) nitrate hexahydrate (reagent grade, 98%, Sigma-Aldrich Canada Co., Canada). The two-part heat curable polymer (poly)dimethylsiloxane (PDMS) (Sylgard 184, Dow Corning, USA) is used for the fabrication of the polymeric fluidic layer which also serves as an electrode separator. The materials required for the ultraviolet (UV) lithography include the chemically-amplified negative photoresist KMPR® 1000, SU-8 photoresist developer solution (Methoxy-2-propanol acetate), and a photoresist remover PG solution (1-Methylpyrrolidone (NMP)) (all from MicroChem Corp., USA).

Instruments: Metal thin films of chromium and nickel are prepared using an electron beam evaporator (Balzers, USA). Additionally, a Varian in-house-built DC magnetron sputter deposition system is employed to deposit intermetallic films of $La_{1.11\pm0.05}Ni_{4.73\pm0.02}Al_{0.19\pm0.02}$ from a target with a composition of $LaNi_{4.77}Al_{0.23}$. Temperature and argon pressure can be controlled within the sputter chamber. All film depositions are performed at the Microelectronics Fabrication Laboratory (MFL) at Carleton University in Ottawa, Canada. In terms of the electroplating and the electrodeposition process, a power supply (U8002A, Agilent Technologies, USA) along with a potentiostat/galvanostat (PGSTAT302N, Metrohm Autolab B.V., The Netherlands) is employed. For the UV lithography step, we use a glass photo-mask featuring a grid style pattern consisting of squares of $400 \times 400\,\mu m^2$ which is received from nanoFAB at the University of Alberta (Canada). A mask aligner (Oriel Instruments, USA) coupled with a light intensity controller, timer, and ultraviolet (UV) lamp is utilized to transfer the mask pattern to the photoresist.

5.3.2 Materials and Physical Characterization

The elemental composition of the deposited films is examined using X-ray diffraction (XRD), X-ray photoelectron spectroscopy (XPS) and energy dispersive spectroscopy (EDS) instruments. The surface morphology is investigated by a field emission scanning electron microscope (FESEM) and a stylus profiler. We observe that the patterned nickel hydroxide film consists of $Ni(OH)_2 \cdot 0.75H_2O$, i.e., (hydrated) α-$Ni(OH)_2$. The metal hydride film electrode consists of $La_{1.11\pm0.05}Ni_{4.73\pm0.02}Al_{0.19\pm0.02}$ which is very close to the elemental composition of the target used for sputtering, i.e., $LaNi_{4.77}Al_{0.23}$. The grain size of the metal hydride film is found to be roughly $20\,nm$ throughout the surface of the film electrode. Note that we do not discuss further details of the materials characterization as they have been previously reported elsewhere in refs.[27, 28].

5.3.3 Electrochemical Characterization

The microfabricated battery is electrochemically characterized by measuring voltage-current and galvanostatic charge-discharge profiles using a combined potentiostat/galvanostat instrument (PGSTAT302N, Metrohm Autolab B.V., The Netherlands). Electrochemical impedance spectroscopy (EIS) is also performed using this instrument. All electrochemical measurements are generally performed in aqueous $1M$ potassium hydroxide (KOH) solutions at a room temperature of $23\,^{\circ}C$. However, we also study the effect of the electrolyte concentration on the performance of the microbattery using $0.75M$ and $0.5M$ KOH electrolyte concentrations. All electrolyte solutions are prepared with deionized water with a conductivity of approximately $2\,\mu S\,cm^{-1}$. Conductivities and pH values are tested using a modular pH and conductivity meter (Mettler-Toledo, SevenMulti, Switzerland). Further comprehensive electrochemical characterization of the single electrodes in terms of cyclic voltammetry can be found in refs.[27, 28].

5.4 Results and Discussion

In this section, we first introduce the microbattery and microfabrication methodologies. We then give insights into the electrochemical performance and the charge-discharge capability of the microbattery. Finally, we present the results of the electrochemical impedance spectroscopy.

5.4.1 Microbattery Microfabrication

The nickel/metal hydride microbattery is fabricated by using common methods in the semiconductor industry. Figure 5.1(a) illustrates the design of the microbattery. The electrodes are fabricated on glass substrates with a size of $2.54\,cm$ by $7.62\,cm$. Since glass-like substrates are most commonly used in microfluidic and LOC devices, we pursue the electrode fabrication on this material as well. We use a sandwich–like configuration to assemble the entire cell in that the electrodes stack one above the other and the polymeric fluidic layer is placed between the electrodes. In fact, a polymeric PDMS layer with microchannels is usually sandwiched between two glass-like substrates in the microfluidic chips. That is, our microbattery configuration mimics the integration onto a microfluidic chip without using an actual device.

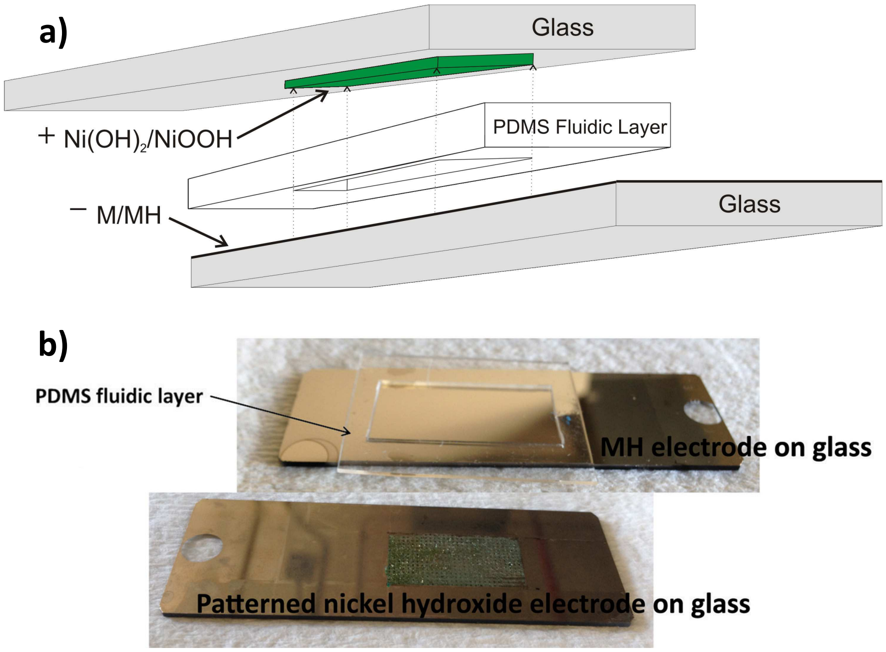

Figure 5.1: a) Sketch of the entire microbattery; b) Actual patterned nickel hydroxide and metal hydride electrodes, and PDMS fluidic layer.

Both positive and negative electrodes on glass substrates are shown in Figure 5.1(b). We first deposit thin layers of metals, which are used as current collectors of the microbattery, on the glass substrate by employing an electron beam evaporation method. It turns out that pure nickel hardly adheres to the glass surface. An improved adhesion is achieved, when we first evaporate a 60 nm thin film of chromium to deposit an adhesion (seed) layer onto the glass surface. Then, a nickel thin film of the same thickness is grown onto the adhesion layer.

The nickel hydroxide $Ni(OH)_2$ film electrode is the positive electrode of the microbattery and is microfabricated using an electrodeposition technique from a nickel nitrate solution (with an addition of 30% cobalt nitrate solution used in this work) as previously described in ref.[27]. The $Ni(OH)_2$ is then electrochemically converted to $NiOOH$. The thickness of the $Ni(OH)_2$ film electrode is around $20\,\mu m$. We observe that the mechanical stability of these film electrodes is very poor if deposited onto the surface of planar (smooth) current collectors. Hence, we use a surface patterning process in order to create a 3D array of micropillars onto the nickel current collectors. In a nutshell, we electroplate nickel micropillars with a footprint area of $400 \times 400\,\mu m^2$ on the nickel current collector using a soft lithography technique prior to the electrodeposition of $Ni(OH)_2$. The investigation of the charge-discharge characteristics of the single electrodes demonstrates that patterning of the electrode surface on glass results in a significantly higher durability compared to a patternless surface, especially in the presence of the parasitic oxygen evolution reaction. The reader is referred to ref.[27] for further details on the microfabrication of the positive electrode of the microbattery.

The negative electrode of the microbattery is an intermetallic compound of $La_{1.11\pm0.05}Ni_{4.73\pm0.02}Al_{0.19\pm0.02}$ with an ability of electrolytic (de-)hydrogenation. Here, we grow a film layer of $La_{1.11\pm0.05}Ni_{4.73\pm0.02}Al_{0.19\pm0.02}$ on the current collector using a DC magnetron sputter instrument at room temperature and at an argon gas pressure of $0.53\,Pa$. Under these conditions, the growth rate corresponds to $0.11\,nm\,s^{-1}$ at a power of $100\,W$. The final thickness of the $La_{1.11\pm0.05}Ni_{4.73\pm0.02}Al_{0.19\pm0.02}$ film layer is around $1.1\,\mu m$ which is measured using a stylus profiler. We observe that sputtering of the intermetallic film results in an electrochemical performance which is similar to that of conventionally-fabricated electrodes, cf. ref.[28]. The $La_{1.11\pm0.05}Ni_{4.73\pm0.02}Al_{0.19\pm0.02}$ film is then hydrogenated and (theoretically) converted to $La_{1.11\pm0.05}Ni_{4.73\pm0.02}Al_{0.19\pm0.02}H_6$. For further details on the microfabrication and characterization of the negative electrode, the reader is referred to ref.[28].

Finally, the battery design comprises a polymeric layer with a thickness of around $600\,\mu m$ and made from (poly)dimethylsiloxane (PDMS) as shown in Figure 5.1(b). We use a PDMS elastomer and curing agent at a ratio of 10:1 weight basis to perform our PDMS soft lithography. A piece of LEGO$^{\text{TM}}$ is used to create a cavity of around $2.54\,cm \times 1.27\,cm$ which serves as a reservoir of the alkaline electrolyte. The polymeric fluidic layer also serves as an electrode separator. Hence, the surface area of both electrodes which is in contact with the electrolyte corresponds to that of the cavity of the PDMS layer; i.e., $2.54 \times 1.27\,cm$. It is well known that glass can be etched by concentrated KOH solutions. Nevertheless, we do not observe any hint of material degradation. On the one hand, the electrolyte is not in a direct contact with the glass substrate since the surface of the glass substrate is covered either with the electrode (which consists of mainly nickel) or with the (pure) nickel thin film which serves as a current collector. On the other hand, nickel is obviously very resistant to corrosion in the presence of a concentrated KOH electrolyte. Therefore, contrary to the nickel-zinc microbattery proposed by Humble et al. [5], we do not use an epoxy layer or any other coatings to reduce the corrosion on the glass surface. The physical parameters and dimensions of the microbattery are summarized in Table 5.1.

Microbattery Parameters	
Dimension	$2.54 \times 7.62\,cm^2$
Negative electrode materials (thickness)	$La_{1.11\pm0.05}Ni_{4.73\pm0.02}Al_{0.19\pm0.02}$ $(1.1\,\mu m)$
Positive electrode materials (approx. thickness)	$Ni(OH)_2/NiOOH(20\,\mu m)$
Fluidic layer thickness	$600\,\mu m$
Electro-active materials surface dimension	$2.54 \times 1.27\,cm^2$
Adhesion improvement layer material (thickness)	chromium $(60\,nm)$
Current collector material (thickness)	nickel $(60\,nm)$

Table 5.1: Microbattery physical dimensions and materials.

5.4.2 Electrochemical characterization

In this section, we discuss the results of charge-discharge measurements, voltage-current characteristics, and electrochemical impedance spectroscopy of the microbattery.

Galvanostatic charge-discharge characteristics

In this section, we provide some insights into the charge-discharge characteristics and the cyclability of the microbattery. The battery chemistry of the nickel/metal hydride is as follows: During the charge process, nickel hydroxide $Ni(OH)_2$ is converted to nickel (oxy)hydroxide $NiOOH$ while the intermetallic film M is hydrogenated to MH; During the discharge process, the reverse reactions occur. Hence, the overall NiMH cell reaction can be written according to:

$$NiOOH + MH \rightleftharpoons Ni(OH)_2 + M \qquad E^{0\ominus} = 1.35V \tag{5.1}$$

Figure 5.2 depicts charge-discharge characteristics of the microbattery. Before these measurements, the electrodes are preconditioned by using a linear cyclic voltammetry

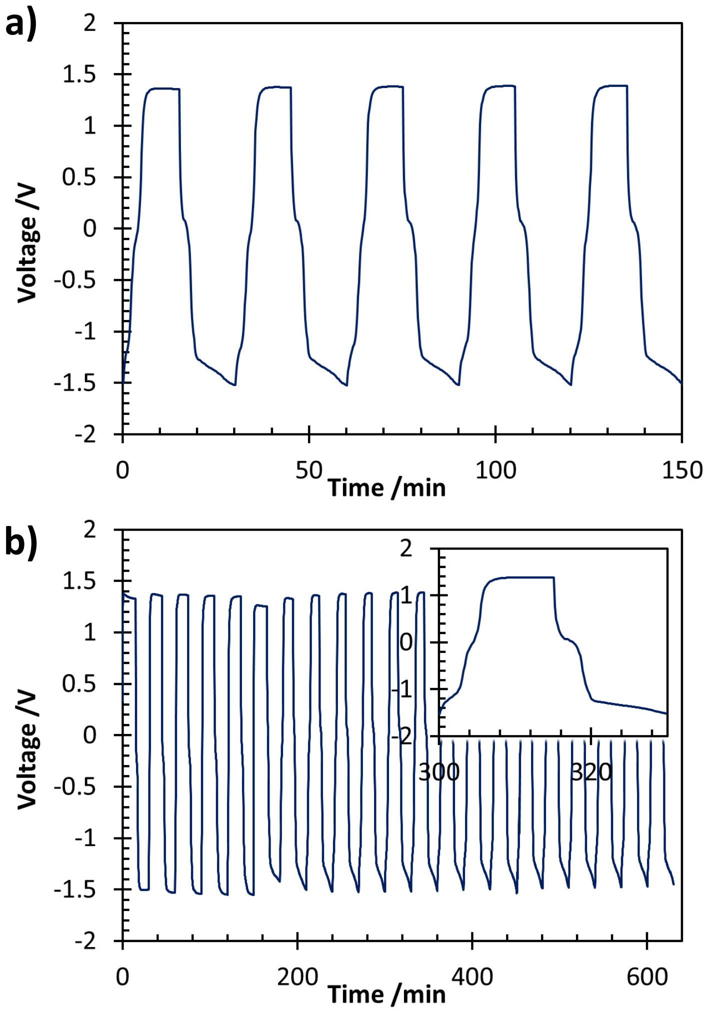

Figure 5.2: Charge-discharge characteristics of the microbattery; (insert in (b): magnification of a single charge-discharge cycle for $30\,mins$).

(CV) at a scan rate of $10\,mVs^{-1}$ until a steady and reproducible pattern is obtained which usually takes around 50 CV cycles with a voltage window of -0.5 to $0.5\,V$. In Figure 5.2(a), five charge-discharge cycles is shown which are obtained at a constant current of $0.1\,mA$ (current density of around $0.03\,mA\,cm^{-2}$, normalized with the surface area of the electrode). Additionally, Figure 5.2(b) illustrates charge-discharge capability of the microbattery in terms of the reliable number of cycles. It is found that around 20 charge-discharge cycles can be obtained with no obvious indication of film electrode deterioration. A rather severe deterioration can be seen on the nickel hydroxide film electrode if we go to a higher number of cycles while the metal hydride film electrode is still intact. Nevertheless, we can operate the battery reliably for up to around 20 charge-discharge cycles. Note that this is not the maximum number of cycles that we can obtain; the maximum number depends on the state of charge (SOC) that we achieve as discussed below. As it can be seen in Figure 5.2(a), during the charge process, the cell voltage rises to around $V_{cha} \approx 1.4\,V$ while a maximum cell voltage of around $V_{dis} \approx -1.5\,V$ is measured during the discharge process. This is in rather good agreement with the standard cell voltage of the reaction as given in reaction (5.1). We observe that the shape of the first five discharge curves (negative potentials) is different than that of the rest of the discharge curves as shown in Figure 5.2(b). We may attribute this behavior to the further activation of the films, especially the MH film electrode. In other words, the shape of the discharge cycle seems to be transiting to a sharper decrease starting at cycle#6 at the voltage boundary. This behavior can be seen in Figure 5.2(a) as these charge-discharge cycles are obtained after the transition has been completed. Note that the rest of the displayed cycles, from cycle#6 to cycle#21 shows a similar discharge-voltage behavior. Additionally, we observe that the shape of the discharge voltage varies significantly from that of charge voltages. This can be attributed to different overvoltages present during the charge and discharge state.

Generally, the (de-)hydrogenation of the intermetallic film electrode occurs in three phases. The first is the so-called "$\alpha-$phase" referring to the state in which hydrogen and metal mix in the form of a solid-solution. The next phase is transitional which is called "$\alpha-$ and $\beta-$phase" and is featured by a plateau region in the voltage-current and charge-discharge characteristic plots. Here, the hydrogen continuously occupies the interstitial sites of the intermetallic film electrode. Once the intermetallic electrode is almost saturated with hydrogen, the metal hydride is referred to reach the "$\beta-$phase. For further details on various phases of the metal hydride materials, the reader is referred to ref.[29]. When we inspect the charge-discharge cycles in Figure 5.2(b)(insert), we observe a charge plateau (transition region) at around (starting at) $-0.19\,V$ with an upward slope while the discharge plateau is obtained at around (starting at) $0.14\,V$. Note that a smaller plateau is also observed at around $-1.3\,V$ which indicates that the microbattery cell features a multi-plateau behavior which can be assigned to the metal hydride electrode. The multi-plateau behavior of this metal hydride film electrode has also been observed in our previously reported work in ref.[28].

As already mentioned above, the adjustment of the state of charge (SOC) at a particular level by controlling the charging-discharging time is important to maintain the mechanical integrity of the film electrodes. It is found that when we perform a $15\,mins$ charge followed by $15\,mins$ discharge, we do not observe any signs of degradation of the electrode surface. The optimized conditions obtained in our previous works [27, 28] are also used for testing the microbattery in the present work. We find that the charge-discharge voltages remain relatively stable–there is no significant increase of overvoltages with increasing number of cycles. That is, the shape of the charge-discharge curves is more or less identical for all cycles after the first five cycles.

We estimate that the state of charge is around 25% for the above-mentioned charge-discharge duration. Since, we are not able to measure depth of discharge reliably due to severe deterioration on the nickel hydroxide film electrode if the potential and charging time are not limited, we use a method as described in ref.[27]. Here, we just give the final results. In detail, it is found that this charging protocol results in a faradic capacity of the patterned nickel hydroxide film electrode of around 70 $mA\,h\,g^{-1}$ ($400\,\mu A\,h\,cm^{-2}$ with electrode thickness of around $20\,\mu m$, and a film density of $2.82\,g\,cm^{-3}$ as obtained from XRD results) and therefore in a SOC of 25%. Also, we estimate the specific capacitance of the nickel hydroxide film to be around $3600\,Cg^{-1}$ at a voltage of $1.2\,V$ [27]. This high capacitance indicates that the charges which are transferred during charge and discharge processes are more likely to be stored in or withdrawn from the electrical double layer (EDL) rather than due to an electrochemical reaction. We give further insights into the double layer capacitance of the nickel hydroxide film electrode below. In terms of the metal hydride film electrode, we do not observe any sign of degradation even at a longer charging duration (i.e., higher utilization of the electrode materials). We find that the MH electrode can be cycled for more than 40 cycles with a respective charge and discharge time of $30\,min$. The faradic capacity of the MH film electrode corresponds then to approximately 50 $mA\,h\,g^{-1}$ ($40\,\mu Ah\,cm^{-2}$ with electrode thickness of $1.1\,\mu m$ and weighted average film density of $8.24\,g\,cm^{-3}$) resulting in a SOC of 25% as well. Therefore, we conclude that the cell is limited by the MH electrode (negative electrode) since the capacity of the nickel hydroxide film electrode is higher than that of MH film electrode.

A scale-up of the negative electrode (MH film electrode) capacity by increasing the film thickness appears intriguing at the first glance. We are able to deposit a mechanically stable intermetallic film of $1.1\,\mu m$ with our sputter instrument at a deposition rate of $0.11\,nm\,s^{-1}$. The estimated electroactive mass of the metal hydride film which is in contact with the electrolyte is $\approx 2.5 \times 10^{-3}\,g$. However, the DC magnetron sputtering method, which is used to deposit our intermetallic film electrodes, and many other commonly-used deposition techniques in the semiconductor (electronics) industry, have usually limitations in terms of film thickness. It should also be emphasized that the surface of the film, which is not in a direct contact with the electrolyte, does not show any indication of lattice expansion (or in severe cases, film degradation) or changes due to the hydriding process, hence, it has not undergone (de-)hydrogenation processes. The mass of the electroactive MH film is used to estimate the capacity of the microbattery since the cell is anode (negative electrode) limited. If we compare our performance data with other batteries which have been reported in the literature, the work of Humble et al.[5] is an obvious choice since they use a nickel based chemistry for the positive electrodes as well. However, their microbattery, contrary to ours, is limited by the positive electrode and they report the capacity of the entire cell based on the capacity of the nickel hydroxide electrode. Furthermore, they utilize a negative zinc electrode with a much larger thickness of $15\,\mu m$. Therefore, we normalize our area-specific microbattery capacity with the thickness of the MH film (our negative electrode) and compare it to the normalized capacity based on the zinc anode electrode in ref.[5]. Eventually, Humble et al. reported a cell capacity of $1.4\,C\,mm^{-2}$ normalized by the area of the entire cell including sidewalls in ref.[5]. For the sake of comparison, if we normalize this capacity with the thickness of the anode ($15\,\mu m$), we arrive at $0.93\,C\,mm^{-3}$. We estimate an area-specific capacity (the area includes both electrode surfaces, and sidewalls) of $0.66\,C\,mm^{-3}$ (normalized with the thickness of the MH film electrode) for our microbattery.

Voltage-current characteristics

In this section, we give insights into the voltage-current characteristics of the microbattery at three different electrolyte concentrations, namely $1M$, $0.75M$, and $0.5M$. Given the intended application of the microbattery in microfluidic devices, the use of less concentrated electrolyte is desired. Generally, most of the commonly used microfluidic devices operate with liquids with rather low ionic contents and the use of a less concentrated electrolyte is beneficial with respect to the corrosion protection of microfabricated components on glass-like substrates. In order to prepare for the measurements, we first perform 30 current sweep cycles in the range of 0 to $0.1\,mA$ to condition the electrode surfaces. Then, we charge the microbattery for $15\,mins$ before the voltage-current plot is measured; this corresponds to a SOC of around 25%. All current values that we measure are normalized by the surface area of the electrode which is in contact with the electrolyte. We perform a few trials to obtain a suitable current range in which the electrodes are stable, and unwanted parasitic reactions are suppressed. We find that increasing the current density for up to around $6\,\mu A\,cm^{-2}$ along with end-point voltage of around $1.0\,V$ provides a good microbattery performance. Note that the end-point voltage of around $1.0\,V$ has been commonly utilized for various NiMH battery cells as can be found in ref.[30].

The results of the measurements with three different electrolyte concentrations are given in Figure 5.3. We observe a very weak dependency of the open circuit voltage (OCV) on the electrolyte concentration. In detail, an OCV of around $1.19\,V$ for an electrolyte concentration of $1M$ KOH is measured while similar values of 1.18 and $1.17\,V$ are measured for electrolyte concentrations of $0.75M$ and $0.5M$ KOH, respectively. It has been reported that the OCV of a NiMH battery cell at a SOC of 25% is around $1.25\,V$ [31] while the theoretical (reversible) OCV is $1.35\,V$ as mentioned above in reaction (5.1). Note that the OCV of the NiMH macrobatteries ranges between 1.25 and $1.35\,V$ with a nominal voltage of $1.2\,V$ at around room temperature [30]. In summary, we realize that the difference between the experimental OCV of this microbattery and OCVs of the macrobatteries (ref.[30]) ranges from 70 ± 10 to $170 \pm 10\,mV$. If we compare the experimental OCV of the microbattery to that of reported in ref.[31] for a SOC 25%, we find a smaller voltage difference of approx. $70 \pm 10\,mV$. We attribute the relatively lower OCV values of the microbattery to the use of cobalt as an additive in the microfabrication of the nickel hydroxide film electrode. The addition of cobalt mitigates the unwanted parasitic oxygen evolution reaction, cf. e.g., refs.[32, 33]. This reaction contributes to the mechanical degradation of the nickel hydroxide film electrodes especially for a larger number of charge-discharge cycles. In detail, a concentration of around $30\,wt\%$ cobalt nitrate is added to the electrodeposition bath of the nickel nitrate solution in our work. The addition of cobalt leads to lower nickel (cathode) potentials resulting in lower cell voltage. Cyclic Voltammetry measurements (results not shown) reveal that the oxidation peaks are shifted between 100 and $140\,mV$ depending on the scan rates (i.e., 0.5, 2, and $5\,mVs^{-1}$) which is in agreement to the decrease of OCV of the microbattery cell. Additionally, in our previous work [28], we introduced a correlation which give the equilibrium potential of the metal hydride film electrode depending on its hydrogen content. We use this correlation along with an oxidation peak potential obtained for the nickel electrode when using cobalt as an additive (results not shown) to estimate the OCV of the entire cell. We arrive in 1.16 V, slightly lower than the measured one for the microbattery cell as shown in Figure 5.3, which demonstrates the quality of the correlation.

In terms of the voltage characteristics when a current is withdrawn, it appears for all concentrations that the activation polarization is rather insignificant. We generally observe that the voltage linearly drops with the current density; i.e., the behavior is mainly determined by the ohmic overpotential (ohmic polarization). Furthermore, a rather weak concentration overpotential can also be seen at higher operating current densities.

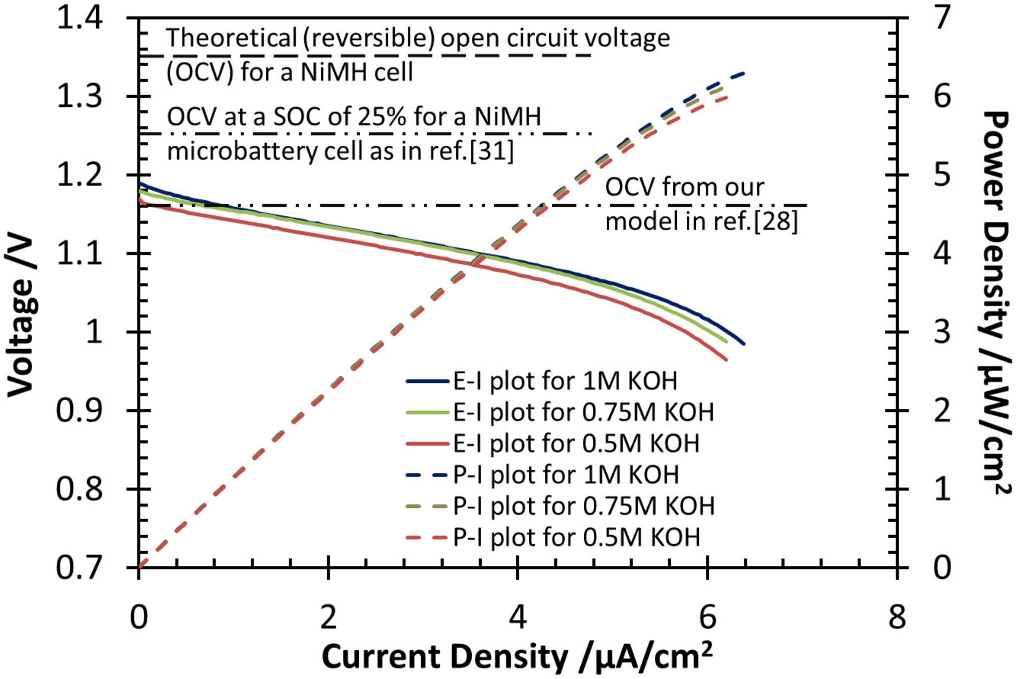

Figure 5.3: Voltage-current and power-current characteristic curves at three different electrolyte concentrations.

In terms of the influence of the electrolyte concentration on the cell performance, we observe almost identical performance for the operation with $1\,M$ and $0.75\,M$ electrolyte concentration but with a slightly more pronounced concentration polarization at high current densities for the less concentrated electrolyte, i.e., $0.75M$ KOH. In the case of the electrolyte concentration of $0.5\,M$, we find that the voltage is always lower compared to that of higher electrolyte concentrations.

In terms of power density and operation mode, Figure 5.3 depicts power density of the microbattery as a function of current density withdrawn from the cell at three different electrolyte concentrations. Generally, we observe that the power density values of the microbattery for all electrolyte concentrations are almost the same with a small deviation for current densities larger than $5\,\mu A\,cm^{-2}$. It is found that the microbattery provides a power density of around $5\,\mu W\,cm^{-2}$ at a current density of around $5\,\mu A\,cm^{-2}$ while maintaining a cell voltage of larger than $1V$.

Electrochemical impedance spectroscopy

In this section, we present our results obtained from electrochemical impedance spectroscopy for the entire microbattery cell. In detail, we apply a voltage of $10\,mV$ between the electrodes and scan over a frequency range of $0.001\,Hz$ to $1.0\,MHz$ and measure the respective current. We adjust the potential to such a small value to avoid any electrochemical reaction to occur. Otherwise, the electrode surfaces and the conversion degrees would considerably change during the measurements at low frequencies. All impedance measurements are performed after surface conditioning for around 30 cycles with a current sweep from 0 to $0.1\,mA$. For the sake of comparison, we perform impedance measurements on an immaculate cell (prior to surface conditioning), after conditioning, after 10 charge-discharge cycles, and after

25 charge-discharge cycles.

For the interpretation of the impedance data, an equivalent electrical circuit is required. We choose a serial arrangement of three RC elements; i.e., (RC)(RC)(RC), shown as an insert in Figure 5.4. Here, the left and the right RC elements denote the charge transfer resistance and the capacitance of the nickel hydroxide and the metal hydride electrode, respectively. The middle RC element accounts for the characteristics of the electrolyte where we account for the capacitance of the electrolyte since the distance between the two electrodes is small. An estimation results in an electrolyte ohmic resistance and capacitance of approximately $R_{el} \approx 1\,\Omega$ and $C_{el} \approx 140\,pF$, respectively. These values are used as initial guesses for the regression of the data in our equivalent circuit modelling.

The Nyquist plot for the various experimental conditions is shown in Figure 5.4. We find that the shape of all curves more or less corresponds to a segment of a semi-circle where the distance of the data points to the origin is a measure for the frequency. In other words, the frequency of the impedance increases from the left to the right. According to the interpretation of the equivalent circuit, all capacitors are short-circuited at the highest frequencies. Hence, the intercept of the real part axis of the impedance gives the value of the sum of the electrolyte resistance and the charge transfer resistance of the electrodes. As it can be seen in Figure 5.4, we do not observe a significant difference in this combined value for all conditions of the microbattery. Indeed, the main difference is rather the height of the circle segments which is related to the electrode capacitances.

We summarize the quantitative results of the data regression in Table 5.2. We realize that the electrolyte resistance and capacitance remain more or less constant

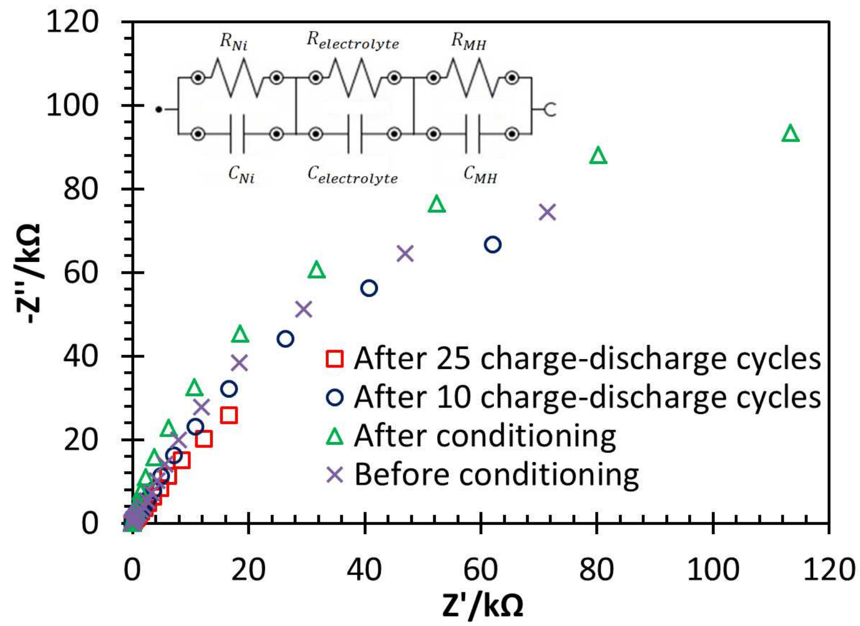

Figure 5.4: Nyquist plot and equivalent circuit (insert) of the microbattery at various conditions.

State of microbattery	$R_{ctr,Ni}$	$C_{dl,Ni}$	R_{El}	C_{El}	$R_{ctr,MH}$	C_{MH}
Before conditioning	$75.8\,k\Omega$	$574\,\mu F$	0.80Ω	$116\,pF$	$16.3\,\Omega$	$289\,pF$
After conditioning	$129\,k\Omega$	$397\,\mu F$	0.88Ω	$114\,pF$	$12.0\,\Omega$	$313\,pF$
After 10 charge-discharge cycles	$70.8\,k\Omega$	$739\,\mu F$	0.60Ω	$111\,pF$	$12.5\,\Omega$	$482\,pF$
After 25 charge-discharge cycles	$10.2\,k\Omega$	$1.23\,mF$	0.65Ω	$120\,pF$	$15.1\,\Omega$	$575\,pF$

Table 5.2: Equivalent circuit values of the microbattery at various conditions

for all investigated conditions. The values, given the accuracy of the method, are in good agreement with the estimated electrolyte resistance and capacitance mentioned above. When we compare the absolute value of the electrolyte resistance with the electrode charge transfer resistances, we realize a difference which is at least on the order of 2 magnitudes. That is, the electrolyte resistance has no significance. Additionally, we realize that the capacitance of the electrolyte, as well as that of the metal hydride electrode, is six order of magnitude smaller than the capacitance of the nickel hydroxide electrode. In other words, the capacitance of the microbattery is governed by the nickel hydroxide film electrode which is as expected. We further find that the charge transfer resistance of nickel hydroxide film electrode $R_{ctr,Ni}$ ranges between $10.2\,k\Omega$ and $129\,k\Omega$. Moreover, we observe that the higher is the charge transfer resistance, the lower is the capacitance. However, we do not find a simple behavior in terms of the utilization degree of the electrode. Generally, we would expect to find higher charge transfer resistances over the number of charge-discharge cycles as a sign of degradation. Contrary to this assumption, we realize that the lowest charge transfer resistance (and the highest capacitance) is observed for the most utilized state of the electrode; i.e., after 25 cycles where the nickel electrode shows some signs of deterioration. Generally, we see an increasing trend in $C_{dl,Ni}$ as the utilization increases. Since the capacitance is related to the electrical double layer (EDL) of the electrode, it appears that the structural surface changes with the increasing utilization conveys that more surface is generated while the charge transfer resistance is maintained or even reduced.

In contrast, the charge transfer resistance $R_{ctr,MH}$ of the metal hydride film electrode is on the order of $10\,\Omega$ and therefore much smaller than that of the nickel hydroxide film electrode. Likewise, the capacitance values of the nickel hydroxide film electrode are much larger than those of metal hydride electrodes, the difference is about six order of magnitudes. This can be attributed to the porous structure and very large surface area of the nickel hydroxide film electrode contrary to the metal hydride film electrode. With respect to these significant differences between the electrodes, the interpretation of the change in the metal hydride parameters over the utilization degree is rather difficult.

5.5 Concluding Remarks

This study is concerned with the microfabrication of a nickel metal hydride microbattery on glass substrates which can be integrated (embedded) in various microdevices. We conclude this article with the following remarks:

1) We show that the fabrication of a NiMH microbattery cell on glass substrates is possible by employing common microfabrication techniques. The microbattery provides a capacity of around 50 $mA\,h\,g^{-1}$ for a SOC of 25% (40 $\mu Ah\,cm^{-2}$ with the limiting electrode thickness of 1.1 μm) which can be utilized in applications requiring low capacities. For instance, if we assume an operation time of around 4 $hr\,day^{-1}$ for the wireless sensor node reported for health monitoring system by Okada et al.[8, 7] as mentioned above, an approximate capacity of 1.7 μAh per day (50 μAh per month) at a nominal voltage of 1.2 V is required. This capacity is adequate for the sensor to perform the measurement every minute for a duration of 10 seconds. Assuming a SOC of 100%, the microbattery presented in this work has a capacity of around 160 $\mu Ah\,cm^{-2}$ (520 μAh for a film electrode surface area of $2.54 \times 1.27\,cm$) is able to provide sufficient power for the sensor to operate for around 10 months. Since we need to maintain around 25% SOC of the microbattery to prevent mechanical instability within the film electrodes, the microbattery can provide sufficient power for the sensor for around 2.5 months of operation for a single charge. For the sake of comparison with other microbatteries, Albano et al. have reported capacities of up to 138 $\mu Ah\,cm^{-2}$ for an integrated zinc-silver oxide primary microbattery for implantable MEMS devices [10] while Humble et al. have stated a capacity range of 278 to 972 $\mu Ah\,cm^{-2}$ for a

nickel-zinc microbattery [5]. A much larger capacity range has also been reported by Do et al. ranging between 1170 and 3150 $\mu Ah\, cm^{-2}$ [22, 23] for a screen printed NiMH microbattery. However, this design includes a membrane in their microbattery which not only increases the costs of fabrication but also results in fabrication complexities.

The microbattery is a rechargeable (secondary type) cell and could be coupled with an energy harvesting device, such as a solar cell, to make an autonomous power supply system. Additionally, we introduce a modular design for the microbattery electrodes. That is, in the case of electrode degradation, either electrodes can be replaced with a newly fabricated one. This would be possible since the electrodes are separately fabricated onto different glass substrates contrary to the designs where both electrodes are on the same substrate along with the electrolyte such as the work by Humble et al. in ref.[5]. Note that in the case of an integrated (embedded) cell within a device, the electrodes can not be easily replaced. Nevertheless, the modular design allows for a straightforward numbering-up approach by arranging singles batteries into a stack.

2) The cyclability of the microbattery is investigated using an electrochemical impedance spectroscopy analysis. Here, the microbattery is dominated by the nickel hydroxide film electrode in terms of degradation. Hence, further improvement is required in order to increase the number of possible charge-discharge cycles. One possibility could be to use an etching method to pattern the surface of the glass substrates in order to increase the adhesion surface area at the interface of the films and the glass substrates which may result in better electrode durability. In the present work, a grid style pattern consisting of squares of $400 \times 400\, \mu m^2$ is used to improve the cyclability of the nickel hydroxide film electrode. Further improvement would be

expected to achieve by using rather smaller or different grids shape or aspect ratio. As for the metal hydride film electrode, further durability improvement could be achieved by the same pattering method used for the nickel hydroxide film electrode.

3) The presented microbattery is able to provide an area-specific and volumetric power density of around $0.05\,W\,m^{-2}$ and $0.045\,W\,cm^{-3}$, respectively, while maintaining a voltage of above $1\,V$. There have been various power sources reported in the literature with a range of power densities. For instance, Lam et al. have reported a MEMS-based photosynthetic cell with a power density of around $10^{-10}\,W\,cm^{-3}$ [34] while Lemmerhirt and Wise have mentioned a lithium cell fabricated by common microfabrication methods with an estimated power density range of 0.075 to $1.5\,W\,m^{-2}$ (for a nominal voltage of $3.75\,V$) (ref.[35] as cited in ref.[10]). High volumetric power densities are also reported such as works of Humble et al. (Ni-Zn cell) and Pikul et al. (lithium cell) with $3\,W\,cm^{-3}$ and $74\,W\,cm^{-3}$, respectively [5, 17]. Note that such high power densities may not be necessary when site-specific integrated power supplies are coupled with low power microdevices especially in MEMS applications. Nevertheless, further improvements in terms of materials and mechanical integrity of the film electrodes will lead to higher power densities along with improved cyclability.

5.6 Acknowledgments

The authors gratefully acknowledge the financial support from Queen's University, the Natural Sciences and Engineering Research Council of Canada (NSERC), and CMC microsystems. We would like to thank Johanna Bort for her assistance with the fabrication of the polymeric fluidic layer.

5.7 Nomenclature

C	Capacitance [F]
E	Potential [V]
R	Resistance [Ω]
V	Voltage [V]
α	Single phase (dehydrided)/anhydrated phase
$\alpha + \beta$	Transition phase when α and β phases coexist
β	Single phase (hydrided)/hydrated phase

5.8 References

[1] Jack W Judy. Microelectromechanical systems (MEMS): fabrication, design and applications. *Smart Mater. Struct.*, 10(6):1115, 2001.

[2] Darwin R. Reyes, Dimitri Iossifidis, Pierre-Alain Auroux, and Andreas Manz. Micro Total Analysis Systems. 1. Introduction, Theory, and Technology. *Anal. Chem.*, 74(12):2623–2636, 2002.

[3] P Abgrall and A-M Gué. Lab-on-chip technologies: making a microfluidic network and coupling it into a complete microsystem–a review. *J. Micromech. Microeng.*, 17(5):R15, 2007.

[4] Paul Yager, Gonzalo J. Domingo, and John Gerdes. Point-of-Care diagnostics for global health. *Annu. Rev. Biomed. Eng.*, 10(1):107–144, 2008.

[5] Paul H. Humble, John N. Harb, and Rodney LaFollette. Microscopic nickel–zinc batteries for use in autonomous microsystems. *J. Electrochem. Soc.*, 148(12):A1357–A1361, 2001.

[6] Robert Puers and Patrick Wouters. Adaptable interface circuits for flexible monitoring of temperature and movement. *Analog Integr. Circuits Signal Process.*, 14(3):193–206, 1997.

[7] H. Okada, H. Nogami, T. Kobayashi, T. Masuda, and T. Itoh. Development of ultra low power wireless sensor node with piezoelectric accelerometer for health monitoring. In *Solid-State Sensors, Actuators and Microsystems (TRANSDUCERS EUROSENSORS XXVII), 2013 Transducers Eurosensors XXVII: The 17th International Conference on*, pages 26–29, June 2013.

[8] H. Okada, T. Itoh, and T. Masuda. Development of custom CMOS LSI for ultra-low power wireless sensor node in health monitoring systems. In *Sensors, 2011 IEEE*, pages 1197–1200, Oct 2011.

[9] Anantha P. Chandrakasan, Naveen Verma, and Denis C. Daly. Ultralow-power electronics for biomedical applications. *Annu. Rev. Biomedical Engineering*, 10(1):247–274, 2008. PMID: 18647116.

[10] F. Albano, Y.S. Lin, D. Blaauw, D.M. Sylvester, K.D. Wise, and A.M. Sastry. A fully integrated microbattery for an implantable microelectromechanical system. *J. Power Sources*, 185(2):1524 – 1532, 2008.

[11] Xue-Ping Gao and Han-Xi Yang. Multi-electron reaction materials for high energy density batteries. *Energy Environ. Sci.*, 3:174–189, 2010.

[12] Jilei Liu, Minghua Chen, Lili Zhang, Jian Jiang, Jiaxu Yan, Yizhong Huang, Jianyi Lin, Hong Jin Fan, and Ze Xiang Shen. A flexible alkaline rechargeable Ni/Fe battery based on graphene foam/carbon nanotubes hybrid film. *Nano Lett.*, 14(12):7180–7187, 2014.

[13] Jinkui Feng, Binggong Yan, Man O. Lai, and Lu Li. Design and fabrication of an all-solid-state thin-film li-ion microbattery with amorphous TiO2 as the anode. *Energy Technology*, 2(4):397–400, 2014.

[14] Nana Amponsah Kyeremateng, Chrystelle Lebouin, Philippe Knauth, and Thierry Djenizian. The electrochemical behaviour of TiO2 nanotubes with Co3O4 or NiO submicron particles: Composite anode materials for Li-ion micro batteries. *Electrochim. Acta*, 88(0):814 – 820, 2013.

[15] Konstantinos Gerasopoulos, Matthew McCarthy, Elizabeth Royston, James N Culver, and Reza Ghodssi. Nanostructured nickel electrodes using the tobacco mosaic virus for microbattery applications. *J. Micromech. Microeng.*, 18(10):104003, 2008.

[16] Kyle T. Braam, Steven K. Volkman, and Vivek Subramanian. Characterization and optimization of a printed, primary silver-zinc battery. *J. Power Sources*, 199(0):367 – 372, 2012.

[17] J. Pikul, H. Zhang, J. Cho, P. Braun, and W. King. High power lithium ion microbatteries with lithographically defined 3-D porous electrodes. In *Intl. Conf. on Micro Electro Mechanical Systems (MEMS), 2013 IEEE 26th*, pages 857–860, 2013.

[18] JFM Oudenhoven, RJM Vullers, and R Schaijk. A review of the present situation and future developments of micro-batteries for wireless autonomous sensor systems. *Int. J. Energy Res.*, 36(12):1139–1150, 2012.

[19] A Armutlulu, Y Fang, S H Kim, C H Ji, S A Bidstrup Allen, and M G Allen. A MEMS-enabled 3D zinc-air microbattery with improved discharge characteristics based on a multilayer metallic substructure. *J. Micromech. Microeng.*, 21(10):104011, 2011.

[20] C C Ho, K Murata, D A Steingart, J W Evans, and P K Wright. A super ink jet printed zincsilver 3d microbattery. *J. Micromech. Microeng.*, 19(9):094013, 2009.

[21] C C Ho, J W Evans, and P K Wright. Direct write dispenser printing of a zinc microbattery with an ionic liquid gel electrolyte. *J. Micromech. Microeng.*, 20(10):104009, 2010.

[22] Jing-Shan Do, Sen-Hao Yu, and Suh-Fen Cheng. Thick-film nickel–metal-hydride battery based on porous ceramic substrates. *J. Power Sources*, 117(12):203 – 211, 2003.

[23] Jing-Shan Do, Sen-Hao Yu, and Suh-Fen Cheng. Preparation and characterization of thick-film Ni/MH battery. *Biosens. Bioelectron.*, 20(1):61 – 67, 2004.

[24] C Branci, N Benjelloun, J Sarradin, and M Ribes. Vitreous tin oxide-based thin film electrodes for Li-ion micro-batteries. *Solid State Ionics*, 135(14):169 – 174, 2000.

[25] N.J. Dudney and B.J. Neudecker. Solid state thin-film lithium battery systems. *Curr. Opin. Solid State Mater. Sci.*, 4(5):479 – 482, 1999.

[26] Menachem Nathan, D. Golodnitsky, V. Yufit, E. Strauss, T. Ripenbein, I. Shechtman, S. Menkin, and E. Peled. Three-dimensional thin-film Li-ion microbatteries for autonomous MEMS. *J. Microelectromech. Syst.*, 14(5):879–885, 2005.

[27] H Falahati, E Kim, and D.P.J. Barz. Fabrication and characterization of thin-film nickel hydroxide electrodes for micro-power applications. *Accepted for publication in ACS Applied Materials & Interfaces, 22/05/2015*, 2015.

[28] H Falahati and DPJ Barz. Fabrication and characterization of thin film metal hydride electrodes for battery applications. *To be submitted*, 2015.

[29] H Falahati and DPJ Barz. Evaluation of hydrogen sorption models for AB5-type metal alloys by employing a gravimetric technique. *Int. J. Hydrogen Energy*, 38(21):8838 – 8851, 2013.

[30] D. Linden and T.B. Reddy. *Handbook of batteries.* McGraw-Hill handbooks. McGraw-Hill, 2002.

[31] Novie Ayub Windarko and Jaeho Choi. SOC estimation based on OCV for NiMH batteries using an improved Takacs model. *J. Power Electron.*, 10(2):181–186, 2010.

[32] Dennis A. Corrigan and Richard M. Bendert. Effect of coprecipitated metal ions on the electrochemistry of nickel hydroxide thin films: Cyclic voltammetry in 1M KOH. *J. Electrochem. Soc.*, 136(3):723–728, 1989.

[33] Wen-Hua Zhu, Jia-Jun Ke, Hong-Mei Yu, and Deng-Jun Zhang. A study of the electrochemistry of nickel hydroxide electrodes with various additives. *J. Power Sources*, 56(1):75 – 79, 1995.

[34] Kien Bang Lam, Eric A Johnson, Mu Chiao, and Liwei Lin. A MEMS photosynthetic electrochemical cell powered by subcellular plant photosystems. *J. Microelectromech. Syst.*, 15(5):1243–1250, 2006.

[35] D.F. Lemmerhirt and K.D. Wise. Chip-scale integration of data-gathering microsystems. *Proc. IEEE*, 94(6):1138–1159, 2006.

Chapter 6

Conclusion and Outlook

This thesis is concerned with the fabrication of a rechargeable microbattery as a microscale power supply. In detail, we develop and characterize a nickel/metal hydride (NiMH) microbattery on a glass substrate, which can be ultimately integrated in various microsystems. The majority of the research works in this thesis are experimental, however, it also includes some mathematical modelling of the characteristics of the negative (metal hydride) electrode of the microbattery as given in chapters II and IV. In chapter II, further insights are given into the (gaseous) hydrogen sorption characteristics and the mathematical model evaluations of commonly used intermetallic compounds for the negative electrode of a NiMH battery. The results of the electrode fabrication and characterization for the nickel hydroxide and the metal hydride films are presented in chapters III and IV, respectively. Finally, chapter V presents the results of the microbattery assembly and its electrochemical performance. This chapter proceeds with a summary of findings and observations in the works given in each chapter of the thesis. This chapter is concluded with some recommendations for further research.

6.1 Summary of Findings in this Thesis

The scientific findings along with observations are summarized as follows:

Paper #1 in chapter II:

In this work, two AB_5–types hydrogen sorption intermetallic alloys –i.e., $LaNi_5$ and $LaNi_{4.5}Co_{0.5}$– are characterized in terms of (de-)hydrogenation based on gravimetric measurements. We use the experimental results to review and evaluate the applicability of known P-C-T (pressure-concentration-temperature) models found in the literature in terms of their ability to describe the α- , β-, and $\alpha + \beta$-phase regions of the sorption processes. It is found that the thermodynamic-based Zhou model cannot resolve the seamless transition of the isotherms between the phases while the empirical-based Bjurström and the kinetic-based Feng models can. Further, it is found that all these models are capable of describing the non-idealities of the plateau regions, i.e., plateaus featuring slopes and being slightly curved. Overall, it is observed that the sorption enthalpy and entropy values estimated based on the Zhou and the Feng models are in moderate agreement with the literature. A novel model developed in this thesis, the so-called ERF model, shows good accuracy for the α- and transition phases, however, a limited accuracy in the β-phase region. This model also requires a fewer number of regression parameters compared to the Bjurström model. The investigation of the Feng model and its derivation, which is based on the sorption kinetics at the interface, prepares the foundation for the derivation of a model for the electrolytic (de-)hydrogenation. This model is introduced in chapter IV of this thesis.

Paper #2 in chapter III:

In this study, the focus is on the microfabrication of the nickel hydroxide $Ni(OH)_2$ film electrodes on glass substrates which can be used as a positive electrode of a NiMH microbattery. Here, the fabrication methods of the $Ni(OH)_2$ films are comprised of common microfabrication methods utilized in the semiconductor industry. In detail, an electron beam evaporation deposition process along with electroplating and electrodeposition are employed to grow films of pure nickel and $Ni(OH)_2$, respectively. The former is used as a current collector for the $Ni(OH)_2$ films. In this regard, some qualitative studies show that a chromium seed (sticky) film layer improves the adhesion of the nickel film current collector to the glass substrate significantly.

It is observed that patterning the surface of the nickel current collector with a three-dimensional (3D) array of micropillars of nickel/nickel oxide improves the durability (mechanical stability) of the $Ni(OH)_2$ films. In detail, by comparing the overall performance of the patterned electrode to that of a non-patterned electrode, it is found that a higher number of charge-discharge cycles can be performed for the patterned electrode, especially in the presence of the unwanted parasitic oxygen evolution reaction. We determine the rate-specific capacity of the non-patterned and patterned electrodes to be around 280 $mA\,h\,g^{-1}$ ($\approx 1580\,\mu A\,h\,cm^{-2}$ with electrode thickness of approx. $\approx 30\,\mu m$). However, to obtain a reasonable durability, we can only utilize around 25% of this charge content, otherwise, the electrodes last only a very limited number of cycles. The rate-specific capacity of the film electrodes is in agreement with the work of Chen et al. who have reported electrodes of a mixture of Ni and $Ni(OH)_2$ powders with a charge capacity of around $250\,mA\,h\,g^{-1}$ for a SOC of around 95% [1]. Further, a volumetric capacity (based on electrode area and electrode thickness) of 0.36 and $0.1\,Cmm^{-3}$ are obtained for patternless and patterned film electrodes, respectively. While the thickness of the film electrodes in this study is much smaller, these capacity values are in agreement with the capacity of $0.4\,C\,mm^{-3}$ (normalized by film thickness of approx. $100\,\mu m$) for patternless films on epoxy-coated silicon reported by Humble et al. [2, 3].

Paper #3 in chapter IV:

This work is concerned with the microfabrication of a metal hydride (MH) film electrode on a glass substrate –using physical vapor deposition techniques– which can serve as a negative electrode of a NiMH microbattery. In this study, an aluminium-substituted AB_5 alloy is used. We first compare the hydrogen sorption characteristics of the aluminium-substituted AB_5 alloy to those of pure AB_5 type alloy of $LaNi_5$ (which is comprehensively investigated as given in paper #1 in chapter II of this thesis) in terms of plateau pressure and activation process. It is observed that the addition of aluminum reduces the plateau pressures of the alloy which not only results in a higher hydrogen content in the metal but also results in an easier activation. The latter is of great importance with respect to the in-situ activation of microscale systems which can be a difficult process. Finally, using the comparison of the data for the pure and the aluminium-added alloys, the latter is chosen for the fabrication of the metal hydride film electrode.

In terms of microfabrication of the electrodes, we first deposit a chromium seed layer on glass followed by growing a $60\,nm$ thin nickel current collector employing electron beam evaporation. Subsequently, a DC magnetron sputtering technique is used to grow a film comprised of $La_{1.11\pm0.05}Ni_{4.73\pm0.02}Al_{0.19\pm0.02}$. We estimate the specific capacity of the metal hydride film electrode to be roughly 200 $mAh\,g^{-1}$ (160 $\mu Ah\,cm^{-2}$ with a thickness of 1.1 μm). Likewise to the nickel electrode, the durability of the metal hydride films depends on the state of charge (SOC). We observe around five charge-discharge cycles for an SOC of 25%. We are able to obtain reliable charge-discharge cycles for around 45 cycles at SOCs of around 7%.

We also derive a mathematical model which can describe the electrolytic (de-)hydrogenation of the intermetallic film electrodes. The model is based on the same kinetics approach which is used to derive the Feng model as investigated in chapter II of this thesis. The model extracts the reversible potential of the metal hydride depending on hydrogen content from a single (dis)charge experiment. It can be utilized for design and analysis of electrolytic (de-)hydrogenation of intermetallic materials along with reduced experimental costs, –i.e., a fewer number of experiments needs to be performed. Also, it can have relevance for sensing applications.

Paper #4 in chapter V:

Finally, this paper is concerned with a microbattery consisting of the electrodes from the previous works. The design of the microbattery comprises the stacking of two microfabricated electrodes and placing a polymeric fluidic layer between them, i.e., sandwich-like design. The microbattery provides a capacity of around 200 $mA\,h\,g^{-1}$ ($\approx 160\,\mu Ah\,cm^{-2}$ with respect to the surface area of the limiting film electrode with a thickness of 1.1 μm). However, likewise to the single electrodes, a maximum SOC of 25% has to be maintained to enable a certain durability. It is found that the modular design of the microbattery is useful, in that, a degraded electrode can be replaced with a newly fabricated one. Of course, if the microbattery is integrated (embedded) in a microdevice, it seems difficult to perform such a replacement. Also, it is found that the microbattery provides a power density of around $5\,\mu W\,cm^{-2}$ at a current density of around $5\,\mu A\,cm^{-2}$ while maintaining a cell voltage of larger than $1V$. In terms of applications, our battery can power many MEMS sensors which have ultra-low power consumptions of around $0.5\,\mu W$ as reported by e.g. refs. [4, 5]. It could also be used for existing and emerging biomedical applications including pacemaker and a cardioverter-defibrillator ($< 10\,\mu W$) and body-area monitoring microsystems ($140\,\mu W$).

The presented microbattery is able to provide an area-specific and a volumetric power density of $\approx 0.05\,W\,m^{-2}$ and $\approx 0.045\,W\,cm^{-3}$, respectively. Lam et al. have mentioned a MEMS-based photosynthetic cell with an ultra-low-power density of around $10^{-10}\,W\,cm^{-3}$ [6]. Lemmerhirt and Wise have reported a microfabricated lithium cell with an estimated power density range of 0.075 to $1.5\,W\,m^{-2}$ (for a nominal voltage of $3.75\,V$) (ref.[7] as cited in ref.[8]). Further, higher volumetric power densities are reported by Humble et al. (Ni-Zn cell) and by Pikul et al. (lithium cell) at $3\,W\,cm^{-3}$ and $74\,W\,cm^{-3}$, respectively [2, 9]. Our microbattery power density is within the lower range of the reported densities in the literature, however, such larger power densities would not be necessary especially for MEMS applications. As mentioned in the introduction section of this thesis, ultra-low-power sensors would not require high powers, for instance.

In terms of other microbattery capacities, Albano et al. have reported capacities of up to $138\,\mu Ah\,cm^{-2}$ for an integrated zinc-silver oxide primary microbattery for implantable MEMS devices [8] while Humble et al. have stated a capacity range of 278 to $972\,\mu Ah\,cm^{-2}$ for a nickel-zinc microbattery [2]. In terms of capacity requirements, if we assume an operation time of around $4\,hr\,day^{-1}$ for the wireless sensor node reported for health monitoring system by Okada et al.[4, 5], a capacity of $\approx 1.7\,\mu Ah$ per day ($\approx 50\,\mu Ah$ per month) at a nominal voltage of $1.2\,V$ is required. This capacity is sufficient for the sensor to perform the measurement every minute for a duration of 10 seconds. The microbattery presented in this work with a capacity of $\approx 520\,\mu Ah$ (for a film electrode surface area of $2.54 \times 1.27\,cm$) is able to provide sufficient power for this sensor to operate for around 10 months, if the microbattery is charged at 100% SOC. Since we need to maintain around 25% SOC of the microbattery to prevent mechanical instability within the films, the microbattery can provide adequate power for the sensor to operate around 2.5 months at a single charge.

In the next section of this chapter, an outlook and recommendations for further research are given.

6.2 Outlook and Further Works

This thesis is focused on the development and characterization of a NiMH microbattery consisting of film electrodes on glass substrates. This study opens a new horizon for further research and yet there are aspects of the microbattery which can be improved. As for further optimization of the microbattery, there are also areas which have not been investigated in the current work; hence, the recommendations for further research are:

1) The durability of the film electrodes for a larger number of charge-discharge cycles still remains a challenge. The durability of the metal hydride films is significantly better than that of nickel hydroxide films as reflected in a larger number of reliable charge-discharge cycles. Achieving higher state of charge (SOC) values ($\geq 25\%$) along

with the durability of the film electrodes needs to be investigated. We employed a surface patterning method which improved the durability of the $Ni(OH)_2$ films. In future work, a thorough investigation of the surface patterning parameters should be undertaken. In detail, the effect of size, shape, aspect ratio and distance of the features on the film durability should be explored. In the current study, a chromium layer is used as an adhesion layer, further investigation with respect to using other materials, such as Titanium, should be performed. The current collector can also be optimized in terms of thickness and electroplating parameters. One possibility would be to pattern the surface of the glass substrates using an etching technique, that is, increasing the surface area of adhesion at the interface of the adhesion film layer and the glass surface. Further, the effect of annealing process on mechanical and materials integrity of the films should be studied.

2) Since the capacity of the microbattery is determined by the capacity of the negative metal hydride electrode (anode limited cell), further investigation is required to grow thicker films of intermetallic alloys which results in larger capacities. Also, another study should be towards obtaining higher power densities. Additionally, the use of higher electrolyte concentrations should be investigated to reduce the ohmic overpotentials and to improve the overall performance of the microbattery.

3) Given that an unwanted parasitic oxygen evolution reaction (OER) occurs at the nickel electrode during the operation of the microbattery, a further investigation to suppress such parasitic reactions would be beneficial. In paper #4 in chapter V, we have mentioned that the addition of cobalt to the nickel nitrate electrodeposition bath leads to films which show better durability as the oxidation peaks are shifted farther away from the OER region as also reported in ref.[10].

4) This microbattery features two-dimensional film electrodes. Given the higher surface area of three-dimensional (3D) microstructures for the same footprint area, further study is required to explore the possibility of microfabricating both electrodes in 3D, e.g., 3D micropillars of nickel hydroxide and metal hydride materials. This is also of great interest as the absolute power (power density multiplies by surface area) provided by the microbattery will be increased as well.

5) Since the resulting microbattery has a potential of being integrated and coupled with microscale devices such as sensors, this possibility should be further investigated through microfabrication of the cell during the device fabrication process. Also, the microbattery is a rechargeable cell, the coupling of the cell with energy harvesting devices (such as a solar cell) would be of great interest. Such hybrid power supplies are also mentioned in refs.[11, 2]. This also leads to an autonomous power supply system. Such an autonomous power supply can be used, for instance, as an indicator for medial diagnostics kits –in that light emitted diodes (LED) are triggered by a voltage as an indicator of the test results– may increase the availability of such point-of-care (POC) medical devices around the globe.

6.3 References

[1] J. Chen, D. H. Bradhurst, S. X. Dou, and H. K. Liu. Nickel hydroxide as an active material for the positive electrode in rechargeable alkaline batteries. *J. Electrochem. Soc.*, 146(10):3606–3612, 1999.

[2] Paul H. Humble, John N. Harb, and Rodney LaFollette. Microscopic nickel-zinc batteries for use in autonomous microsystems. *J. Electrochem. Soc.*, 148(12):A1357–A1361, 2001.

[3] Paul H. Humble and John N. Harb. Optimization of nickel–zinc microbatteries for hybrid powered microsensor systems. *J. Electrochem. Soc.*, 150(9):A1182–A1187, 2003.

[4] H. Okada, T. Itoh, and T. Masuda. Development of custom CMOS LSI for ultra-low power wireless sensor node in health monitoring systems. In *Sensors, 2011 IEEE*, pages 1197–1200, Oct 2011.

[5] H. Okada, H. Nogami, T. Kobayashi, T. Masuda, and T. Itoh. Development of ultra low power wireless sensor node with piezoelectric accelerometer for health monitoring. In *Solid-State Sensors, Actuators and Microsystems (TRANSDUCERS EUROSENSORS XXVII), 2013 Transducers Eurosensors XXVII: The 17th International Conference on*, pages 26–29, June 2013.

[6] Kien Bang Lam, Eric A Johnson, Mu Chiao, and Liwei Lin. A MEMS photosynthetic electrochemical cell powered by subcellular plant photosystems. *J. Microelectromech. Syst.*, 15(5):1243–1250, 2006.

[7] D.F. Lemmerhirt and K.D. Wise. Chip-scale integration of data-gathering microsystems. *Proc. IEEE*, 94(6):1138–1159, 2006.

[8] F. Albano, Y.S. Lin, D. Blaauw, D.M. Sylvester, K.D. Wise, and A.M. Sastry. A fully integrated microbattery for an implantable microelectromechanical system. *J. Power Sources*, 185(2):1524 – 1532, 2008.

[9] J. Pikul, H. Zhang, J. Cho, P. Braun, and W. King. High power lithium ion microbatteries with lithographically defined 3-d porous electrodes. In *IEEE 26th Intl Conf. on Micro Electro Mechanical Systems (MEMS)*, pages 857–860, 2013.

[10] Dennis A. Corrigan and Richard M. Bendert. Effect of coprecipitated metal ions on the electrochemistry of nickel hydroxide thin films: Cyclic voltammetry in 1M KOH. *J. Electrochem. Soc.*, 136(3):723–728, 1989.

[11] John N. Harb, Rodney M. LaFollette, Richard H. Selfridge, and Larry L. Howell. Microbatteries for self-sustained hybrid micropower supplies. *J. Power Sources*, 104(1):46 – 51, 2002.